Deutsches Zentrum
für Luft- und Raumfahrt
German Aerospace Center

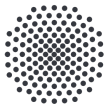

University of Stuttgart
Germany

MASTERS'S THESIS

Simulation of the contrast mechanisms of a heterodyne two-color interferometer

Simulation der Kontrastmechanismen eines heterodynen Zweifarb-Interferometers

Presented by
Aurelius Manny
Faculty 6: Aerospace Engineering and Geodesy
Student ID: 3224456

Reviewer
Prof. Dr. rer. nat. Thomas Dekorsy
Institute of Aerospace Thermodynamics (ITLR)
University of Stuttgart
and
Institute of Technical Physics
German Aerospace Center (DLR)

Supervisor
Hugo Uittenbosch
Institute of Technical Physics
German Aerospace Center (DLR)

December 23rd, 2024

Eidesstattliche Erklärung

Hiermit erkläre ich mich damit einverstanden, dass meine Masterarbeit zum Thema

Simulation of the contrast mechanisms of a heterodyne two-color interferometer

in der Institutsbibliothek des Instituts für Thermodynamik der Luft- und Raumfahrt öffentlich zugänglich aufbewahrt und die Arbeit auf der Institutswebseite sowie im Online-Katalog der Universitätsbibliothek erfasst wird. Letzteres bedeutet eine dauerhafte, weltweite Sichtbarkeit der bibliographischen Daten der Arbeit (Titel, Autor, Erscheinungsjahr, etc.). Nach Abschluss der Arbeit werde ich zu diesem Zweck meinem Betreuer neben dem Prüfexemplar eine weitere gedruckte sowie eine digitale Fassung übergeben. Der Universität Stuttgart übertrage ich das Eigentum an diesen zusätzlichen Fassungen und räume dem Institut für Thermodynamik der Luft- und Raumfahrt an dieser Arbeit und an den im Rahmen dieser Arbeit von mir erzeugten Arbeitsergebnissen ein kostenloses, zeitlich und örtlich unbeschränktes, einfaches Nutzungsrecht für Zwecke der Forschung und der Lehre ein. Falls in Zusammenhang mit der Arbeit Nutzungsrechtsvereinbarungen des Instituts mit Dritten bestehen, gelten diese Vereinbarungen auch für die im Rahmen dieser Arbeit entstandenen Arbeitsergebnisse.

.....

Ort, Datum, Unterschrift

Hiermit versichere ich, dass ich diese Masterarbeit selbstständig mit Unterstützung des Betreuers angefertigt und keine anderen als die angegebenen Quellen und Hilfsmittel verwendet habe. Die Arbeit oder wesentliche Bestandteile davon sind weder an dieser noch an einer anderen Bildungseinrichtung bereits zur Erlangung eines Abschlusses eingereicht worden. Ich erkläre weiterhin, bei der Erstellung der Arbeit die einschlägigen Bestimmungen zum Urheberschutz fremder Beiträge entsprechend den Regeln guter wissenschaftlicher Praxis eingehalten zu haben. Soweit meine Arbeit fremde Beiträge (z.B. Bilder, Zeichnungen, Textpassagen, etc.) enthält, habe ich diese Beiträge als solche gekennzeichnet (Zitat, Quellangabe) und eventuell erforderlich gewordene Zustimmungen der Urheber zur Nutzung dieser Beiträge in meiner Arbeit eingeholt. Mir ist bekannt, dass ich im Falle einer schuldhaften Verletzung dieser Pflichten die daraus entstehenden Konsequenzen zu tragen habe.

.....

Ort, Datum, Unterschrift

Abstract

Simulation of the contrast mechanisms of a heterodyne two-color interferometer

At the German Aerospace Center (DLR) an optical sensor is being developed to measure the refractive index of air using a two-color interferometer in the visible and infrared spectrum. The measured change of dispersion is related to the pressure change in air and thus the interferometer can be potentially deployed as a variometer in aviation applications. The experimental interferometer consists of two emitted laser beams of harmonically related wavelengths and features a frequency modulation scheme. The resulting heterodyne detection process on a photodetector leads to a beat signal for each emitted wavelength in the real-world setup. Due to the modulation frequencies of 80 MHz and 160 MHz for the infrared and visible wavelength, respectively, an investigation of the resulting interference patterns and other optomechanical effects in the laboratory is not feasible with conventional image recording methods.

Thus, to investigate the spatial and time-resolved interference a digital twin of the real-world interferometer was implemented. The propagation paths of the laser beams within the digital twin were obtained by utilizing complex ray tracing. In order to achieve this, prior and over the course of this thesis, a complex ray tracing framework was developed. To implement the digital twin, the necessary optical components and interactions of the interferometer were modelled. This includes surrogates for beamsplitters, as well as an acousto-optic modulator model to simulate the frequency modulation. For the modelling of Bragg diffraction, a vector formalism was researched in literature and implemented. A simulation of the resulting optical signal was implemented by calculating the interference patterns and utilizing a spatial photodetector model.

The interferometric phase of each wavelength was determined by applying an in-phase and quadrature demodulation algorithm to the generated optical power signals, matching the demodulation practice in the real-world. Furthermore, the spatial and time-resolved simulation allows to investigate the impacts of dynamic vibrations on the individual phases and the measurement result. This is especially useful to evaluate the vibration robustness of the interferometer. To compare the susceptibility of the two-color interferometer to vibrations, a component sensitivity analysis was carried out.

Keywords: interferometer, pressure measurement, dispersion interferometer, phase detection, vibrations, digital twin, optical simulation

Kurzzusammenfassung

Simulation der Kontrastmechanismen eines heterodynen Zweifarb-Interferometers

Am Deutschen Zentrum für Luft- und Raumfahrt (DLR) wird ein optischer Sensor zur Messung des Brechungsindex der Luft entwickelt. Dafür wird ein Zweifarb-Interferometer verwendet, das im sichtbaren und infraroten Bereich arbeitet. Das Funktionsprinzip des Interferometers basiert darauf, dass eine gemessene Änderung der Dispersion abhängig von einer Änderung des Luftdurcks ist. Damit kann das Interferometer potentiell als Variometer in der Luftfahrt eingesetzt werden. Der experimentelle Aufbau des Interferomters besteht aus zwei emittierten Laserstrahlen, deren Wellenlängen ein Vielfaches voneinander sind. Weiterhin wird eine heterodyne Detektionsmethode verwendet. Daher wird von einem Photodetektor ein Schwebungssignal für jede emittierte Wellenlänge registiert. Da das Schwebungssignal eine Frequenz von 80 MHz für die sichtbare und 160 MHz für die infrarote Wellenlänge aufweist, ist die Untersuchung von Interferenzeffekten am Photodetektor sowie weiterer optisch-mechanischer Effekt mit herkömmlichen Bildaufnahmetechniken im Labor nicht möglich.

Aus diesem Grund wurde, um die räumliche und zeitlich aufgelöste Interferenz des realen Interferometers zu untersuchen, ein digitaler Zwilling des Interferometers implementiert. Die Propagation der emittierten Laserstrahlen wurde mit dem Complex Ray Tracing Verfahren simuliert. Dafür wurde vor und im Rahmen dieser Arbeit ein Complex Ray Tracing Framework entwickelt. Um den digitalen Zwilling zu implementieren, wurden nötige optische Komponenten sowie deren Interaktion mit den Laserstrahlen modelliert. Dies beinhaltete zum einen verschiedene Strahlteiler sowie die Modellierung eines akusto-optischen Modulators, der das Schwebungssignal verursacht. Um die Beugung der Laserstrahlen nach Bragg im Kristall des akusto-optischen Modulators zu bestimmen wurde ein, aus der Literatur entnommener, Vektorformalismus verwendet. Die Simulation des resuliterenden optischen Signals wurde implementiert indem das Interferenzmuster auf der aktiven Fläche eines Photodetektormodells berechnet wurde.

Die interferometrische Phase jeder Wellenlänge wurde bestimmt, indem ein In-Phase und Quadratur-Verfahren zur Demodulation des Signal angewendet wurde. Dieses Verfahren kommt ebenfalls im experimentellen Aufbau des Interferometers zum Einsatz. Die räumliche und zeitlich aufgelöste Simulation ermöglicht weiterhin den Einfluss dynamischer Vibrationen auf die einzelnen Phasen zu untersuchen. Dies ist vorallem nützlich, um die Fehlerrobustheit des Interferometers gegenüber Vibrationen im Messprozess zu bewerten. Schlussendlich wurde die Fehleranfälligkeit einzelner Komponenten aufgrund von Vibrationen in einer Sensitivitätsanalyse verglichen.

Schlagwörter: Interferometer, Luftdruckmessung, Dispersionsinterferometer, Phasendetektion, Vibrationen, Digitaler Zwilling, Optische Simulation

Contents

List of Figures

List of Tables

Symbols and Acronyms

Symbol

Latin Symbols

f	Hz	Frequency
T	K	Temperature
p	Pa	Pressure
rh	%	Relative Humidity
n	-	Refractive index
c_s	$\frac{\text{m}}{\text{s}}$	Speed of sound
m	-	Order of diffraction
t	s	Time
c	-	Contrast
z_R	m	Rayleigh length
P	W	Optical power
Δx	m	Translation displacement

Greek Symbols

λ	m	Wavelength
φ	rad	Phase
$\Delta\varphi$	rad	Phase difference
ω	Hz	Frequency (optical)
Ω	Hz	Radio frequency
Λ	m	Acoustic wavelength
α	rad	Diffraction angle
τ	-	Beam splitter transfer matrix
$\Delta\theta$	$^\circ$	Rotation angle

Acronyms

AOI angle of incidence. 19, 26, 31, 32, 52, 57, 60

AOM acousto-optic modulator. 1, 2, 5, 7–9, 15, 21–26, 30–34, 39, 41–43, 45, 49, 51, 52, 55–60

API application programming interface. 13, 17, 21

CAD computer-aided design. 21, 30, 31

DI dispersion interferometer. 3, 5

DLR German Aerospace Center. 1

DOF degree of freedom. 36, 37

DPSSL diode-pumped solid-state laser. 4, 5, 13, 14, 31, 47

FIR finite impulse response. 45

FPGA field programmable gate array. 5

HBS harmonic beam splitter. 1, 5, 15–19, 21, 27, 28, 30, 31, 33, 49, 50, 53, 54, 56, 57, 59

I/Q in-phase and quadrature. 2, 5, 7, 44, 48, 52, 53, 57, 59

M mirror. 5, 20, 21, 30–33, 39, 40, 42, 49, 51–54, 56, 57

MI Michelson interferometer. 5, 35, 41, 42, 49

MZI Mach-Zehnder interferometer. 5, 6, 9

NIR near-infrared. 3, 14, 16, 34

OPL optical path length. 1, 29, 36, 37, 39, 47, 50, 51, 57, 59

PBS plate beam splitter. 1, 5, 15, 27, 28, 30–33, 49, 51–53, 56, 57, 59

PD photodetector. 1, 2, 5, 21, 27–30, 33, 39, 41–43, 47, 50, 58, 59

RR retroreflector. 5, 26, 27, 30–33, 37, 41, 47–51, 53, 57–59

SCDI single crystal dispersion interferometer. 13, 15, 16, 18, 19, 21, 28, 59

SDF signed distance function. 17

SDI synthetic dispersion interferometer. 1, 4, 5, 13, 30, 35, 44, 45, 57

SHG second harmonic generation. 3, 4, 13

STL standard triangle language. 21, 22

TEM transverse electromagnetic. 10, 12, 13, 15

1 Introduction

Modern aircraft rely heavily on accurate information about primary flight parameters, e.g. air speed, angle of attack, flight altitude and more. Traditionally, all of these parameters are determined by sensors that have to interact with the air stream directly, i.e. to measure the pressure. Dynamic, total and static air pressure are of high relevance, since they are used to derive the parameters mentioned previously. In recent decades it was observed that icing conditions or contamination may lead to a blockage of pressure sensing devices even if anti-icing measurements like heated sensors are installed on the aircraft. This can lead to incorrect flight state measurements with tragic outcomes like the Birgenair Flight 301 or Air France Flight 447. Thus, alternative methods to obtain the flight state are researched at the German Aerospace Center (DLR) at the Institute of Technical Physics.

An alternative way to determine air pressure or changes thereof optically is the concept of measuring the refractive index of air. The refractive index depends directly on the density of air, meaning that one can measure changes of the air temperature, air pressure or relative humidity by measuring changes of the optical path length (OPL). If, for instance, air temperature and humidity are known, the change in static air pressure can be obtained. This relation is described with high accuracy by the Ciddor equation [1].

One way to measure changes of the OPL is via interferometry. Two-color interferometry and dispersion interferometry are established techniques to perform this measurement in a way that is claimed to be robust against mechanical vibrations, which contribute to OPL fluctuations as well [2–4]. The synthetic dispersion interferometer (SDI) by Uittenbosch et. al (2022) is an optical sensor being developed at the DLR to measure the refractive index of air by emitting two wavelengths, one in the visible and the other in the infrared spectrum [5]. This device can be potentially used as an optical variometer in aviation, if the device is able to reduce the influence of mechanical vibrations encountered on an aircraft to an acceptable level.

The SDI is a heterodyne two-color interferometer, meaning that the signal at the photodetector (PD) is modulated periodically in the time-domain due to a difference in frequency between the reference and probe beams. This frequency modulation is generated via an acousto-optic modulator (AOM). The beat signals at the PD are generated for the visible wavelength at 160 MHz and 80 MHz for the infrared. Due to the beat signal frequency in the range of MHz the observation of interference at the PD with conventional imaging techniques is not feasible. Thus, the objective of this work is to investigate how vibrations affect the laser beams propagation path and the resulting phase readout in a simulation.

For this reason, a digital twin of the existing laboratory setup is implemented and the propagation paths of each emitted laser beam are computed with the complex ray tracing method. In Ch. 2 the underlying theory of heterodyne detection is presented as well as the utilized complex ray tracing method. For the digital twin optical components such as harmonic beam splitter (HBS) and plate beam splitter (PBS) need to be modelled. An AOM model is also required for simulation. To account for Bragg diffraction inside the AOM a vector formalism is implemented to model the AOM behaviour. The digital representation of optical components as well as the simulated laser beams are described in Ch. 3.1 and Ch. 3.2. The position and orientation of the modelled optical components are chosen to recreate the real-world interferometer setup and is described in Ch. 3.3. To

model vibrations harmonic mechanical oscillations are assumed and a military standard is considered in Ch. 3.4 to derive vibration frequencies. Furthermore, the diffraction inside the AOM leads to a frequency shift, which is the cause of the beat signal at the PD. To consider this time-dependence of the signal an appropriate simulation method is implemented, elaborated in Ch. 3.5.3. This time-domain simulation method allows to investigate the impact of vibrations on the measured phase and allows to analyse the contrast of the resulting power signal on the PD due to misalignments and vibrations. Individual vibration simulations of components are conducted with this simulation method. The obtained power signals are post-processed by an in-phase and quadrature (I/Q) demodulation algorithm to extract the individual phases equivalent to the data handling in the laboratory setup of the interferometer. The results of the conducted vibration simulations are presented in Ch. 4. The vibration robustness of the interferometer is evaluated with the obtained results for the assumed displacements and rotations. For this a sensitivity analysis comparing the optical components of their error susceptibility due to vibrations is carried out. Lastly, in Ch. 5 the results as well as their limitations are discussed.

2 Literature Review

In the following chapter basic principles involved in the numerically investigated interferometer are briefly elaborated. Furthermore, required optical components to set up the interferometer and their theoretical description are described. Lastly, the simulation method which was used in this work is outlined.

2.1 Dispersion Interferometry

Dispersion interferometry originates historically from plasma applications, mainly common in fusion reactors to measure the integrated electron density along a path. The classic, most simple, dispersion interferometer (DI) was proposed by Drachev et al. (1993) in the article "Dispersion interferometer for controlled fusion devices" [3]. The basic setup of this DI is illustrated in Fig. 2.1.

While the setup is applicable to any wavelength where frequency doublers exist, Drachev et al. used a radiation laser source of $\lambda_1 = 1.06\,\mu m$ [3]. For reasons of simplicity the working principle of the classic DI is explained with an emitting wavelength $\lambda_1 = 1064\,nm$, which is roughly the same as in Drachevs et al. work and lies within the near-infrared (NIR) range.

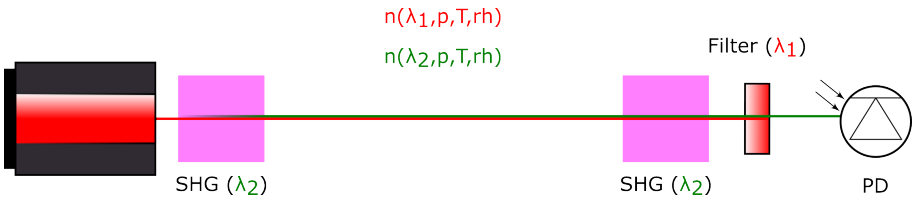

Figure 2.1: Classic DI setup by Drachev et al. featuring a single wavelength λ_1 emitting laser and two optical frequency doublers creating a second harmonic λ_2. The probe is placed between the frequency doublers [6].

First the laser emitted frequency is doubled by second harmonic generation (SHG) such that two beams of wavelength $\lambda_1 = 1064\,nm$ and $\lambda_2 = \frac{\lambda_1}{2} = 532\,nm$ are produced. Therefore the term two-color interferometer stems from the fact that two wavelengths are used. The wavelength of λ_1 corresponds to a frequency ω, whereas the beam doubled by SHG is of 2ω. The beam phases can be denoted as φ_ω and $\varphi_{2\omega}$.

Both beams propagate through a probe chamber filled with a dispersive medium, meaning the refractive index n varies with wavelength λ. Furthermore, the present conditions pressure p, temperature T and relative humidity rh in case of an atmosphere affect the refractive index. Ciddor explored the relationship between the refractive index and these quantities for air in detail, which led to the Ciddor equations [1].

After passing the probe medium a second SHG of λ_1 is carried out and λ_1 is filtered. This results in two beams of the same wavelength λ_2, where one is spawned by the first SHG and the other by the second SHG step. Both beams are superimposed on a photodetector.

We can quantify the phase of each beam, where l is the path length in the probe medium

respectively. For the emitted radiation source this is

$$\varphi_\omega = \frac{2\pi}{\lambda_1} \int_0^l n(\lambda_1, p, T, rh)\, dh\,, \tag{2.1}$$

while the beam of λ_2 after the first SHG is of

$$\varphi_{2\omega} = \frac{2\pi}{\lambda_2} \int_0^l n(\lambda_2, p, T, rh)\, dh\,. \tag{2.2}$$

For the second beam by SHG because of frequency and thus phase doubling

$$2\varphi_\omega = \frac{4\pi}{\lambda_1} \int_0^l n(\lambda_1, p, T, rh)\, dh\,. \tag{2.3}$$

The phase difference of the superimposed beams with same wavelength λ_2 on the photodetector is therefore $\Delta\varphi = \varphi_{2\omega} - 2\varphi_\omega$. With (2.2) and (2.3) and the relation $\lambda_1 = 2 \cdot \lambda_2$ it follows that

$$\Delta\varphi = \frac{2\pi}{\lambda_2} \int_0^l n(\lambda_2, p, T, rh) - n(\lambda_1, p, T, rh)\, dh\,. \tag{2.4}$$

For a homogeneous medium this integral can be reduced to

$$\Delta\varphi = \frac{2\pi \cdot l}{\lambda_2} \Big(n(\lambda_2, p, T, rh) - n(\lambda_1, p, T, rh) \Big)\,. \tag{2.5}$$

We therefore obtain an equation which holds the dispersion of the refractive index on the right hand side and the phase difference on the left, therefore the term dispersion interferometer [3].

For a measured phase difference the right hand side can be solved numerically with the Ciddor equations for pressure p if other quantities are held constant. For plasma applications the working principle is analogous. Likewise, dispersion of the refractive index and therefore the phase difference relates to the line integrated electron density [3, 6].

2.1.1 Synthetic Dispersion Interferometry

The SDI by Uittenbosch et al. (2023) is a sensor that measures changes in the relative pressure of air by the refractive index [5]. It is investigated as an optical method to determine the static pressure in aviation, or as an optical variometer [5]. The principle setup of the SDI is shown in Fig. 2.2.

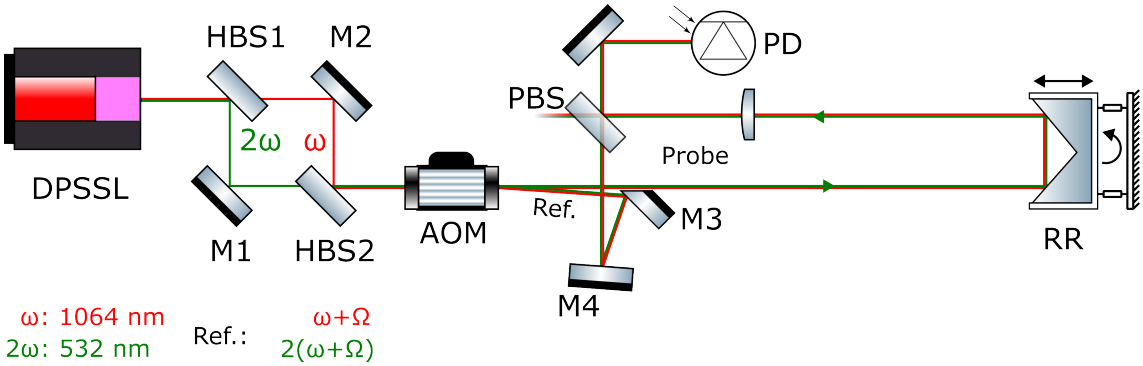

Figure 2.2: SDI setup by Uittenbosch et al. featuring a diode-pumped solid-state laser (DPSSL) emitting two frequencies ω and 2ω [6].

The setup is based on a DPSSL emitting two beams. This is achieved by intracavity frequency doubling in the laser resonator. One beam has the frequency ω, which corresponds to a wavelength of 1064 nm and the other beam 2ω which equals 532 nm. Because the beams are not emitted coaxially, a pair of HBS and mirrors (M) is used to adjust each beam independently, and, therefore guarantee the alignment of both beams [5].

Each beam is diffracted afterwards by an AOM. The deflected beams are the so-called reference beams. The deflection angle can be calculated with the Bragg equation, which is discussed later in Ch. 2.2.1. The 1st order deflection angle of ω equals the 2nd order deflection angle of 2ω. This is exploited so that both reference beams are coaxial after diffraction. Each deflected beam is also shifted in frequency depending on the diffraction order, so that the reference beams are of $\omega + \Omega$ and $2\omega + 2\Omega = 2(\omega + \Omega)$ [5].

The non-diffracted beams propagate through a probe medium and are thus called probe beams. They are reflected by a retroreflector (RR) and propagate a second time through the probe medium. Reference and probe beams are recombined by a PBS and directed onto a PD [5].

For each beam the phase can be again denoted as φ_ω and $\varphi_{2\omega}$. In case of the SDI one has to consider that the phase of each beam is the difference between reference and probe beam

$$\varphi_\omega(t) = (\omega + \Omega) \cdot t - \left(\omega t - \frac{2\pi}{\lambda_\omega} \int_0^l n(\lambda_\omega) dh \right) + \Phi_{\mathrm{NCP}} \tag{2.6}$$

and

$$\varphi_{2\omega}(t) = 2(\omega + \Omega) \cdot t - \left(2\omega t - \frac{2\pi}{\lambda_{2\omega}} \int_0^l n(\lambda_\omega) dh \right) + \Phi_{\mathrm{NCP}} \tag{2.7}$$

where Φ_{NCP} are the non-common path phase contributions which are perturbations that do not cancel out. With the relation $\Delta\varphi = \varphi_{2\omega} - 2\varphi_\omega$ and $\lambda_\omega = 2 \cdot \lambda_{2\omega}$ it follows that

$$\Delta\varphi = \frac{2\pi}{\lambda_{2\omega}} \int_0^l n(\lambda_{2\omega}, p, T, rh) - n(\lambda_\omega, p, T, rh)\, dh \tag{2.8}$$

thus allowing to quantify the relative pressure [5].

However, compared to the classic DI, the requirement of a second frequency doubler is eliminated by post-processing and performing an I/Q demodulation on a field programmable gate array (FPGA). Therefore, the term synthetic dispersion interferometer has been proposed. Another characteristic of the two-arm, two-color design is the robustness to vibrations. If the optical path of both generated beams are equally altered by external forces, no effect of the phase difference will be measured in theory. In this work it is investigated how much this statement holds true for arbitrary vibrations of components. For a detailed description of the SDI and its working principle the article by Uittenbosch et. al (2023) is recommended [5].

2.1.2 Homodyne Detection

Homodyne Detection, from Ancient Greek "homos" meaning equal, is a technique which shares the same frequency of probe and reference beam. For an interferometer this detection technique can be implemented with a simple beam splitter which splits a coherent source beam into a probe and reference beam. Combining these beams again and superimposing them leads to a static interference pattern, if we assume that the source beam does not fluctuate in power and neglect the frequency of light itself. Classic interferometers featuring a homodyne detection method are the Michelson interferometer (MI) or the Mach-Zehnder interferometer (MZI), which is depicted in Fig. 2.3.

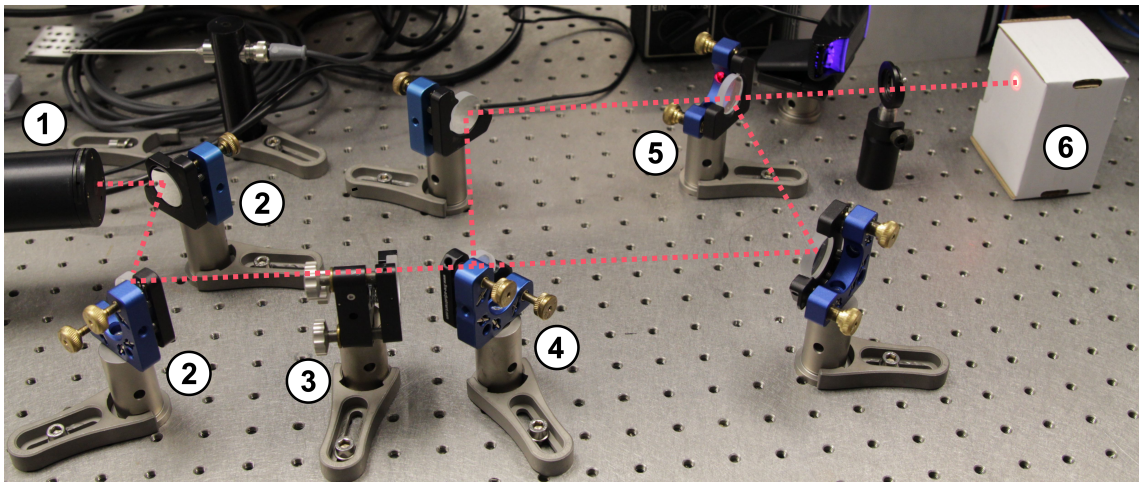

Figure 2.3: MZI setup with laser source on the left ①. The beam (red dashed line) is redirected by two mirrors ② followed by a diverging lens ③ such that the beam spot radius is increased for better visualization. A beam splitter ④ leads to a reference beam (upper path) and a probe beam (lower path). They are unified by a second beam splitter ⑤ and projected onto a card box ⑥.

Because a direct measurement of the relative phase difference between reference and probe beam is not possible another physical quantity is necessary to obtain the relative phase difference. If we assume that the laser source signal $E(t)$ can be described by a light wave with an amplitude E_0 and a frequency ω

$$E(t) = E_0 \cdot \sin(\omega t) \tag{2.9}$$

then the reference beam $E_R(t)$ and probe beam $E_P(t)$ can be written as

$$E_R(t) = E_1 \cdot \sin(\omega t) \tag{2.10}$$

$$E_P(t) = E_2 \cdot \sin(\omega t + \varphi) \tag{2.11}$$

where φ is the relative phase difference between probe and reference beam. E_1 and E_2 are determined by the power splitting ratio. For example a 50:50 beam splitter would halve the amplitude E_0 for both reference and probe beam. The measurable intensity $S(t)$ of reference and probe beam at a photodetector can then be expressed as

$$S(t) \propto |E_R(t) + E_P(t)|^2 \,. \tag{2.12}$$

With the use of trigonometric identities and assuming that the bandwidth B of the photodetector is $B \ll \omega$, meaning that any ωt can be neglected, it follows that

$$S(t) \propto \frac{1}{2}E_1^2 + \frac{1}{2}E_2^2 + E_1 E_2 \cdot \cos(\varphi) \,. \tag{2.13}$$

For a constant input amplitude $E_0 = 2$ and 50:50 beam splitter, thus $E_1 = E_2 = 1$ this can be simplified to

$$S(t) \propto 1 + c \cdot \cos(\varphi) \tag{2.14}$$

with interferometric contrast $c = 1$. The intensity signal $S(t)$ measured by the photodetector is only a function of the relative phase difference $\varphi(t)$ between reference and probe beam. Therefore, if $\varphi = 0$ the intensity will be at the maximum because of constructive interference.

For $\varphi = \pi$, a minimum in intensity can be measured because of destructive interference. The determination of φ via an inverse function $\arccos(S(t))$ leads to a ambiguity if φ exceeds the interval of $[0, \pi]$. In practical applications this can be solved by unwrapping the phase function. However, this may not work in all cases as the wrap detection in an arcsin or arccos unwrapping algorithm is prone to errors mainly due to noise. Filtering and advanced unwrapping algorithms are then necessary to achieve acceptable results.

2.1.3 Heterodyne Detection and I/Q Demodulation

Heterodyne Detection, from Ancient Greek "hetero" meaning different, uses distinct frequencies in reference and probe beam. The setup is similar to a homodyne interferometer. Two beams are generated by splitting up a source beam. However, the probe or reference beam is then shifted in frequency e.g. by a Bragg cell or an AOM, see Ch. 2.2.1 for a detailed description of AOM. The shift frequency is typically orders of magnitudes smaller than the light frequency.

This leads to the following equations for reference and probe beam, where the probe beam is shifted by frequency Ω and φ is the relative phase difference between reference and probe beam

$$E_R(t) = E_1 \cdot \sin(\omega t) \tag{2.15}$$

and

$$E_P(t) = E_2 \cdot \sin((\omega + \Omega) \cdot t + \varphi)\,. \tag{2.16}$$

With Eq. (2.12) and the same assumption as in the homodyne detection, that the photodetector bandwidth is $B \ll \omega$, it follows that the intensity signal is

$$S(t) \propto \frac{1}{2}E_1^2 + \frac{1}{2}E_2^2 + E_1 E_2 \cdot \cos(\Omega \cdot t + \varphi) \tag{2.17}$$

and with $E_1 = E_2 = 1$ we obtain

$$S(t) \propto 1 + c \cdot \cos(\Omega \cdot t + \varphi) \tag{2.18}$$

with contrast $c = 1$. For heterodyne detection the intensity signal is time-dependent and not only a function of the relative phase difference φ, but also of the frequency shift Ω, so that the relative phase can not be extracted from the measured power on the photodetector directly. To obtain the relative phase a different approach has to be used. This is achieved by mixing the intensity signal with the frequency Ω and extracting the in-phase component I and quadrature component Q. This technique is called I/Q demodulation [5].

The real intensity signal S is mixed such as

$$S_{IQ}(t) = S(t) \cdot e^{-i\Omega t} \tag{2.19}$$

$$S_{IQ}(t) = (1 + c \cdot \cos(\Omega \cdot t + \varphi)) \cdot e^{-i\Omega t} \tag{2.20}$$

$$S_{IQ}(t) = e^{-i\Omega t} + c \cdot \cos(\Omega \cdot t + \varphi) \cdot e^{-i\Omega t} \tag{2.21}$$

$$S_{IQ}(t) = e^{-i\Omega t} + c \cdot \frac{1}{2} \cdot (e^{i(\Omega t + \varphi)} + e^{-i(\Omega t + \varphi)}) \cdot e^{-i\Omega t} \tag{2.22}$$

$$S_{IQ}(t) = e^{-i\Omega t} + c \cdot \frac{1}{2} \cdot (e^{i\varphi} + e^{-i(2\Omega t + \varphi)}) \tag{2.23}$$

An ideal low-pass filter is applied to the mixed signal to filter out frequencies $\geq \Omega t$. This leads to

$$S_{IQ_{\text{filtered}}}(t) = c \cdot \frac{1}{2} \cdot e^{i\varphi} \tag{2.24}$$

$$S_{IQ_{\text{filtered}}}(t) = c \cdot \frac{1}{2} \cdot (\cos(\varphi) + i \sin(\varphi)) \tag{2.25}$$

The in-phase component I can be expressed as

$$I(t) = \text{Re}(S_{IQ_{\text{filtered}}}(t)) = c \cdot \frac{1}{2} \cdot \cos(\varphi) \tag{2.26}$$

and the out-of-phase or quadrature component Q with

$$Q(t) = \text{Im}(S_{IQ_{\text{filtered}}}(t)) = c \cdot \frac{1}{2} \cdot \sin(\varphi)\,. \tag{2.27}$$

With the relation

$$\frac{Q}{I} = \frac{c \cdot \frac{1}{2} \cdot \sin(\varphi)}{c \cdot \frac{1}{2} \cdot \cos(\varphi)} = \tan(\varphi) \tag{2.28}$$

and therefore

$$\varphi = \arctan\left(\frac{Q}{I}\right) \tag{2.29}$$

the phase φ can finally be extracted [5]. Note that the phase φ is not limited to a constant value but can be a function of time $\varphi(t)$ as well.

2.2 Optical Components

For the simulation of the interferometer optical components are necessary. In the following chapters two relevant optical components are introduced and their features are elaborated.

2.2.1 Acousto-optic Modulator

An AOM is often characterized by a quartz crystal which is driven by a radio frequency Ω. In Fig. 2.4 such an AOM is depicted. This leads to sounds waves moving through the quartz crystal in a column. The sound waves propagate with the crystal speed of sound c_s, which is a material property, and act as an optical diffraction grating.

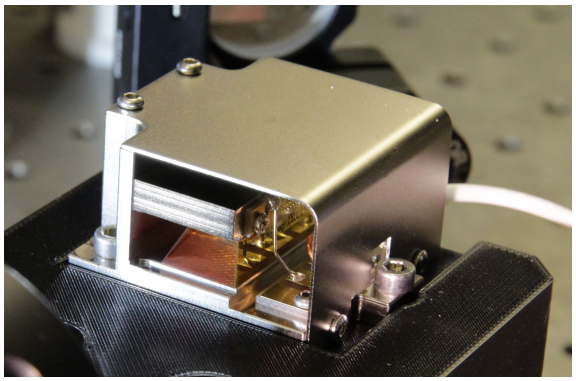

Figure 2.4: The quartz crystal has an incident front surface on which the light beam is directed. The white cable in the background connects the AOM with a driver, which generates the radio frequency Ω.

The acoustic wavelength Λ can be interpreted as the slit distance in a common diffraction grating and is defined as

$$\Lambda = \frac{c_s}{\Omega}\,. \tag{2.30}$$

Typical values for the radio frequency Ω are in the range of MHz resulting in acoustic wavelengths of µm. The deflection angle α of the diffracted beam relative to the non-diffracted beam can be calculated with the Bragg equation

$$\alpha = \frac{m \cdot \lambda}{\Lambda} = \frac{m \cdot \lambda \cdot \Omega}{c_s}\,, \tag{2.31}$$

where m is the order of diffraction and λ is the incident beams wavelength. In case of calculating the deflection angle within the medium, λ has to be divided by the refractive index of the medium [7].

Diffraction in an AOM not only leads to a deflection of an incident beam but also to a frequency shift Δf which equals

$$\Delta f = m \cdot \Omega\,. \tag{2.32}$$

One can see that the frequency shift is solely a function of the externally tuned radio frequency and can therefore be easily modified. With constant λ and c_s the diffraction angle α can be also adjusted by Ω, which is typically in the range of a few mrad [7].

Korpel generalized the calculation of diffraction for an AOM by applying vector algebra. The incident light ray can be denoted as $\vec{s}_o$ and the sound vector of the sound waves as $\vec{s}_s$. Then the following equation gives the direction of the diffracted light $\vec{s}_\pi$, if $\vec{s}_o$ and $\vec{s}_s$ are unit vectors

$$K\vec{s}_s + k\vec{s}_o = k\vec{s}_\pi\,, \tag{2.33}$$

where $K = \frac{1}{\Lambda}$ and $k = \frac{1}{\frac{\lambda}{n}} = \frac{n}{\lambda}$. Dividing the equation by k leads to

$$\vec{s}_\pi = \frac{K}{k}\vec{s}_s + \vec{s}_o\,. \tag{2.34}$$

This vector formalism generalizes the diffraction of an AOM and is especially useful for three-dimensional problems [8].

2.2.2 Beam Splitter

Beam splitters can be used to split the power of an incoming beam, e.g. a 50:50 beam splitter would halve the beam power for each generated beam. In other cases the polarization is split up, such that the output is either vertically or horizontally polarized [9, 10]. A beam splitter can be described by two inputs E_1 and E_2 and two outputs E_3 and E_4. Each input and output represents an electric field. In Fig. 2.5 a generic plate beam splitter with inputs and outputs is shown. Inputs and outputs can be related by a beam splitter matrix τ

$$\begin{bmatrix} E_3 \\ E_4 \end{bmatrix} = \tau \begin{bmatrix} E_1 \\ E_2 \end{bmatrix} = \begin{bmatrix} t_{31} & r_{32} \\ r_{41} & t_{42} \end{bmatrix} \begin{bmatrix} E_1 \\ E_2 \end{bmatrix}\,, \tag{2.35}$$

with the transmission coefficients t_{31} and t_{42} and the reflection coefficients r_{32} and r_{41}. The conservation of energy leads to the constraint that the beam splitter matrix τ must be unitary [11, p. 89–90]. Another constraint, related to the energy conservation of the beams, is the difference in phase shifts. In case of the MZI two beams are partially reflected and transmitted. The resulting summed power can not exceed the summed input power. If a beam gets directly reflected $E_1 \rightarrow E_4$ a phase shift of π takes place. To fulfil the condition of energy conservation now, the phase shift of the reflected beam from $E_2 \rightarrow E_3$ is constrained and must be 0. This can be also observed at the MZI. If constructive interference is visible for E_3, then destructive interference will occur for E_4 and vice versa.

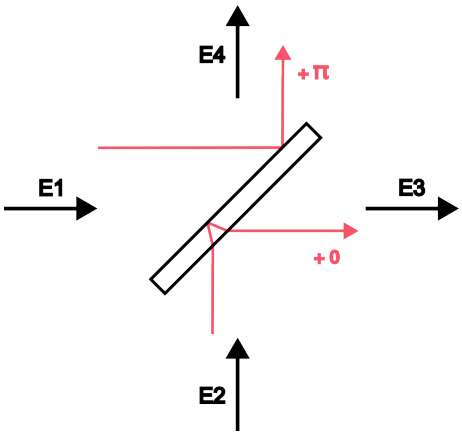

Figure 2.5: Inputs E_1 and E_2 and Outputs E_3 and E_4. The phase shift depends on the beam path [11, p. 89].

2.3 Gaussian Beamlet Tracing

The properties of light can either be described by particles or waves depending on the observed phenomena, this is well known as the wave-particle duality of light. To analyse the behaviour of light waves, the wave equation can be used as a starting point. In case of light the wave equation is a partial differential equation for the electric field E in space and time [11, p. 5, 12, p. 31].

Analytic solutions for the wave equation are for example spherical waves or plane waves. However, these solutions are not sufficient to describe a laser beam in detail. By separating time and space the wave equation can be transformed into two independent equations for the electric field E, one for time and space respectively. The time-independent equation is called the Helmholtz equation and is useful to further investigate the electric field in space [12, p. 32].

If the electric field of the light beam is closely formed around the propagating axis of the light beam, meaning small angles between light rays and the optical axis can be assumed, which is the case for laser beams, the paraxial approximation is valid. This leads to the paraxial Helmholtz equation, in which multiple terms of the ordinary Helmholtz equation are neglected [12, p. 35].

2.3.1 Gaussian Beam

The Gaussian beam is a solution of the paraxial Helmholtz equation [12, p. 35]. Laser beams are therefore often described by the electric field E of a Gaussian beam. Multiple characteristics of the Gaussian beam can be experimentally verified. While there are several other solutions to the paraxial Helmholtz equation, a fundamental solution is the Gaussian beam with a transverse electromagnetic (TEM) TEM_{00} mode. Higher-order TEM modes exist too, but are not of interest in this work. For a radius r and a propagation distance z in cylinder coordinates the electric field for the fundamental Gaussian beam with a TEM_{00} mode can be expressed as

$$E(r,z) = E_0 \frac{w_0}{w(z)} e^{-r^2/w(z)^2} e^{ikz} e^{i\psi(z)} e^{ikr^2/2R(z)} \tag{2.36}$$

where E_0 is the electric field amplitude at $E(0,0)$ and w_0 is the beam waist radius [12, p. 58]. The beam radius w at the z-position can be calculated with

$$w(z) = w_0 \sqrt{1 + \left(\frac{z}{z_R}\right)^2} \tag{2.37}$$

where z_R denotes the Rayleigh length

$$z_R = \frac{\pi w_0^2 n}{\lambda} \tag{2.38}$$

with refractive index of the medium n and beam wavelength λ [12, p. 58–60].

The term $e^{-r^2/w(z)^2}$ describes the radial distribution of the electric field. For radius $r = 0$ the term will be maximum, for any other r the electric field drops with e^{-r^2} for constant z which equals a Gaussian distribution, hence the common term Gaussian beam.

The three exponential terms containing the imaginary unit i hold the phase information of the Gaussian beam [12, p. 60]. The term e^{ikz} is related to the phase of a plane wave, where k is the wave number

$$k = \frac{2\pi}{\lambda}\,. \tag{2.39}$$

The second phase term $e^{i\psi(z)}$ contains the so-called Gouy phase

$$\psi(z) = -\arctan\left(\frac{z}{z_R}\right) \tag{2.40}$$

and is necessary since the phase of a Gaussian beam does not equal the phase of a plane wave. For $z \to \pm\infty$ the Gouy phase is $\psi(z) \to \pm\pi/2$ [12, p. 61].

The last phase term $e^{ikr^2/2R(z)}$ takes into account that the phase front has a curvature depending on the propagation distance z. The function $R(z)$ gives the phase front curvature radius and is defined as

$$R(z) = z\left(1 + \left(\frac{z_R}{z}\right)^2\right)\,. \tag{2.41}$$

For $z \to 0$ at the beam waist the curvature $R \to \infty$ which equals a plane wave. For $z = z_R$ the curvature radius is at minimum and increases then again nearly linearly [12, p. 61].

Because of imaginary terms the electric field of a Gaussian beam maps every point in space (r, z) to a complex number $E(r, z)$. The intensity I is a function of the electric field and can be calculated with

$$I(r,z) = \frac{|E(r,z)|^2}{2Z} \tag{2.42}$$

where Z is the wave impedance, which is a medium property [12, p. 127]. By applying the absolute value function to the electric field, the resulting quantity is no longer imaginary but real. The total net optical power P that results for example on a photodetector can then be expressed by integrating the intensity I

$$P = \int_{r=0}^{\infty} I(r)\, 2\pi\, r\, dr\,. \tag{2.43}$$

at a fixed position z over radius r [12, p. 59].

2.3.2 Complex Ray Tracing

In many real-world applications it is of interest how a laser beam propagates through an optical system with components like lenses to analyse the propagation path and obtain Gauss parameters such as the beam spot radius w or the intensity distribution I. A common method is to use geometrical optics to trace light rays through an optical system. For simple light rays the mathematical concept of vectors can be used to trace a ray through space. The laws of reflection and refraction such as Snell's law can be applied to vectors. This method of calculating the propagation path of a ray is known as geometrical ray tracing.

In case of the Gaussian beam, however, there is not a single light ray but an electric field propagating. Arnaud (1985) showed that a Gaussian beam with fundamental TEM_{00} mode can be represented by a complex ray $X(z)$, thus the name complex ray tracing [13]. The complex ray $X(z)$ consists of two real paraxial rays

$$X(z) = \xi(z) + i\,\eta(z) \tag{2.44}$$

where z is the propagation distance. $\xi(z)$ can be interpreted as the waist ray which travels parallel to the optical axis. $\eta(z)$ is the divergence ray and propagates under the divergence half-angle θ

$$\theta = \frac{\lambda}{\pi w_0} \tag{2.45}$$

where w_0 is the beam waist radius and λ the wavelength [12, p. 60]. For the purpose of global orientation it is common to define a chief ray which is used to track the optical axis of the Gaussian beam. Each ray, that is waist, divergence and chief ray, is then independently traced like in geometrical ray tracing. In Fig. 2.6 the principle of complex ray tracing is shown. The Gauss parameters and thus the scalar electric field E of the Gaussian beam can

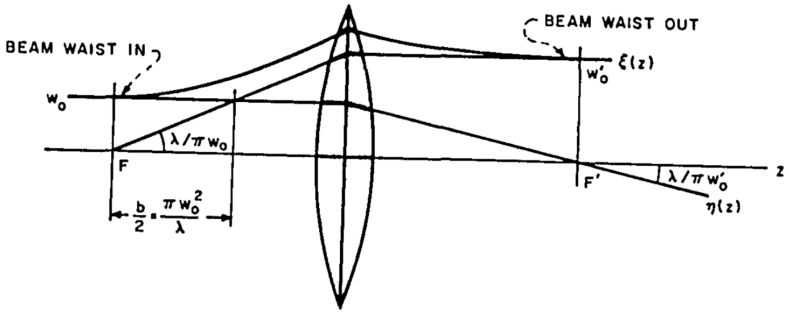

Figure 2.6: Complex ray tracing by tracing a waist ray and a divergence ray [13].

be calculated with the waist and divergence ray by geometric relations for any z provided by Arnaud [13]. To implement complex ray tracing in a simulation software DeJager et. al (1992) provided with the Y-NU procedure a set of equations to improve the calculation of the Gaussian beam parameters [14]. Gaussian beams which follow a skewed ray path will generally be subject to astigmatism [14, 15]. Kochkina (2013) provided a detailed description of the general astigmatic Gaussian beam [16]. In this work aberrations of the Gaussian beam are not considered. Stigmatic Gaussian beams are assumed and used for simulations.

3 Numerical setup of simulation

To investigate the heterodyne two-color interferometer numerically a digital twin of the interferometer was implemented. The digital twin is based on the SDI by Uittenbosch et al. (2023) which is discussed in Ch. 2.1.1. For this work a custom Julia-based ray tracing simulation was used that implements the complex ray tracing method. It has been developed in-house prior to and as part of this work. This software is denoted as the single crystal dispersion interferometer (SCDI) package in the context of this work. The package provides an application programming interface (API) to set up optical components and to solve the propagation path of beams within this optical system. The package is written in Julia, a script-based programming language designed for fast scientific applications while remaining rapid in development [17]. The following chapters provide an overview of the laser beams and optical components used in the digital twin of the interferometer. Furthermore, the implementation of vibrations and the different simulation methods, which were applied to obtain results, are elaborated upon.

3.1 Modelling of the Laser Beams

A DPSSL with intracavity SHG emits two laser beams, one with frequency ω corresponding to a wavelength $\lambda_\omega = 1064\,\text{nm}$ and another beam with frequency 2ω equalling $\lambda_{2\omega} = 532\,\text{nm}$. The laser beams are modelled by Gaussian beams each with a TEM_{00} mode. Astigmatism, spherical aberrations and polarisation effects are not considered. The SCDI package provides a default implementation for such Gaussian beams. In Fig. 3.1 a dummy of the DPSSL laser casing on top of a heatsink is rendered and the two emitted laser beams are visualized.

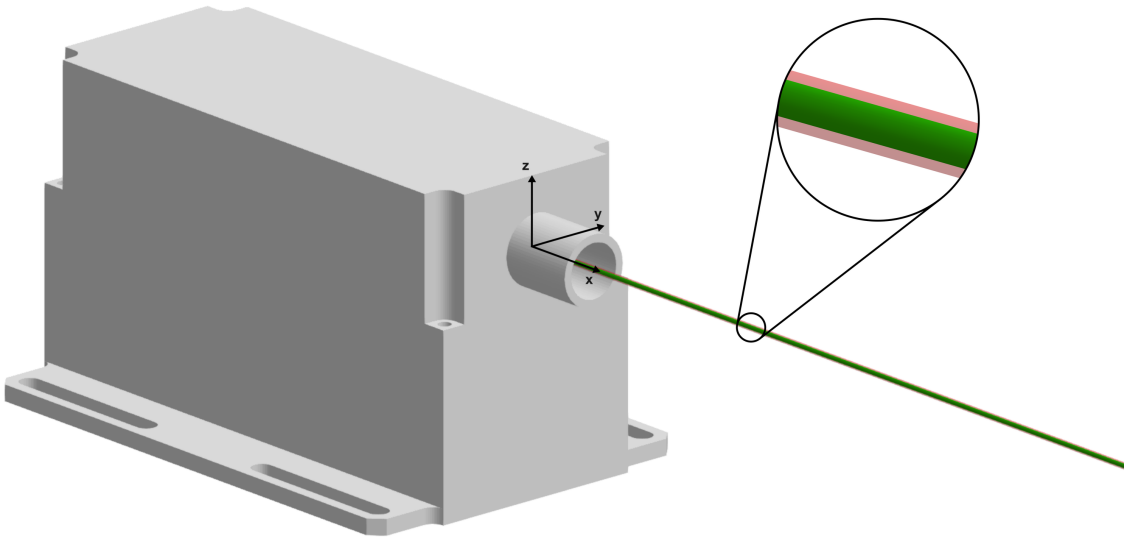

Figure 3.1: DPSSL emits two coaxially aligned laser beams of wavelength λ_ω, colored transparent-red and wavelength $\lambda_{2\omega}$, colored green.

The beams are spawned at global coordinates $x = 0\,\text{m}$, $y = 0\,\text{m}$ and $z = 0\,\text{m}$. This means that the beam waist of each Gaussian beam is initialized with default parameters at these coordinates along the x-axis. In Tab. 3.1 an overview of the initial beam parameters is given. The data was extracted from the article by Uittenbosch et al. (2023) and the DPSSL manual [5]. For simulations it was assumed that the emitted laser beams are not subject to aberrations and the beam quality factor for both beams is $M^2 = 1$. Outside of any optical component it is assumed that the laser beams propagate through air and thus a refractive index of $n = 1$ is used. Effects prior to the exit aperture of the DPSSL are not considered. Therefore the beams are also spawned surrounded by air.

Table 3.1: Initial laser beam parameters used in the digital twin

Parameters	Laser beam 1	Laser beam 2
Color	Visible	NIR
Wavelength λ [nm]	532	1064
Power P_0 [mW]	10.64	36.22
Beam waist radius w_0 [mm]	0.626	0.9705
Spawn direction [x y z]	[1 0 0]	[1 0 0]

In Fig. 3.2 the intensity distributions for each beam is shown shortly after the beam waist. The intensity integrated over the area equals the optical power with which the beams are spawned. One can see that the beam spot radii are different in size and approximately equal to the values given in Tab. 3.1.

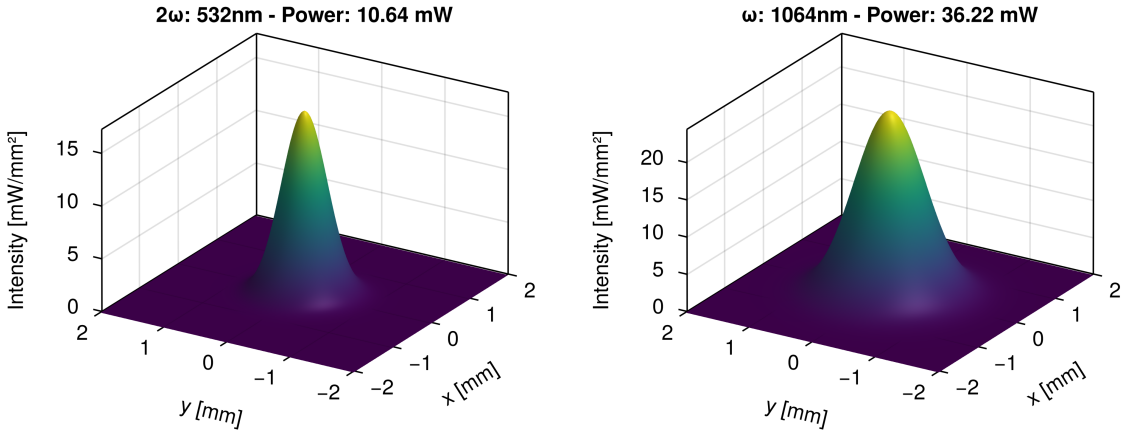

Figure 3.2: Three-dimensional intensity distribution of the emitted laser beams with frequency ω and 2ω. The distance from the beam waist for both beams is 5 cm. Integrating the intensity over the area gives the optical power.

For both emitted beams the Rayleigh length z_R, defined in Eq. (2.38), can be calculated with the parameters provided in Tab. 3.1. For the laser beam of frequency ω the Rayleigh length is

$$z_{R_\omega} = \frac{\pi \cdot (0.9705\,\text{mm})^2}{1064\,\text{nm}} = 2.78\,\text{m} \tag{3.1}$$

and for 2ω

$$z_{R_{2\omega}} = \frac{\pi \cdot (0.626\,\text{mm})^2}{532\,\text{nm}} = 2.31\,\text{m}. \tag{3.2}$$

The divergence half-angle θ can be determined with Eq. (2.45). For ω the divergence half

angle is

$$\theta_\omega = \frac{1064\,\text{nm}}{\pi \cdot 0.9705\,\text{mm}} = 0.35\,\text{mrad} = 0.02^\circ \tag{3.3}$$

and for 2ω

$$\theta_{2\omega} = \frac{532\,\text{nm}}{\pi \cdot 0.626\,\text{mm}} = 0.27\,\text{mrad} = 0.015^\circ \tag{3.4}$$

Because $\theta_\omega > \theta_{2\omega}$ the divergence of ω is greater. This marginal difference becomes apparent for large propagation distances later on.

The SCDI package makes use of the complex ray tracing procedure, see Ch. 2.3.2, to obtain the propagation path of TEM_{00} Gaussian beams. To reduce computational cost the SCDI package traces a Gaussian beam with one chief, one divergence, and one waist ray in three-dimensional space and checks if the intersection object for each ray is identical. For non-astigmatic Gaussian beams this is a valid method because TEM_{00} Gaussian beams are rotationally symmetric around the propagating axis. In many tracing applications this is also sufficient to obtain the correct propagation path. Geometrical critical situations, e.g. optical components positioned very close to each other or so-called clipped laser beams, which only partially intersect with a surface of an object, must be taken into consideration. In these cases the trace is then either stopped or non-physical phenomena are introduced into the simulation.

3.1.1 Simulation Constraints

As mentioned in previous sections, the simulation method for this work can not capture the effects of aberrations and polarizing effects on the propagation of the Gaussian beam throughout the optical system. While the method of complex ray tracing can achieve this in principle, i.e. in the work of Worku et al. (2017) [18], it was chosen to use this simplified method due to the following reasons.

Firstly, the optics used for this simulation are planar in almost all cases. Therefore, several forms of aberrations are assumed to be negligible, e.g. spherical aberrations. Secondly, chromatic aberrations are considered to have a primary effect on the waist position of the individual beams, since they are monochromatic and are therefore considered by the formalism. Astigmatism has also been considered as a source of potential distortion for the simulation results. However, since all wedge angles within the optical system are small, on the order of a few arcmin, astigmatism is also not considered further.

This leaves polarization effects as the main source of uncertainty with respect to the simulation. The complex ray tracing method presented in Ch. 2.3.2 cannot model these without modification. The ramifications of these circumstances on the results will be discussed in Ch. 5.

3.2 Modelling of Components

The SCDI package already provides components like mirrors and lenses for this. In Fig. 3.3 a showcase of tracing a Gaussian beam through multiple varying lenses with the SCDI package is shown. However, it was necessary to implement further components such as HBS, PBS, and AOM for the digital twin. In this chapter optical components of the digital twin, their representation, as well as their the underlying equations are described.

3.2.1 Harmonic Beam Splitter

The HBS is a specialized variant of the generic beam splitter. It either reflects or transmits light depending on the incident beams wavelength. A HBS might be designed to separate

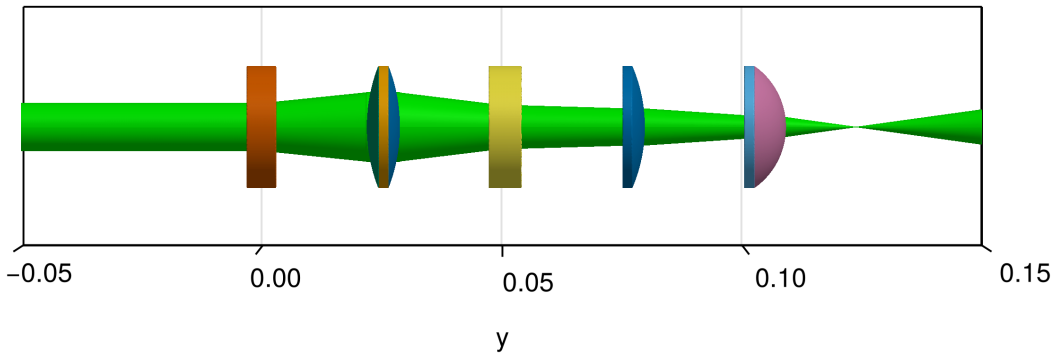

Figure 3.3: SCDI showcase of a beam propagating through a system of lenses.

light with $\lambda_1 = 1064\,\text{nm}$ from an overlapping beam with $\lambda_2 = 532\,\text{nm}$, which is the second harmonic of λ_1 [19]. The principle of operation is shown in Fig. 3.4. Depending on the coating the HBS either reflects the primary or the second harmonic. This allows to separate coaxially aligned beams of different, harmonically related, wavelengths.

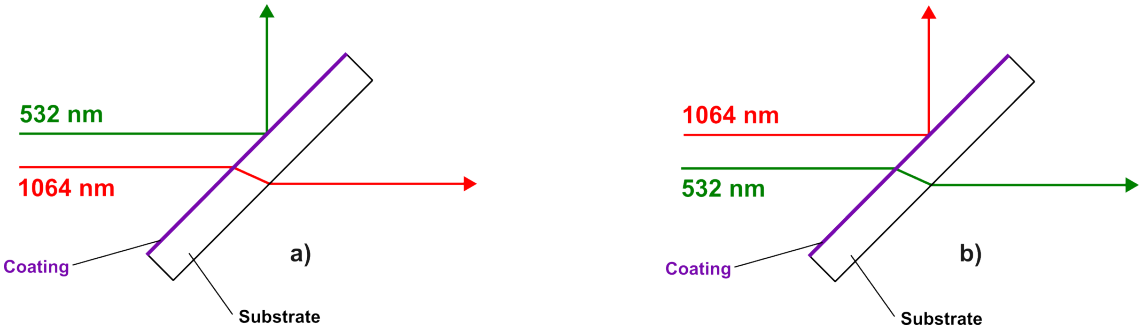

Figure 3.4: The HBS principle is visualized: In a) the HBS reflects green light and transmits NIR light. In b) the green light is transmitted while the NIR light is reflected. Whether case a) or b) is present depends on the coating of the HBS.

Figure 3.5: HBSY12 by company Thorlabs. The direction of light transmission is marked with an arrow on the side near the identifier. One can see that the colored coating stands out against the substrate [19].

Optical components are represented in the simulation and digital twin by a geometry and an arbitrary optical interaction. The geometry can be for example a mesh consisting

of triangles or a signed distance function (SDF). If a light ray intersects a geometry an interaction is triggered in the context of the API, for example refraction. The digital representation of the HBS shape consists of two joined mesh surfaces. One mesh surface is called coating and is necessary to determine which wavelengths will be reflected or transmitted. This surface is a plane mesh with zero thickness in two dimensions. In Fig. 3.6 the mesh of the coating is visualized. It consists of two triangles resulting in a rectangular mesh surface. The second surface is called substrate and accounts for the refraction of the transmitted beam. Refraction occurs because the substrate has a different refractive index than its surrounding medium. The substrate is a cuboid mesh consisting of triangles with one face missing resulting in an open surface. In Fig. 3.7 the substrate mesh is visualized.

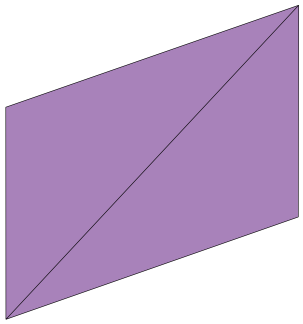

Figure 3.6: A two-dimensional plane mesh represents the coating consisting of two triangles.

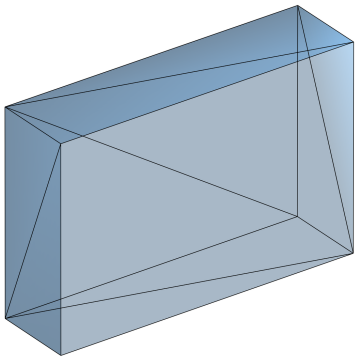

Figure 3.7: An open cuboid mesh represents the substrate. Each face consists of two triangles. Two triangles in the front are missing, thus an open cuboid is formed.

The HBS is implemented by combining coating mesh and substrate mesh as shown in Fig. 3.8. The coating is placed such that the open surface is closed. The size of coating and substrate are coupled so that the size of the coating is always the same size as the missing face in the substrate mesh. The dimensions of the HBS in height, width, and substrate

thickness are specified when first initialized by the user. To determine the reflected or transmitted wavelengths the digital HBS model stores this data in two tuples. Wavelengths specified in the first tuple will be reflected whereas wavelengths in the second tuple will be transmitted. This order is chosen arbitrarily and could also be implemented by other means. If a light beam intersects with the coating mesh it is checked whether the light beams wavelength is contained in the first or second tuple of the harmonic vector. The light beam is then either reflected or transmitted. If a light beam with a wavelength not specified in the harmonic vector intersects the coating no further tracing of this beam is calculated and the trace is stopped. In the case that the beam is transmitted by the coating, refraction occurs instantly at the coating surface with the refractive index n of the HBS substrate, which is also a customizable parameter provided by the user. This can be justified by assuming that the coating thickness is negligible compared to the substrate thickness. A second refraction takes place if the transmitted light beam leaves the substrate. Each refraction direction is calculated with Snell's law. This is visualized in Fig. 3.9.

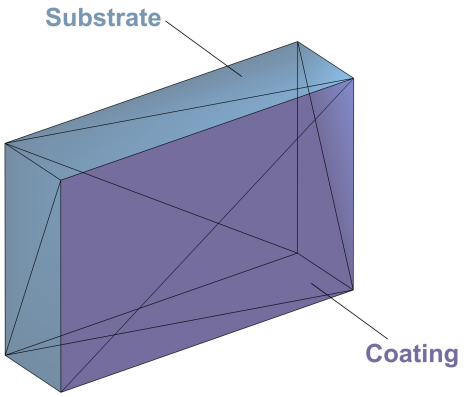

Figure 3.8: The HBS is modelled by the coating and the substrate resulting in a closed cuboid surface.

In total two HBS are used in the digital twin corresponding to the setup in Fig. 2.2. They are denoted as HBS1 and HBS2. The dimensions of the HBS used in the digital twin are derived from real-world HBS of the current dispersion interferometer setup. The current experimental setup of the dispersion interferometer features Thorlabs HBSY11 and HBSY12 as depicted in Fig. 3.5. They are circular with a diameter of 1 inch and have a thickness of 5.0 mm [19]. The modelled HBS have the same substrate thickness as the real-world components. Instead of a circular shape a quadratic shape is used due to the discretization with mesh triangles. The material used for the substrate is quartz glass, which is characterized by the refractive index $n(\lambda)$ [20]. The parameters of the HBS used in the digital twin are listed in Tab. 3.2. The digital HBS models are planar on front and back surface compared to the Thorlabs HBS, which feature a 30 arcmin wedge on the backside. Another difference is that reflection and transmission are lossless for the digital HBS model, thus no reflectance or transmission coefficients are used.

3.2.2 Mirrors

Mirrors are part of the SCDI package. They are implemented either by a planar two-dimensional mesh or a rectangular cuboid mesh. In both cases the mesh is composed by

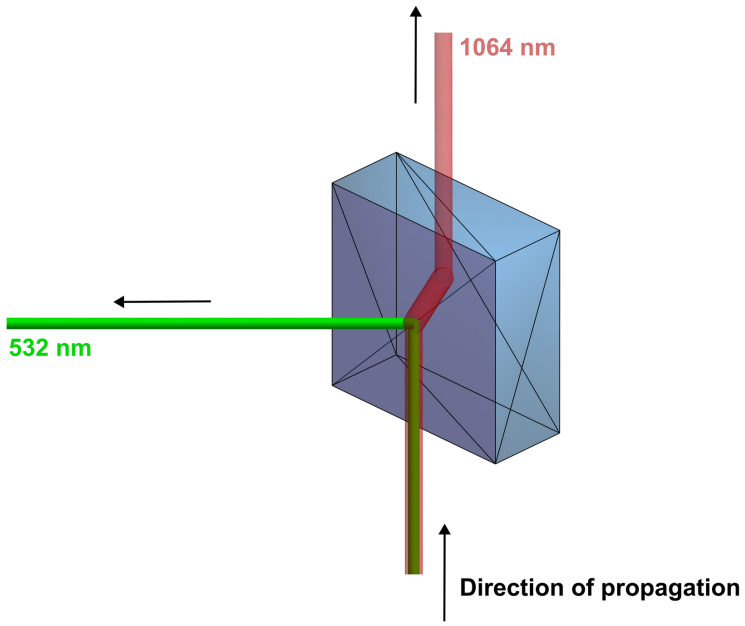

Figure 3.9: The HBS1 model used in the digital twin and in simulations of the dispersion interferometer. The two coaxially aligned beams are separated with HBS1. The coating of a HBS either reflects or transmits beams depending on the beams wavelength. In this case the green light beam is reflected whereas the red beam is transmitted. If a beam is transmitted refraction occurs twice. Once directly at the coating, a second time when leaving the substrate.

Table 3.2: Harmonic beam splitters parameters used in the digital twin

Parameters	HBS1	HBS2
Substrate thickness	5.0 mm	
Height and width	1 inch	
Refractive index $n(\lambda_\omega)$	1.4496	
Refractive index $n(\lambda_{2\omega})$	1.4607	
Reflected wavelengths	532 nm	1064 nm
Transmitted wavelengths	1064 nm	532 nm

triangles. In Fig. 3.10 a planar mesh mirror and in Fig. 3.11 a rectangular cuboid mesh mirror is shown. The dimensions can be adjusted by the user upon creation.

In practice mirrors are coated with highly reflective surfaces to achieve reflectance $\geq 90\,\%$. The reflectance not only depends on the coating but also the wavelength of the incident light. This can be seen in Fig. 3.12 and in Fig. 3.13 where the reflectance characteristics of two mirror coatings by the company Thorlabs are plotted [21]. The angle of incidence (AOI) for both plots is 8°. The -K13 coating is specified for dual order applications, meaning it is designed to reflect 532 nm and 1064 nm, while the -K12 coating is designed and optimized for the the reflection of 532 nm. One can see that the K12 coating performs better for 532 nm because it is designed solely for that wavelength.

The mirror models provided by the SCDI package are ideal such that the reflection introduces no losses of any kind. The mirrors reflectance also does not depend on the wavelength of the incident light beam. Each beam is treated equally and redirected based

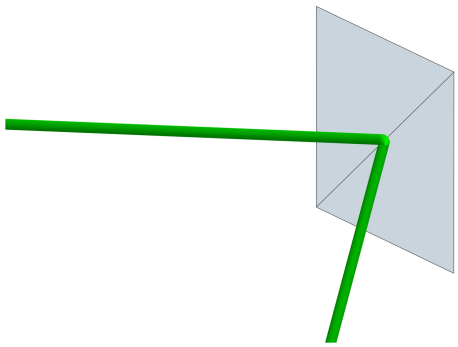

Figure 3.10: A planar mesh mirror consists of two triangles, which form a rectangular mesh. The beam is reflected by the mirror.

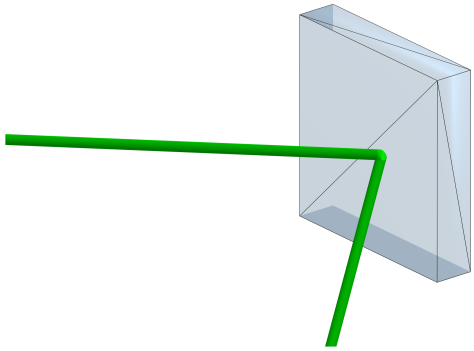

Figure 3.11: A cuboid mesh mirror consists of six faces, each consisting of two triangles, resulting in 12 triangles. The beam is reflected by the mirror.

on the laws of reflection. This equals a reflectance of 100 % for any light beam.

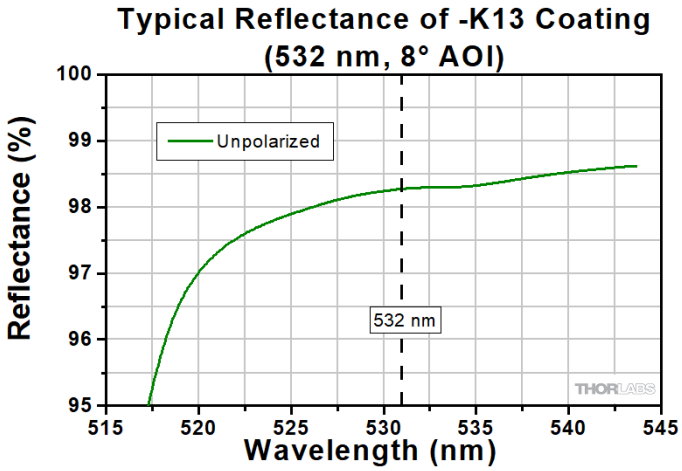

Figure 3.12: The reflectance of a dual order mirror to reflect wavelengths of 532 nm and 1064 nm. Shown is the reflectance curve for unpolarized light. Reflectance values $\geq 95\,\%$ are achieved [21].

In the interferometer digital twin four mirrors are used. They are denoted as M1, M2,

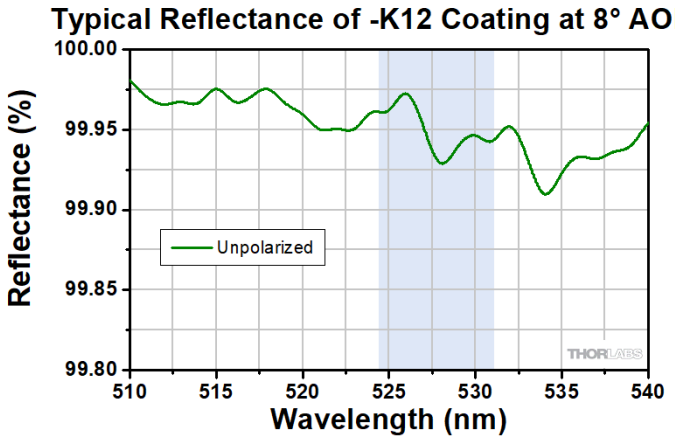

Figure 3.13: The reflectance of an optimized coating for a wavelength of 532 nm. Reflectance values are $\geq 99.90\,\%$ [21].

M3, and M4. M1 and M2 are necessary to complement HBS1 and HBS2, see the setup of the interferometer in Fig. 2.2. They are implemented by planar mesh mirrors. The mirrors M3 and M4 are required to pick-up and redirect the diffracted reference beams, such that they are directed onto the PD. This is also visible in Fig. 2.2. M3 and M4 are implemented respectively by a cuboid mesh mirror. The dimensions of the mirrors M1 to M4 are derived from the real-world mirrors used in the current experimental setup. They mostly feature a 1 inch diameter. Due to discretization instead of circular shaped mirrors rectangular mirrors were used. The substrate thickness does not effect the propagation path for mirrors. Every cuboid mesh mirror can be replaced by a planar mesh mirror. However, using the volume models is useful to check dimensions in a digital twin to analyse if boundaries of components are intersected. The mirror parameters used in the digital twin are listed in Tab. 3.3.

Table 3.3: Mirror parameters used in the digital twin

Parameters	M1	M2	M3	M4
Substrate thickness	-	-	5.0 mm	5.0 mm
Height	1 inch	1 inch	0.5 inch	1 inch
Width	1 inch			
Reflectance	100 %			

3.2.3 Acousto-optic Modulator

An AOM is often used to diffract light and thus to deflect light. In other applications it can be utilized to apply a frequency shift. In Ch. 2.2.1 the general operating principles of an AOM are described. For the digital twin it was necessary to implement an AOM model.

To implement the AOM model close to the real-world the digital model was derived from the one used in the experimental setup. The laboratory setup features an AOM by the company Castech. The data sheet of the AOM by Castech is provided in Appendix A. Castech also supplies a computer-aided design (CAD) model of the AOM including the casing and the quartz crystal of the AOM.

The quartz crystal geometry was extracted from the supplied CAD model and converted to a standard triangle language (STL) file. The SCDI API provides an interface to read in and convert a STL file to a triangle mesh for ray tracing applications. This interface

was used to import the STL quartz crystal geometry into the digital twin. In Fig. 3.14 the used mesh of the quartz crystal for ray tracing is shown. It is visible that the quartz crystal is a hexahedron. The light enters the front surface, is diffracted inside the quartz crystal, and exits at the back surface. One can see that the front and back surface differ in size because of the wedged side face on the left.

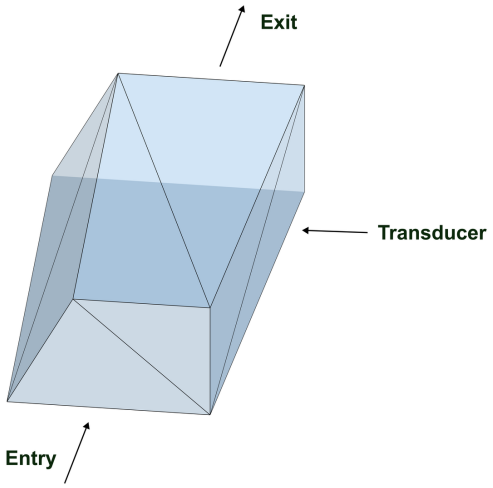

Figure 3.14: The mesh of the AOM quartz crystal used in the digital twin and in simulations. Each face of the mesh consists of two triangles. The triangle edges are marked with black lines.

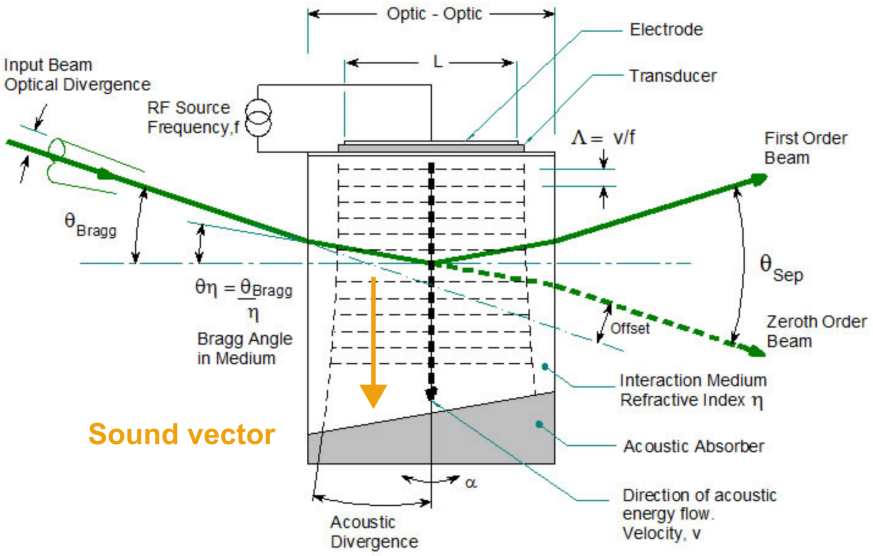

Figure 3.15: The input beam propagates and intersects the AOM crystal. It is refracted at the incident surface. The sound waves inside the crystal move in a column and lead to the generation of a first order diffracted beam. The zeroth order beam is solely refracted. Here the deflection angle α outside of the quartz crystal is denoted as θ_{Sep} [22].

To model the AOM two important effects were considered, i.e. refraction and diffraction.

In the case of the AOM, refraction occurs at the incident surface, where a light beam enters the AOM and at the exit surface where a light beam leaves the AOM. The computation of refraction is based on Snell's law.

The diffraction occurs inside of the AOM, caused by the applied radio frequency Ω, which leads to the generation of sound waves inside the AOM quartz crystal. In Fig. 3.15 refraction and diffraction are visualized [22]. The implementation of the diffraction inside the AOM quartz crystal is based on the vector formalism provided by Korpel introduced in Ch. 2.2.1. The direction of the diffracted light beams $\vec{s}_\pi$ can be calculated with the direction of the incident light beams $\vec{s}_o$ and the direction of the sound vector inside the quartz crystal $\vec{s}_s$. The following equation relates these vectors

$$\vec{s}_\pi = m\frac{K}{k}\vec{s}_s + \vec{s}_o\,, \tag{3.5}$$

where m is the order of diffraction and k is defined as

$$k = \frac{n}{\lambda} \tag{3.6}$$

with refractive index n of the quartz crystal and wavelength λ of the light beam. K is defined as

$$K = \frac{\Omega}{c_s} \tag{3.7}$$

with the applied radio frequency Ω and c_s the speed of sound inside the quartz crystal. $\vec{s}_o$ and $\vec{s}_s$ must be unit vectors. The AOM is also responsible for the frequency shift of the diffracted beams see Eq. (2.32). This leads to the simulation of a heterodyne detection technique. The used method to simulate the frequency shift of the AOM in the time domain is later discussed in Ch. 3.5.3.

Diffraction occurs inside of the AOM quartz crystal where the sound waves move in a column. Because of this it was assumed that the incident beam $\vec{s}_o$ in Eq. (3.5) is not the beam, which intersects the AOM front surface, but the light beam directly after refraction at the interface. This is visualized in Fig. 3.15 where refraction takes place first. Thus the calculation of the refracted beam will occur first. The resulting refracted beam is then set as $\vec{s}_o$ used in Eq. (3.5) to determine the direction of the diffracted light $\vec{s}_\pi$.

The user must provide orders m in form of a function. For each simulated wavelength λ the function returns an one-dimensional array of orders. The reason for this implementation is the flexibility to simulate different orders for distinct wavelengths. This behaviour of simulating exclusively designated orders is not congruent to reality where generally speaking multiple orders will appear simultaneously. In case of the dispersion interferometer the first order diffraction for ω ($m = 1$), the second order for 2ω ($m = 2$) and the zeroth orders ($m = 0$) are of interest. Thus this approach is sufficient. Furthermore, it can be assumed that for practical applications only certain diffraction orders will be of relevance, which justifies this method as well.

The sound vector $\vec{s}_s$ is a fixed vector relative to the geometry of the quartz crystal. This is because the sound waves move in a column inside the crystal and thus the sound vector $\vec{s}_s$ depends on the orientation of the crystal. If the quartz crystal is rotated around an axis p with angle θ, the sound vector will also be rotated around p with θ. Because of this the sound vector is automatically determined at run time by exploiting the fact that the sound vector will always be parallel to the upper edge of the front surface. The advantage is that the user does not have to pass a sound vector manually while also keeping track of the quartz crystal orientation itself. In Fig. 3.16 the sound vector $\vec{s}_s$ for the used quartz crystal is shown. The sound waves move from the planar face on the right to the left wedged side

called absorber. The reader might notice that the direction of the diffracted orders differs in sign from the expected result in Eq. 3.5. In order to stay consistent with the established literature conventions, i.e. Fig. 3.15, the sign of m is flipped. The resulting order is shown in Fig. 3.16. Positive and negative orders are symmetric to the zeroth order.

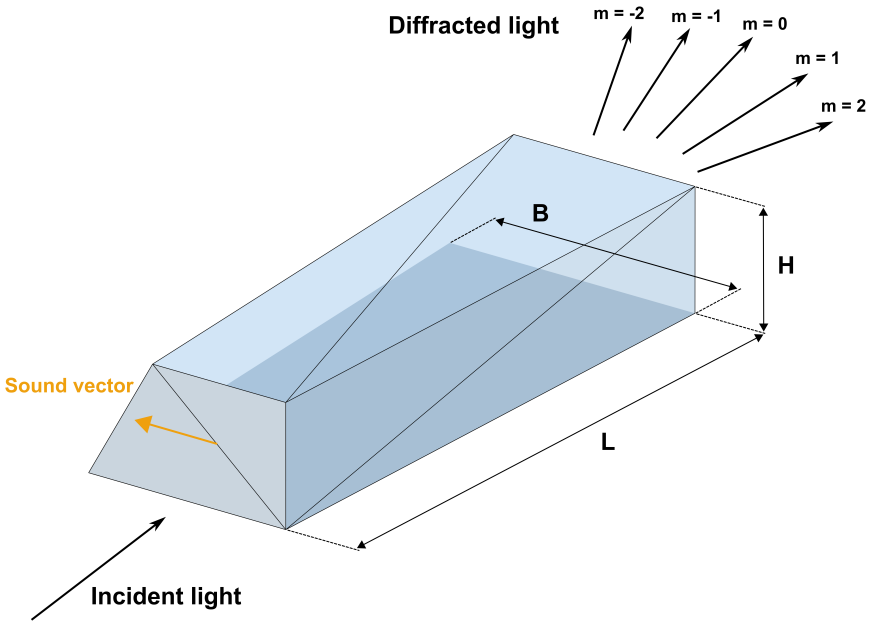

Figure 3.16: The orange sound vector $\vec{s}_s$ represents the direction of acoustic modulation. The sound vector is fixed to the geometry of the quartz crystal. Diffracted light occurs in orders m. The non-diffracted order $m = 0$ only experiences refraction.

The refractive indices n of the quartz crystal for each wavelength were taken from a database, under consideration of the interaction material provided by Castech, see Appendix A [20]. Typical speed of sounds c_s range between 5700 $\frac{\text{m}}{\text{s}}$ and 5800 $\frac{\text{m}}{\text{s}}$ for quartz [23, 24, p. 2]. To fit the diffraction angle to the ones provided by Castech in Appendix A all parameters were held constant and the speed of sound c_s was slightly varied between 5700 $\frac{\text{m}}{\text{s}}$ and 5800 $\frac{\text{m}}{\text{s}}$. A good fit was found with $c_s = 5740\,\frac{\text{m}}{\text{s}}$. One source also states this value as the nominal value of c_s for longitudinal waves in quartz glass [25]. In Tab. 3.4 parameters as well as the overall dimensions of the AOM quartz crystal used for the computation of the diffracted beams are given.

Table 3.4: Acousto-optic modulator parameters used in the digital twin

Parameters	ω	2ω
Wavelength λ	1064 nm	532 nm
Refractive index $n(\lambda)$	1.4496	1.4607
Simulated orders m	[0, 1]	[0, 2]
Speed of sound c_s	5740 $\frac{\text{m}}{\text{s}}$	
Applied radio frequency Ω	80 MHz	
Dimensions overall [L x B x H]	35 mm x 15.5 mm x 7 mm	

The deflection angle inside and outside of the quartz crystal relative to the non-diffracted beam can be calculated analytically by hand for each wavelength λ and order m with Eq.

(2.31). For order $m = 0$ no diffraction is present and the non-diffracted beams, also called zeroth-order beams are only refracted by the quartz crystal. With Eq. (2.31) this gives for ω and $m = 1$ inside the AOM quartz crystal

$$\alpha_{\omega_{\text{inside}}} = \frac{m \cdot \frac{\lambda_\omega}{n_\omega} \cdot \Omega}{c_s} = \frac{1 \cdot \frac{1064\,\text{nm}}{1.4496} \cdot 80\,\text{MHz}}{5740\,\frac{\text{m}}{\text{s}}} = 10.23\,\text{mrad} \tag{3.8}$$

and outside for ω

$$\alpha_{\omega_{\text{outside}}} = \frac{m \cdot \lambda_\omega \cdot \Omega}{c_s} = \frac{1 \cdot 1064\,\text{nm} \cdot 80\,\text{MHz}}{5740\,\frac{\text{m}}{\text{s}}} = 14.83\,\text{mrad}\,. \tag{3.9}$$

For 2ω and analogous proceeding using the second diffraction order $m = 2$ yields the diffraction angle inside

$$\alpha_{2\omega_{\text{inside}}} = \frac{m \cdot \frac{\lambda_{2\omega}}{n_{2\omega}} \cdot \Omega}{c_s} = \frac{2 \cdot \frac{532\,\text{nm}}{1.4607} \cdot 80\,\text{MHz}}{5740\,\frac{\text{m}}{\text{s}}} = 10.15\,\text{mrad} \tag{3.10}$$

and outside of the quartz crystal

$$\alpha_{2\omega_{\text{outside}}} = \frac{m \cdot \lambda_{2\omega} \cdot \Omega}{c_s} = \frac{2 \cdot 532\,\text{nm} \cdot 80\,\text{MHz}}{5740\,\frac{\text{m}}{\text{s}}} = 14.83\,\text{mrad}\,. \tag{3.11}$$

One can see that despite the slightly different diffraction angles $\alpha_{\omega_{\text{inside}}}$ and $\alpha_{2\omega_{\text{inside}}}$ inside the quartz crystal the same diffraction angles outside of the AOM occur. This is because the diffraction angle outside of the AOM does not depend on the refractive index n of the quartz crystal. The dispersion interferometer exploits that due to the Bragg equation outside of the AOM $\alpha_{\omega_{\text{outside}}}$ equals $\alpha_{2\omega_{\text{outside}}}$ [5].

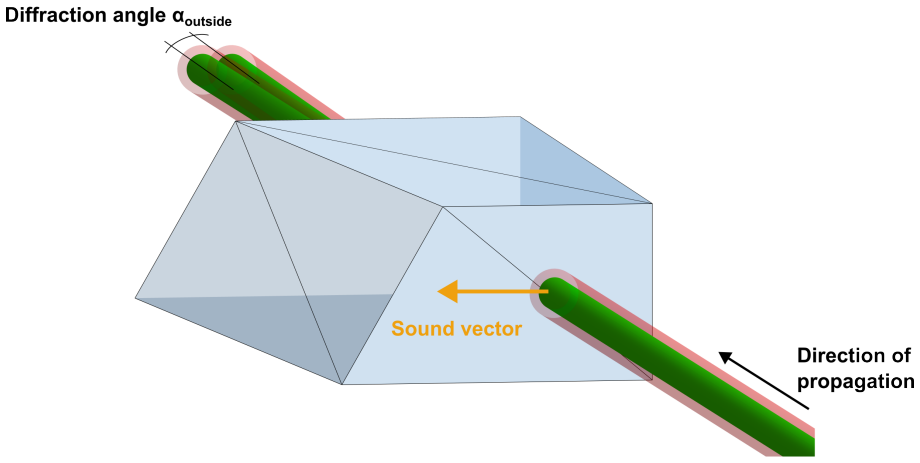

Figure 3.17: Diffraction in AOM quartz crystal. The orange sound vector leads to the diffraction. Two non-diffracted beams and two diffracted beams of order $m = 1$ and $m = 2$ with the same diffraction angle beams leave the AOM.

To verify the ray tracing procedure for the AOM the angles were also measured in the simulation. The diffracted beams are spawned according to Eq. (3.5) relative to the refracted beam. This is visualized in Fig. 3.17. The numerical ray tracing angle values rounded to four significant digits are for ω $\alpha_{\omega_{\text{inside}}} = 10.23\,\text{mrad}$ and $\alpha_{\omega_{\text{outside}}} = 14.83\,\text{mrad}$. For 2ω the simulation yields $\alpha_{\omega_{\text{inside}}} = 10.15\,\text{mrad}$ and $\alpha_{\omega_{\text{outside}}} = 14.83\,\text{mrad}$. The values

correspond to the analytical calculations in Eq. (3.8) to (3.11).

The limits of the AOM implementation are that the diffraction efficiency is not considered. The diffraction efficiency gives information about the optical power of the output beams. Diffraction efficiency depends on the absorption inside the crystal, losses at coated surfaces of the crystal, but also the AOI as well as the applied radio frequency power. In simulations of the digital twin the power of the output beams is distributed, such that for k simulated orders each beams intensity will be scaled to $\frac{1}{k}$ of the input beam. For example, simulating the zeroth and first order results in halved intensity, if three orders are spawned the scaling factor is $\frac{1}{3}$ and so on. While it does not represent the real power outputs, this simple assumption is sufficient for the conducted simulations.

3.2.4 Retroreflector mirror

Retroreflector mirrors are optical components consisting of three perpendicular mirrors. They reflect a light beam such that the outgoing direction of the light beam equals the incident direction, in addition to a parallel offset. In the experimental setup a hollow RR by the company Thorlabs is used. In Fig. 3.18 such a hollow RR is depicted [26].

Figure 3.18: Hollow RR by Thorlabs similar to the one used in the laboratory setup of the interferometer [26].

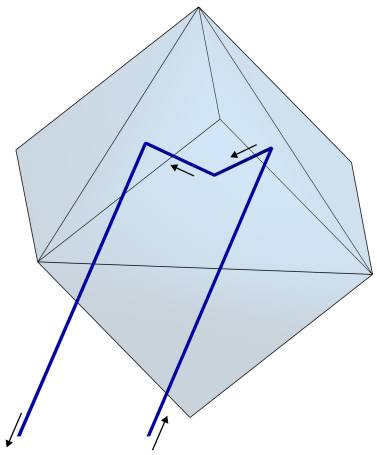

Figure 3.19: The retroreflector mesh consists of three orthogonal planar meshes. Each planar mesh consists of two triangles.

To implement the retroreflector a custom RR mesh was designed. Three planar meshes are assembled such that they are orthogonal to each other, see Fig. 3.19. Each planar mesh consists of two triangles. The dimensions of the RR mesh are uniform, meaning that all outer edges are of same length. A single size parameter must be passed when creating the RR, which sets the length of the outer edges to the desired value. The incident light beam is reflected from the first surface to the second and subsequent third surface. In the end, the beam propagates in the same direction it came from but with an parallel offset. Analogous to the mirrors surface properties, the RR features a reflectance of 100 % on each surface, which is an idealized assumption. In the setup of the digital twin the RR was used with an initialized edge length of 8 cm.

3.2.5 Plate Beam Splitter

Plate beam splitters consist of a plate in contrast to cube beam splitters which feature a cube form. In Ch. 2.2.2 a general description of beam splitters and their properties is given. While there are two HBS in the setup of the interferometer only one PBS is present. The PBS is necessary to realign the reference and probe beams such that they are coaxially orientated for each wavelength when they impinge on the PD, see Fig. 2.2. In the experimental setup of the interferometer a PBS by the company Thorlabs is used. The PBS is designated for 50:50 power splitting. In Fig. 3.20 an exemplary PBS for 50:50 power splitting is shown [27].

Figure 3.20: Plate beam splitter by Thorlabs for 50:50 power splitting [27].

Table 3.5: Plate beam splitter parameters used in the digital twin

Parameters	PBS
Substrate thickness	5.0 mm
Height	1 inch
Width	1 inch
Refractive index $n(\lambda_\omega)$	1.4496
Refractive index $n(\lambda_{2\omega})$	1.4607
Reflectance to transmittance ratio	50:50

The implementation of the PBS is similar to the HBS. A two-dimensional coating mesh and an open cuboid substrate mesh are used equivalent to the meshes depicted in Fig. 3.6 and Fig. 3.7. However, in the case of the PBS the light for any wavelength is partially reflected and transmitted, see Fig. 3.21. The amount of reflected and transmitted power depends on the coating of the PBS. A power splitting ratio of 50:50 means, that the reflected and the transmitted beam will each be half of incident beam power, while 30:70 means that the reflected beam will have 30 % and the transmitted beam 70 % of the power of the incident beam. The user can provide any reflectance value $0 < r < 1$. Because of

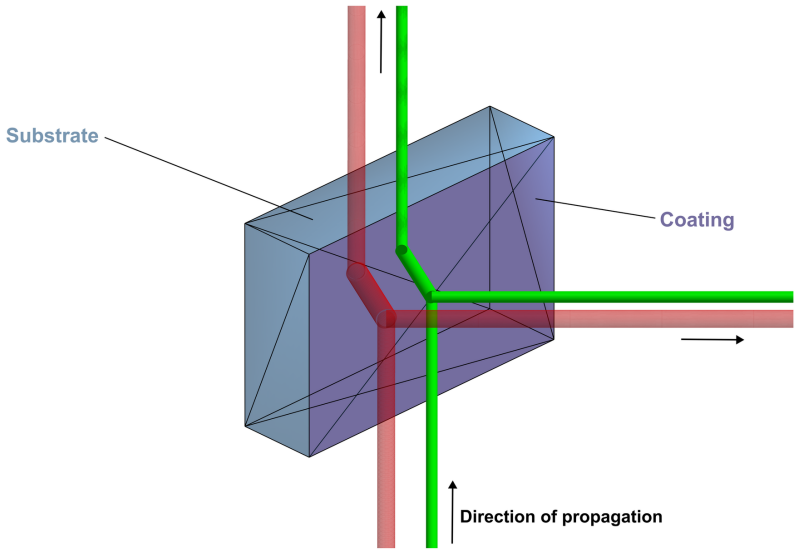

Figure 3.21: PBS model consisting of coating and substrate. The incoming beam intersects the coating of the PBS. The beam is partially reflected and transmitted. Refraction occurs twice, once instantly at the coating, and a second time, when leaving the substrate.

energy conservation the transmittance value is $t = 1 - r$ and automatically calculated at initialization. The dimensions of the PBS and the refractive index n of the substrate are also required upon initialization. Refraction occurs instantly at the coating and when leaving the PBS, analogous to the HBS model. The parameters used for the PBS in the digital twin are derived from real-world components and listed in Tab. 3.5.

3.2.6 Photodetector

The PD is part of the interferometer setup. In Fig. 3.22 a PD similar to the one used in laboratory setup is shown [28]. The PD does not alter the propagation path of the laser beams unlike previous components, albeit it measures the incident optical power. Parameters such as rise time, detectable bandwidth or responsivity are determining the choice of a PD for applications.

The SCDI package features the implementation of a PD. It consists of two equally sized mesh triangles which form a square shown in Fig. 3.23. After ray tracing, the electric field E can be evaluated at the intersection plane of the PD. This is achieved by calculating the electric field values $E(r, z)$ for the coordinates r, z according to Eq. (2.36) within the PD plane. For this the PD area is discretized. The parameters resolution and size are used for discretization of the PD and must be passed by the user. The resolution parameter squared equals the total count of discretized values. The size parameter determines the overall dimensions of the PD area. To initialize the PD an edge length of 10 mm and a resolution parameter of 500 was chosen, meaning the intensity array is of size $500 \cdot 500$ and contains therefore 250 000 values. After obtaining the discretized electric field E in form of an array it is converted to the intensity distribution I with Eq. (2.42), which is also an array. Integrating the intensity I over the PD area gives the resulting power P, see Eq. (2.43). This is visualized in Fig. 3.2 where the intensity distributions of the spawned beams were shown. If the beam spot size at the photodetector is significantly greater than the area of the PD, it must be considered that the intensity distribution is only partially resolved and the optical power is underestimated. The PD allows not only to capture the intensity

Figure 3.22: PD by Thorlabs. The material of the PD measurement surface is Silicon (Si). The total detection surface of the PD, which is positioned centred in the aperture, is approximately 1 mm^2 and thus relatively small compared to the casing. Two ports on the top are for power supply and the output signal of the PD [28].

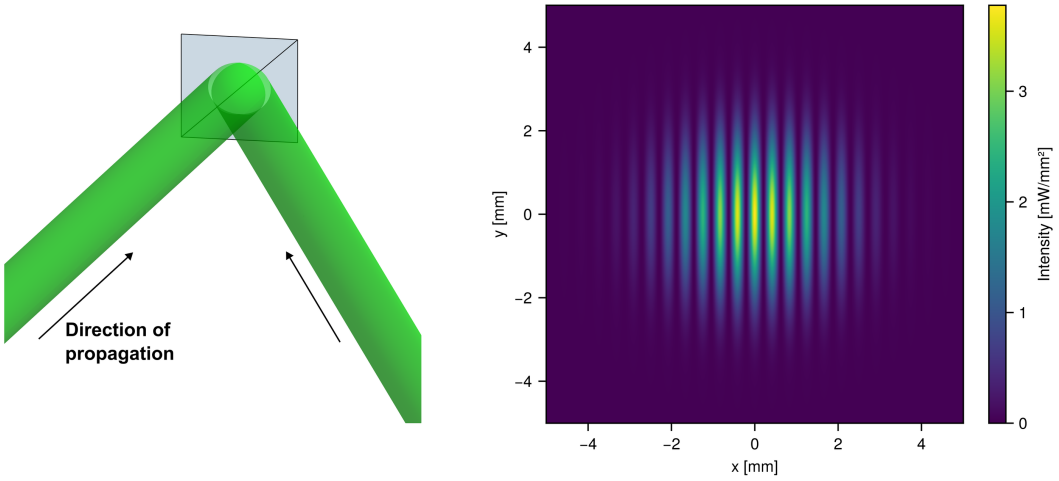

Figure 3.23: On the left: The PD is a planar mesh and consists of two triangles forming a square. Two coherent laser beams intersect the PD plane under an angle β. The superposition of the electric fields in the PD plane and the subsequent calculation of the intensity distribution leads to the interference pattern shown on the right.

distribution of one Gaussian beam but also the numeric superposition of electric fields and thus interference patterns. A necessary condition to observe interference is coherence between light beams. With this it is possible to investigate three major spatial interference effects due to differences in the phase fronts. Those are angular deviations, translation offsets or different OPL. All three effects are automatically captured by the superposition of electric fields with the PD. It is important to note that the field values are modelled as a scalar quantity. In order to account for the vectorial nature of field superposition, geometric considerations are used to adjust for this. In Fig. 3.23 two beams intersect the PD plane under an angle β. Because the laser beams are coherent an interference pattern

forms, which can be seen on the right in the intensity distribution. Because the PD can not differentiate which light beams are coherent to each other it is the responsibility of the user to only obtain the superposition and interference of coherent light beams. For the digital twin interferometer it is therefore necessary to separate the superposition of the electric fields for ω and 2ω. This can be implemented by either ray tracing first one wavelength, reading out the PD field, then removing the intensity distribution by resetting all intensity field values to zero and then tracing the next Gaussian beam. Alternatively, a HBS could be used to separate the beams to read out two PD areas. For the simulation the first option was used.

3.3 Setup of Digital Twin

The setup of the digital twin consists of the optical components described in the previous chapters and is based on the SDI, which was elaborated in Ch. 2.1.1. The two spawned laser beams were described in Ch. 3.1. In total 10 optical components are used. That are two HBS, four M, one AOM, one RR, one PBS and one PD. To set up the digital twin a position and orientation for each component must be chosen in a global coordinate system. The objective of setting up the digital twin was to adjust the interferometer, meaning that the laser beams are in a nominal state without any deviations and that reference and probe beams impinge the PD nearly coaxially aligned.

The laser beams of frequency ω and 2ω are spawned in the direction of the global x-axis [1 0 0] and propagate in the x-y plane if no deviations are introduced. Because of this the optical components are solely positioned in the x-y plane and no translation in the direction of the z-axis is carried out. Thus the global z-coordinate for each component is $z = 0$. To alter the laser beams propagation direction components were rotated around the vertical z-axis. In Fig. 3.25 the setup of the digital twin is depicted with the exception of the RR. For visualization purposes CAD files provided by Thorlabs including mounts and posts were rendered after ray tracing instead of the actual digital representation of each model. This is shown exemplary for HBS1 in Fig. 3.24, which corresponds to the model in Fig. 3.9.

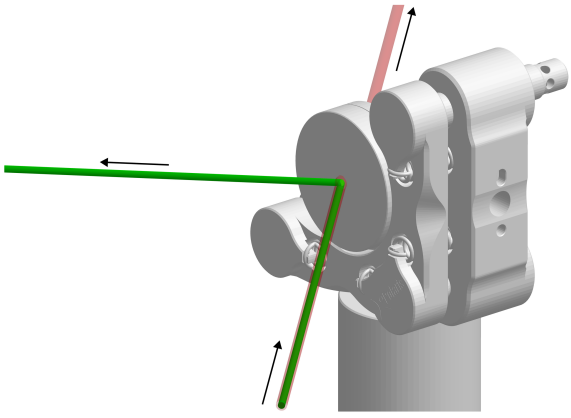

Figure 3.24: The HBS1 is rendered with a CAD file including a mount and a post after simulation. The actual model used for ray tracing is the one in Fig. 3.9.

The setup of the digital twin in Fig. 3.25 is essentially the same setup as the experimental setup in Fig. 2.2. However, it is visible that the setup differs slightly from the experimental one. The unit HBS1 and HBS2 with M1 and M2 is positioned in the positive y-direction compared to the negative y-direction in Fig. 2.2. This choice was made to eliminate any

possible effects of self-interaction, meaning that the beams coming from the RR and passing the PBS do not interact with an optical component any further. In reality a beam dump, barrier or casing wall is placed behind the PBS to prevent this. The general operating principle of the dispersion interferometer remains the same.

Separation of ω and 2ω occurs at $x_{\mathrm{HBS1}} = 10\,\mathrm{cm}$ to align both beams with HBS1, HBS2, M1 and M2. This is necessary since the beams are emitted with different angles by the DPSSL due to spatial walk-off effects. The positions of HBS1, HBS2, M1 and M2 form a square with an edge length of $l_0 = 10\,\mathrm{cm}$. Both HBS and M are each diametrically opposed. The reason for choosing 10 cm as a base length originates from the experimental setup. Components are mounted with posts on an optical table. These posts can be screwed in threaded holes and the nearest spacing between these holes is 1 inch. A practical distance for mounting optical components is then a clearance of 5 spanning threaded holes including the mount holes. This equals 4 inches $\approx$ 10 cm and allows to mount components in a convenient way. A spacing distance of 10 cm is also sufficient to place filters or other devices in between the components. In order to simplify the digital setup, both beams are initialized coaligned to the global x-axis, hence HBS1 is rotated $-45°$ and HBS2 135° around the global z-axis [0 0 1]. A positive degree rotation is equivalent to a counter-clockwise rotation around the axis, while a negative degree rotation is a clockwise rotation. Because M1 and M2 are initialized with a different default orientation than the HBS they must be rotated with the angles listed in Tab. 3.6.

The refractive index of ω and 2ω in quartz is slightly different. Each beam is refracted twice when passing a HBS substrate. This causes a small parallel offset in the y-direction between the laser beams of ω and 2ω after HBS2 and before diffraction inside the AOM. This parallel offset between ω and 2ω is first maintained and then further altered by refraction at the AOM and at the PBS. The parallel offset in the digital twin after HBS2 is $\Delta y = 19.63\,\mu\mathrm{m}$. The analytical beam displacement D can be calculated by

$$D = T \cdot \sin\theta \left(1 - \frac{\cos\theta}{\sqrt{n^2 - \sin\theta}}\right), \tag{3.12}$$

with substrate thickness T, refractive index n and AOI θ [29]. Using the specific parameters gives

$$\Delta y = D_\omega - D_{2\omega} = 19.63\,\mu\mathrm{m} \tag{3.13}$$

which equals the value obtained by the digital twin. One can see that the introduced parallel offset between ω and 2ω does not depend on the length l_0. However, it is more of interest how well reference and probe beam for each wavelength are aligned. This is controlled by the position and orientation of M3 and M4 primarily.

After separation and reunion of ω and 2ω the AOM follows. The AOM quartz crystal is initialized with a default translation. This is because for AOM applications it is desirable that the incident beam intersects the AOM in the aperture region. If no default translation would be applied, the beams would intersect the AOM crystal at the front surface in the right lower corner and no reasonable diffraction would be calculated. In Appendix A, Castech states that the active aperture is 3.0 mm wide. With the provided dimensions in the data sheet and the CAD file a default translation of 3.5 mm in the negative z-direction and 3.5 mm in the negative y-direction of the AOM crystal is applied. Additionally, HBS1 and HBS2 lead to a global parallel offset $D_\omega \approx D_{2\omega} \approx 1.6\,\mathrm{mm} \approx 2\,\mathrm{mm}$ caused by refraction, thus the AOM is moved 2 mm in the negative y-direction relative to the y-position of HBS2 to $y_{\mathrm{AOM}} = 9.8\,\mathrm{cm}$. With this it is ensured that the incident beams intersect the AOM crystal within the aperture region. The AOM is positioned 10 cm behind HBS2 at $x_{\mathrm{AOM}} = 30\,\mathrm{cm}$. The AOM diffracts the incident beams thus creating the zeroth-order

probe beams and the deflected reference beams. The deflected beams are of order $m = 2$ for 2ω and $m = 1$ for ω, thus having the same nominal diffraction angle of $\alpha = 14.83\,\text{mrad}$ as calculated in Eq. (3.9) and Eq. (3.11). It was observed in the laboratory that the AOM must be rotated around the vertical z-axis with a relative small angle approximately 6 to 7 mrad to obtain the diffracted beams. This is because the Bragg Eq. (2.31) holds true if the AOI equals half the diffraction angle α. To account for this effect, the AOM was rotated half the diffraction angle $\frac{\alpha}{2} = -\frac{14.83}{2}\,\text{mrad}$ around the z-axis in the digital twin. With Eq. (2.32) the frequency shift is $m \cdot \Omega = 2\Omega = 160\,\text{MHz}$ for 2ω and $m \cdot \Omega = \Omega = 80\,\text{MHz}$ for ω. The implementation of time-domain frequency modulation is discussed in Ch. 3.5.3.

After passing the AOM, the diffracted reference beams are picked off by M3. To prevent partial clipping of the laser beams a significant distance of 50 cm after the AOM exit surface was chosen such that the diffracted beams are fully separated from the non-diffracted beams and their spots do not overlap. With the AOM crystal length $l_{\text{AOM}} = 35\,\text{mm}$ the x-position of M3 is then

$$x_{\text{M3}} = x_{\text{AOM}} + l_{\text{AOM}} + 50\,\text{cm} = 83.5\,\text{cm}\,.$$

The y-position is $y_{\text{M3}} = l_0 - 1.8\,\text{cm} = 8.2\,\text{cm}$ which is sufficient to prevent clipping. The rotation of M3 was chosen due to previous work to $90\,^\circ + 10.24\,^\circ = 100.24\,^\circ$ [30]. The RR is positioned 5 m behind the AOM exit surface at

$$x_{\text{RR}} = x_{\text{AOM}} + l_{\text{AOM}} + 5\,\text{m} = 533.5\,\text{cm}\,.$$

This position was chosen to ensure that the beam spot sizes have increased notably similar to the conditions in the laboratory. This is also visible in Fig. 3.25 where the radius of the returning probe beams differ from the outbound probe beams. This also guarantees that the probe beam length is at least three times greater than the Rayleigh length z_R for each wavelength, see Eq. (3.1) and Eq. (3.2). The y-coordinate of the RR is fixed at $y_{\text{RR}} = l_0 + 2\,\text{cm} = 12\,\text{cm}$ to reflect the probe beams.

The returning probe beams from the RR propagate in the negative global x-axis direction. The PBS is rotated $-135°$ to partially reflect the probe beams in the direction of the global y-axis $[0\,1\,0]$. The x-coordinate of the PBS was set $-10\,\text{cm}$ relative to M3 so that

$$x_{\text{PBS}} = x_{\text{M3}} - 10\,\text{cm} = 73.5\,\text{cm}\,.$$

This enforces a relative short reference beam path. The y-coordinate of the PBS was then levelled approximately to the y-coordinate of the returning probe beams propagating axis resulting in $y_{\text{PBS}} = 14.2\,\text{cm}$.

To align reference and probe beams finally M4 was rotated and displaced. First, M4 was roughly positioned so that a closed beam path from M3 via M4 to the PBS is formed. Then M4 was rotated iteratively until the reference beams propagated in the global y-direction $[0\,1\,0]$ parallel to the probe beams. This rotation iteration was conducted manually by hand. To ease this process the angle between reference and probe beams was automatically calculated for each iteration step. With this an ideal rotation angle of $-34.335°$ for M4 was determined. However, it must be noted that the precision of position and orientation in the digital twin is limited by machine precision. This allows to setup components with an accuracy which would be hardly achieved in a laboratory setup with standard equipment. Off the shelf kinematic mirror mounts by Thorlabs allow for instance, depending on the mount, a resolution of 8.3 mrad $\approx 0.48°$ or 13 mrad $\approx 0.75°$ per revolution of the adjustment screw [31, 32].

After rotating M4 to the desired orientation, thus resulting in parallel reference and

probe beams in the global y-direction [0 1 0], the x- and y-coordinates of M4 are required. To constrain this further the y-coordinate was set to $y_{\mathrm{M4}} = \frac{l_0}{2} = 5\,\mathrm{cm}$. Then, in an iterative procedure, similar to the rotation of M4, the x-position x_{M4} was altered to match the x-coordinate of the reference beams with the fixed probe beams. As a starting point the same x-coordinate as the PBS was used

$$\tilde{x}_{\mathrm{M4}} = x_{\mathrm{PBS}} = 73.5\,\mathrm{cm}\,.$$

The iteration for each adjusted position was conducted manually with an automated evaluation yielding the x-difference offset between reference and probe beam. While iterating it was observed that the parallel x-offset was in the magnitude of $D_\omega \approx D_{2\omega}$. This is naturally caused by the refraction in the PBS analogous to the earlier mentioned HBS. Thus an offset of 1.6 mm was set and the x-coordinate of M4 results in

$$x_{\mathrm{M4}} = x_{\mathrm{PBS}} - 0.16\,\mathrm{cm} = 73.34\,\mathrm{cm}\,.$$

The PD was then positioned such that the beams impinge roughly in the center of the PD area. In Tab. 3.6 the global x-coordinate, global y-coordinate and the global z-axis rotation angle is listed for each component. In Tab. 3.7 the parametrization according to elaborated values is listed.

Table 3.6: Global coordinates and rotation of components in setup of digital twin

Components	Global x-coordinate	Global y-coordinate	Global z-axis rotation angle
HBS1	10 cm	0 cm	−45 °
HBS2	20 cm	10 cm	135 °
M1	20 cm	0 cm	45 °
M2	10 cm	10 cm	−135 °
AOM	30 cm	9.8 cm	$-\frac{14.83}{2}$ mrad
M3	83.5 cm	8.2 cm	100.24 °
M4	73.34 cm	5 cm	−34.335 18 °
RR	533.5 cm	12 cm	135 °
PBS	73.5 cm	14.2 cm	−135 °
PD	73.52 cm	30 cm	0 °

Table 3.7: Parametric coordinates and rotation of components in setup of digital twin

Components	Global x-coordinate	Global y-coordinate	Global z-axis rotation angle
HBS1	l_0	0 cm	−45 °
HBS2	$2l_0$	l_0	135 °
M1	$2l_0$	0 cm	45 °
M2	l_0	l_0	−135 °
AOM	$3l_0$	$l_0 - 2\,\mathrm{mm}$	$-\frac{14.83}{2}$ mrad
M3	$3l_0 + l_{\mathrm{AOM}} + 50\,\mathrm{cm}$	$l_0 - 1.8\,\mathrm{cm}$	100.24 °
M4	$x_{\mathrm{PBS}} - 0.16\,\mathrm{cm}$	$\frac{l_0}{2}$	−34.335 18 °
RR	$x_{\mathrm{AOM}} + l_{\mathrm{AOM}} + 5\,\mathrm{m}$	$l_0 + 2\,\mathrm{cm}$	135 °
PBS	$x_{\mathrm{M3}} - 10\,\mathrm{cm}$	14.2 cm	−135 °
PD	$\approx x_{\mathrm{PBS}}$	$3l_0$	0 °

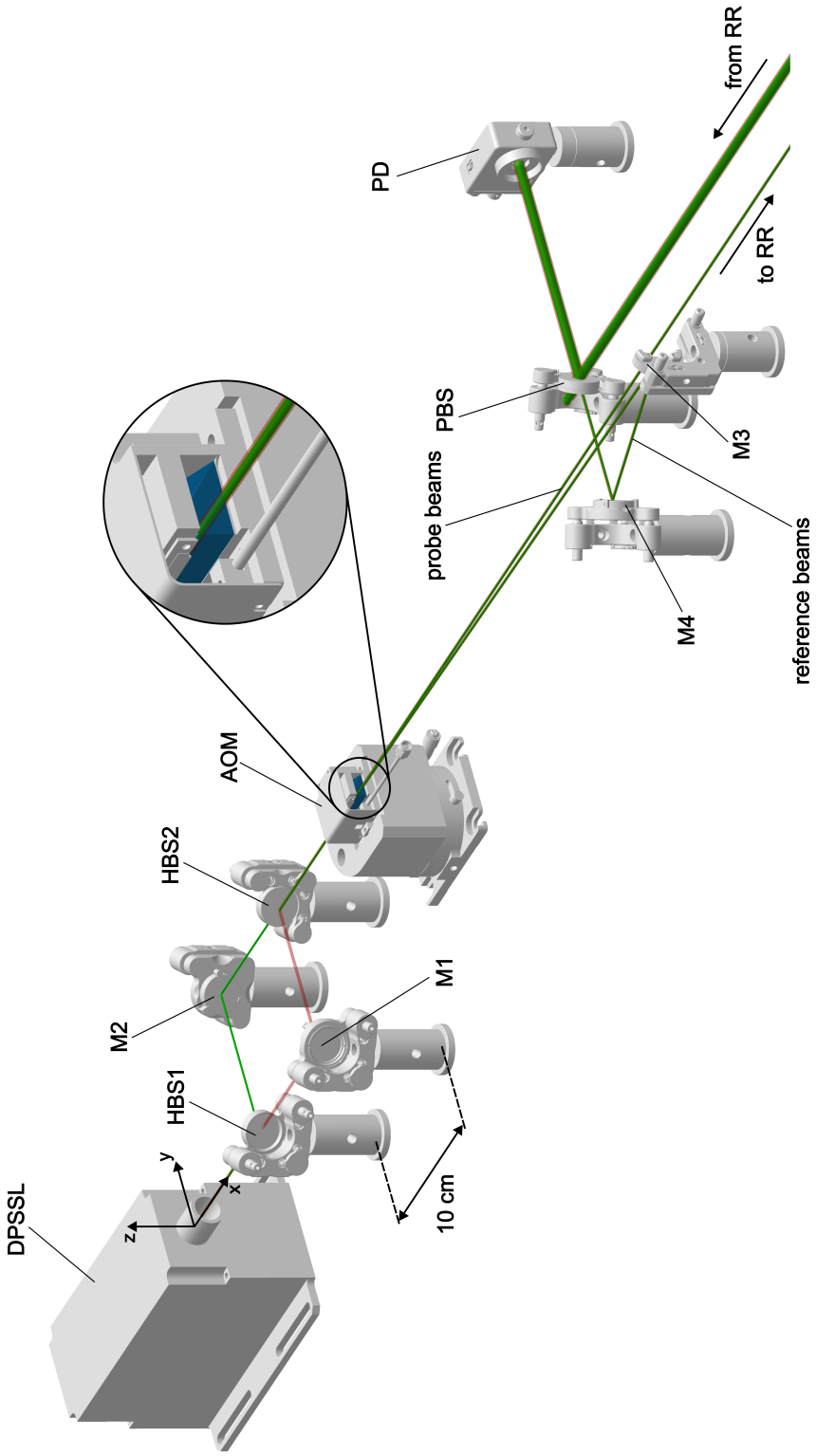

Figure 3.25: Rendering of the digital twin with auxiliary components. The AOM is placed on a rotation stage with a 3D printed mount to precisely rotate it. The quartz crystal of the AOM is colored blue. The NIR laser beam is colored red for visualization purposes. The retroreflector is not depicted.

3.4 Vibrations

Vibrations can be seen as translations or rotations in space. They can be abstracted as oscillations, often periodic in nature, which can be described by regular waves [33]. In Fig. 3.26 an oscillation is shown, where the displacement is a sinusoidal wave. Oscillations which can be described with a sine or cosine are also called harmonic oscillations [33]. An example for such an oscillation is a mass attached to a spring, where the mass is released from an initial displacement. The resulting motion is also called vibration response. The kinetic and potential energy of the mass are exchanged without losses in that case. However, in reality it can be observed that the displacement amplitude of the mass diminishes over time, as shown in the lower graph of Fig. 3.26. This is called damped oscillation. As already mentioned, vibrations are not exclusive to displacements but can also occur in a rotation motion where the oscillating quantity is the angle. A free-hanging pendulum which is deflected and then released would be an example for a rotating oscillation.

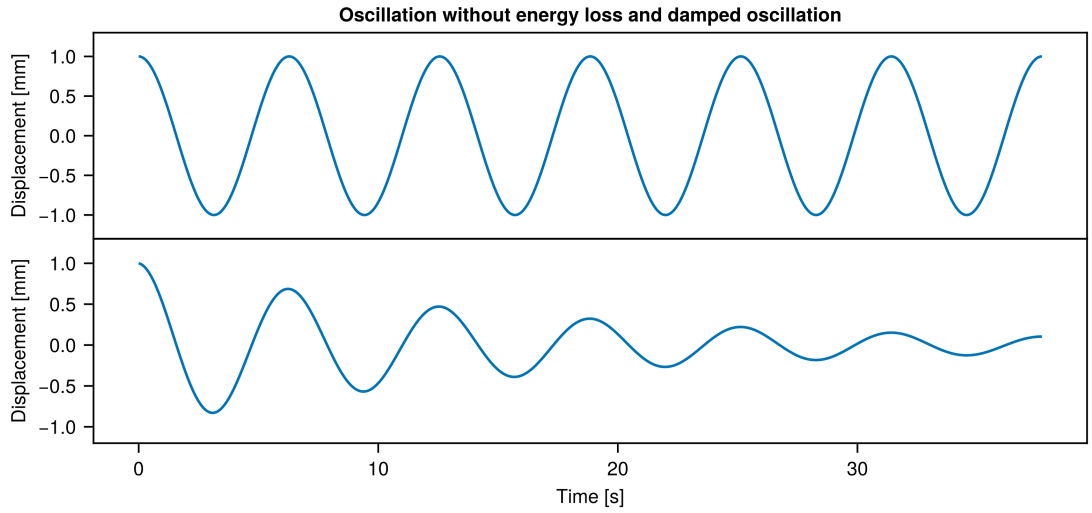

Figure 3.26: Examples of vibrations that are mechanical oscillations. Without energy losses the motion is periodic, whereas the amplitude of a damped oscillation will diminish.

In this work it was investigated how vibrations of the optical components in the digital twin affect the measurement results, particular the phase difference $\Delta\varphi$ in Eq. (2.8). It was especially of interest if and how each component influences the phase difference $\Delta\varphi$. The motivation behind this is to determine components which are likely to influence the sensor accuracy and initiate countermeasures in the design of the interferometer. Typical interferometers like the MI are sensitive to mechanical pertubations on the magnitude of the used laser wavelength. The advantage of the SDI is that two wavelengths are used. If vibrations contribute linear terms to the phase of each wavelength, the phase error will cancel out.

The vibration response of the interferometer includes the vibration motion for each optical component. This opens a great parameter space of possible displacements, rotations, and the combination of both. The resulting vibration response also depends on external excitement forces, the initial displacements, and the oscillation type itself [33]. To isolate these effects in the simulation, the vibration of each optical component was individually investigated. To model vibrations a harmonic oscillation of each component with a fixed vibration frequency and amplitude was assumed. Neglecting damped oscillations can be justified by the fact that displacements stemming from diminishing amplitudes are a subset

of a pure harmonic displacement oscillation. Generally speaking great displacements will impact the phase difference between reference and probe beam more than the diminishing amplitude of a damped oscillation. The vibration motion along the x-axis from an initial position can then be described for any optical component by

$$\Delta x(t) = \hat{x} \cdot \sin(2\pi f_x \cdot t)\,, \tag{3.14}$$

where $\hat{x}$ is the vibration displacement amplitude and f_x the vibration displacement frequency. For the rotation this is analogous with

$$\Delta\theta(t) = \hat{\theta} \cdot \sin(2\pi f_\theta \cdot t)\,. \tag{3.15}$$

where $\hat{\theta}$ is the vibration rotation amplitude and f_θ the vibration rotation frequency. Each optical component has six degrees of freedom (DOFs), three translations in the coordinate directions x, y and z and three rotations around the x, y and z-axis. However, not all translations and rotations are of interest. A change in interference and therefore a phase difference between reference and probe beams will be introduced in three cases, which are an angular deviation, a translation offset or a difference in OPL. It is therefore of interest to investigate the displacement and rotation axes in which these cases are significant. In Fig. 3.27 the scheme of an optical component is shown. As an example a mirror rotated around 45° is displayed. A red beam coming from the left is reflected by the mirror. The global coordinate system seen in Fig. 3.25 can be translated to every optical component in the digital twin such that the origin of the global coordinate system is identical with the components center of gravity. The global coordinate axes can then be denoted as x_G and y_G, whereas the local coordinates axes are coincident with the principal axes of the mirror and are denoted as x_L and y_L. The x_L-axis is by definition perpendicular to the incident surface. The z-axis is vertical to the drawing plane for both the global and local coordinate system.

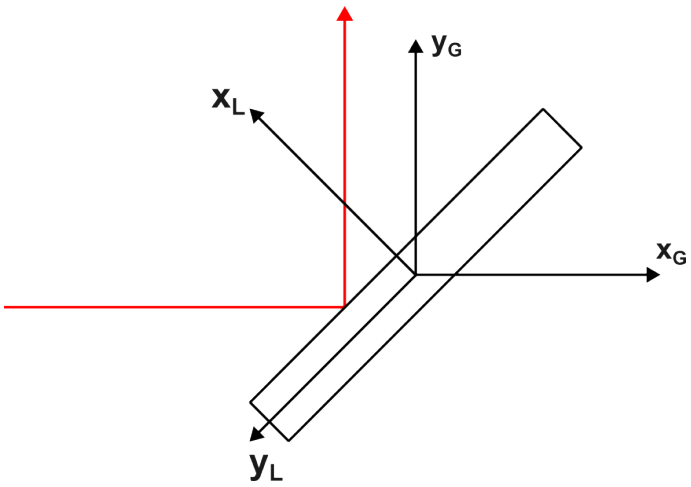

Figure 3.27: Top view of an exemplary component in the digital twin. The global x_G-axis is to the right and the global y_G-axis is upwards, see also Fig. 2.2. The z-axis is perpendicular to the drawing plane. The local coordinates axes x_L and y_L depend on the orientation of each component.

Moving the mirror Δx along the global x_G axis, as shown in Fig. 3.28, increases the geometrical path length by $2\Delta x$, thus increasing the OPL. Furthermore the reflected beam obtains a parallel translation shift of Δx. Moving the same distance Δx in the negative local x_L-axis direction will cause a parallel shift of $\sqrt{2}\Delta x$ and thus an additional $2\sqrt{2}\Delta x$ in

geometrical path length, increasing also the OPL. This shows that moving the component a certain distance Δx along the x_L-axis introduces a greater parallel shift and OPL increase than the same Δx displacement in global coordinates. Furthermore, translation in the direction of the y_L-axis leads to the same beam path. Translation in the global z-axis, which is the same as the local z-axis, does not lead to an altered beam path and is therefore also not of interest. With this the simulation of a vibrating translation for three global axes can be reduced to one local axis with significant phase impact.

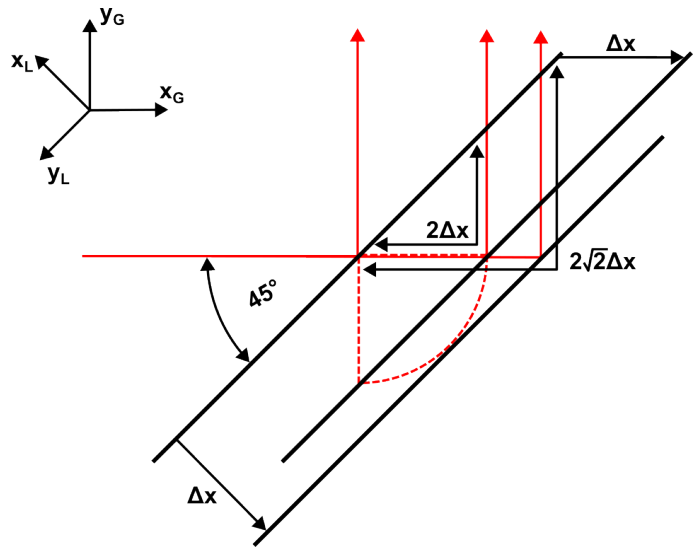

Figure 3.28: Moving the incident surface Δx in the global x-direction leads to a geometrical length increase of $2\Delta x$. Moving the same Δx in the local coordinates leads to an geometrical length increase of $2\sqrt{2}\Delta x$. Thus the OPL is increased more than in the first translation case.

For rotation the local y_L- and z_L-axis are used instead of the global coordinate axes. The reason for this is that rotating around the y_L- and z_L-axis introduces only one angular deflection, meaning the reflected beam path is either deflected upwards/downwards or to the left/right compared to the original reflected beam path. In case of rotating around a global coordinate axis in Fig. 3.27 a coupled angular deflection will occur. Rotating around the local coordinate axes therefore allows to separate these effects. In addition, rotation around the local x-axis does not alter the beam propagation path. For other components these principles in translation and rotation are analogous. Therefore, in both translation and rotation vibration simulations, the local coordinates of each component were used. This also reduces the computational cost by simulating one translation vibration and two rotation vibrations for each component instead of six DOFs. The exception is the RR, where a translation in the direction of the local x-axis, local y-axis and local z-axis leads to a different beam path. In case of x-translation the OPL is altered, in the other two cases a parallel offset of the returning probe beams is caused.

To select vibration frequencies f_x, f_θ the standard MIL-STD-810 method 514.8 was considered. The MIL-STD-810 standard gives guidelines to test and design materiel under consideration of environmental influences [34]. The method 514.8 covers vibrations. Because the interferometer is intended for applications in aviation, the following data was gathered from the standard. In annex C of method 514.8 the vibration exposure of aircraft are given by Fig. 3.29 and Fig. 3.30. In both cases the acceleration spectral density is plotted over a frequency spectrum.

Specific aircraft vibration spectra, such as the Lockheed C-5 Galaxy or the Boeing C-17

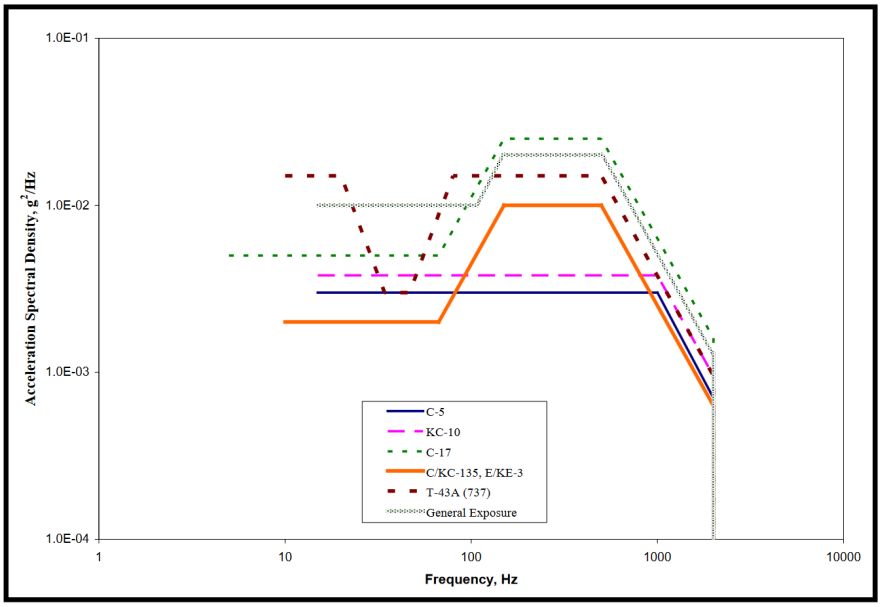

Figure 3.29: MIL-STD-810 specific aircraft vibration exposure [34].

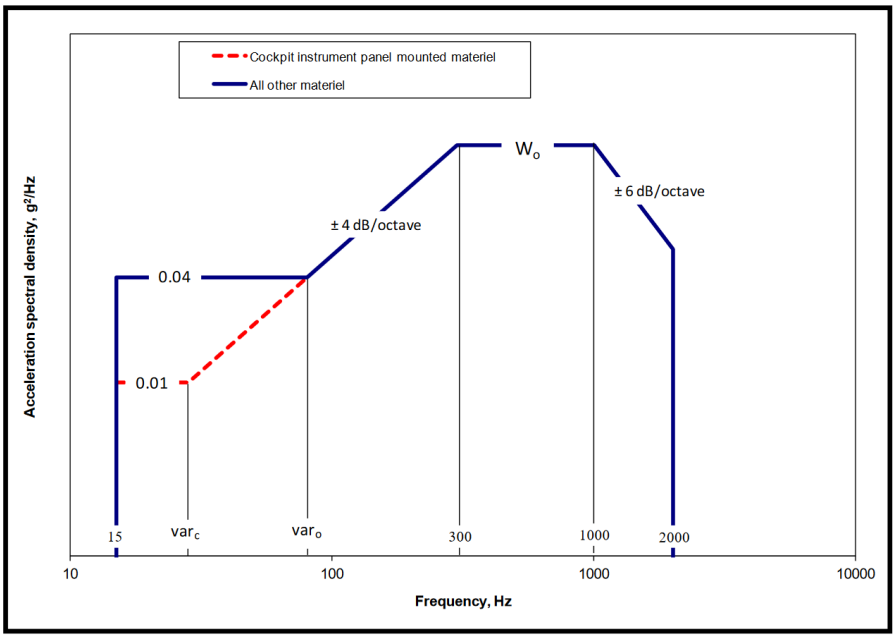

Figure 3.30: MIL-STD-810 general aircraft vibration exposure [34].

Globemaster III are given in Fig. 3.29. Fig. 3.30 shows a general acceleration spectral density. W_0 is a function of vibration exposure due to aerodynamically induced vibration and jet engine noise induced vibration and can be calculated with a formula also provided in annex C of method 514.8. In both figures it can be seen that a frequency spectrum is plotted on a logarithmic scale and that the vibration exposure magnitude ranges from 10 Hz to few kHz. A plateau and maximum of the acceleration spectral density is in the range from approximately 300 Hz to 1000 Hz. This range is of interest to simulate due to great accelerations, assuming resonance, meaning the excitation leads to a vibration of similar sized frequencies. A second assumption is that great accelerations lead to great displacements. The assumptions do not account for damping, inertia, the mass

nor eigenfrequencies of the optical components. Based on the assumptions a vibration frequency of $f_x = 1\,\text{kHz}$ and $f_\theta = 1\,\text{kHz}$ was chosen for simulations. Furthermore, a time span of 5 ms was used, meaning five oscillation periods were simulated. The vibration amplitudes in the simulations are $\hat{x} = 1.064\,\mu\text{m}$ for displacement and $\hat{\theta} = 0.01\,^\circ$ for rotation. The displacement of 1.064 µm equals the wavelength of ω. Thus in theory an OPL increase of 1.064 µm leads to a phase increment of 2π between reference and probe beams for ω. The rotation angle amplitude was chosen based on sensible deflections of the beams at the PD.

3.5 Simulation Methods

The digital twin interferometer was investigated with different simulation methods. In the next three chapters each method is briefly elaborated.

3.5.1 Single Shot Simulation

A static single shot simulation is a singular capture of the intensity distribution on the PD, similar to a photographic snapshot in time. Because there is no time-dependency in this simulation method, the AOM model does not introduce a frequency shift. Thus, the AOM model solely deflects the light beams for this simulation method. For simplicity, the power output of each diffracted beam by the AOM is the input power divided by the number of simulated orders. The working principle of the AOM in the digital twin is elaborated in detail in Ch. 3.2.3. This simulation method is useful to investigate the introduced interference pattern and to analyse how a singular displacement or rotation leads to a change in the intensity distribution. Furthermore, the distribution shape and position can be obtained with this method. In Fig. 3.31 the intensity distribution on the PD is shown for the adjusted interferometer. Reference and probe beams are coaxially aligned at the PD. Phase differences between probe and reference beams lead to partial constructive and destructive interference for each wavelength.

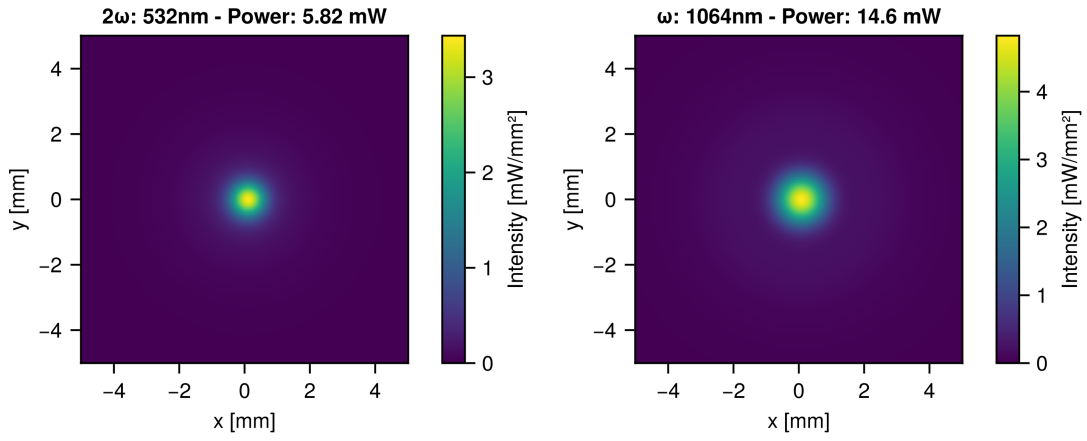

Figure 3.31: Static single shot intensity distribution of the adjusted interferometer

Small deviations can now be introduced by translating or rotating optical components. As an example M3 is rotated 0.1° counter-clockwise around the local z-axis. This causes fringes which are visible in Fig. 3.32. Both intensity distributions contain now vertical fringes and the spots moved to the right. The cause of this are spatial differences in the phase fronts between probe and reference beams. While the probe beams remain the

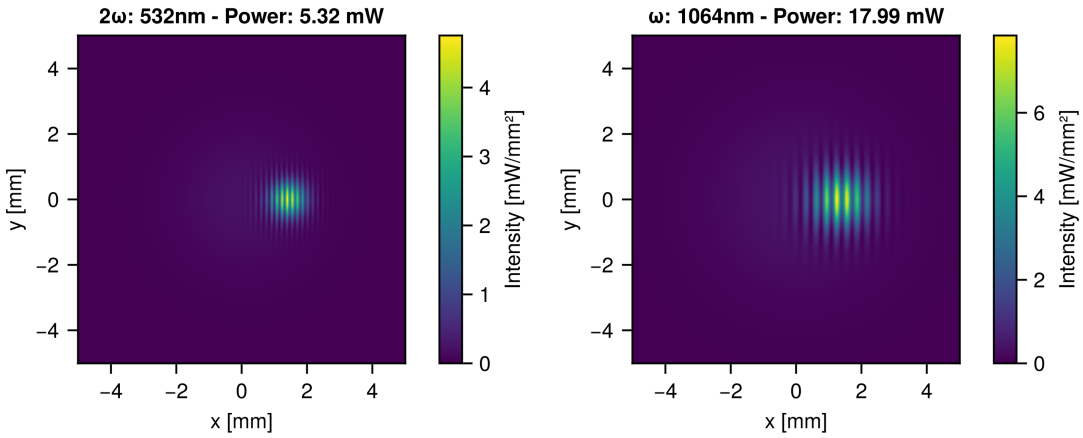

Figure 3.32: Fringes caused by local z-rotation of mirror M3

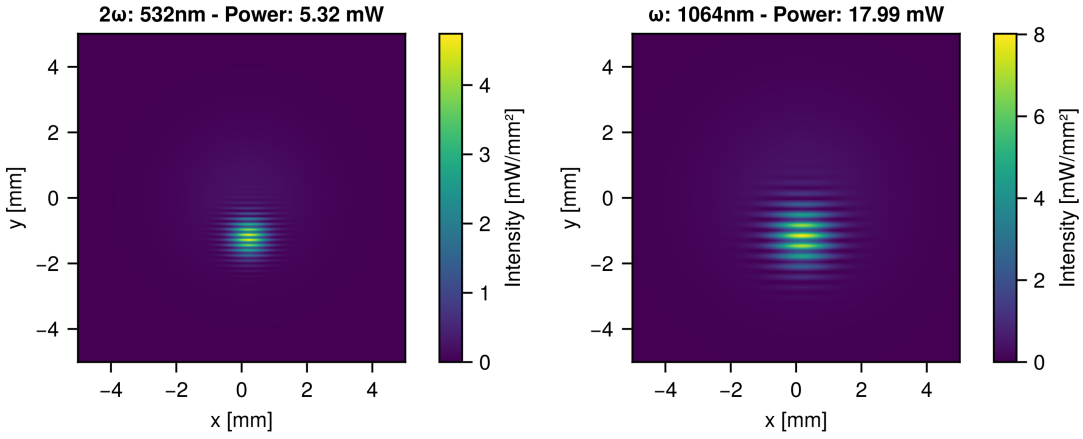

Figure 3.33: Fringes caused by local y-rotation of mirror M3

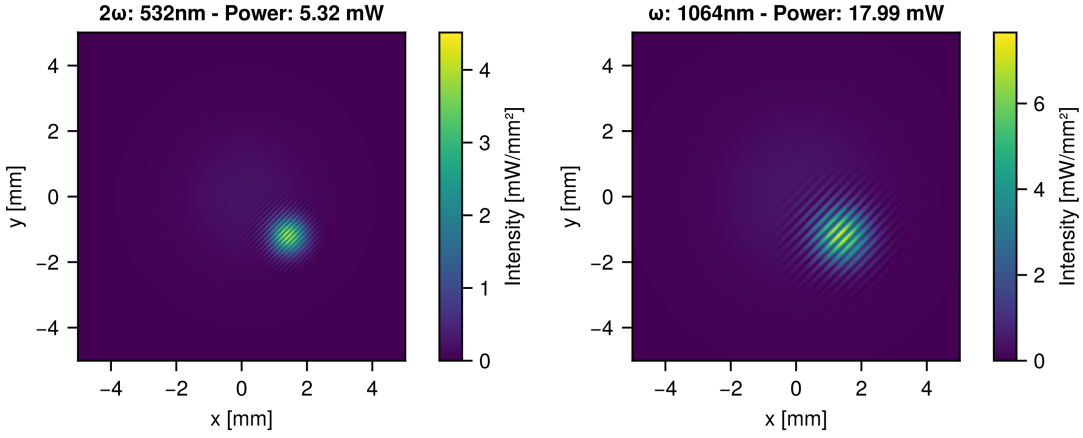

Figure 3.34: Fringes caused by local z- and y-rotation of mirror M3

same, the reference beams are deflected to the right, thus the intensity spots move to the right. Rotating around the local y-axis of M3 leads to the spots moving downwards, as shown in Fig. 3.33. The fringes are now orientated horizontally. Combining the rotation around the local z-axis with the rotation around the local y-axis leads to the intensity

distribution shown in Fig. 3.34. The spots moved both to the right and down. The fringes are orientated under a 45° angle.

3.5.2 Homodyne Vibration Simulation

Homodyne simulations were carried out by assuming that the AOM does not induce a frequency shift. The AOM model operates identical to the single shot technique. While this does not represent the actual working principle of the interferometer, it is useful to investigate how vibrations alter the power on the PD in general. More specifically, it allows to determine which vibration amplitude magnitudes $\hat{x}$ and $\hat{\theta}$ lead to significant effects in power on the PD and thus a phase shift φ of each wavelength. The vibration functions Δx and $\Delta\theta$ mentioned in Ch. 3.4 can be discretized with a grid where for each point in time t_i a certain amount of translation or rotation occurs

$$\Delta x_i = \hat{x} \cdot \sin(2\pi f_x \cdot t_i) \qquad \text{for } i = 0, 1, 2, ..., n\,, \tag{3.16}$$

and

$$\Delta\theta_i = \hat{\theta} \cdot \sin(2\pi f_\theta \cdot t_i) \qquad \text{for } i = 0, 1, 2, ..., n\,. \tag{3.17}$$

For every Δx_i and $\Delta\theta_i$ a single shot simulation is then carried out, the intensity distribution on the PD area is computed and the optical power P is evaluated by integrating the intensity distribution. Thus for every Δx_i or $\Delta\theta_i$ an optical power value for each wavelength is obtained. Because the sine in the discretized function is periodic it is sufficient to simulate one period. Furthermore, the computational cost can be reduced by using a linear displacement or rotation function, which contains the same information. It is then possible, if the displacement is discretized sufficiently, to obtain a curve for the optical power as a function of the displacement or rotation. Plotting the power P for each wavelength over the displacement or rotation angle yields the optical power curve for each optical component and the one-dimensional displacement or rotation. The respective resulting power curves for homodyne simulations are defined by Eq. (2.14), where the major variables are the phase φ and contrast c. As an example, the simulated power curve for the displacement of the RR is shown in Fig. 3.35.

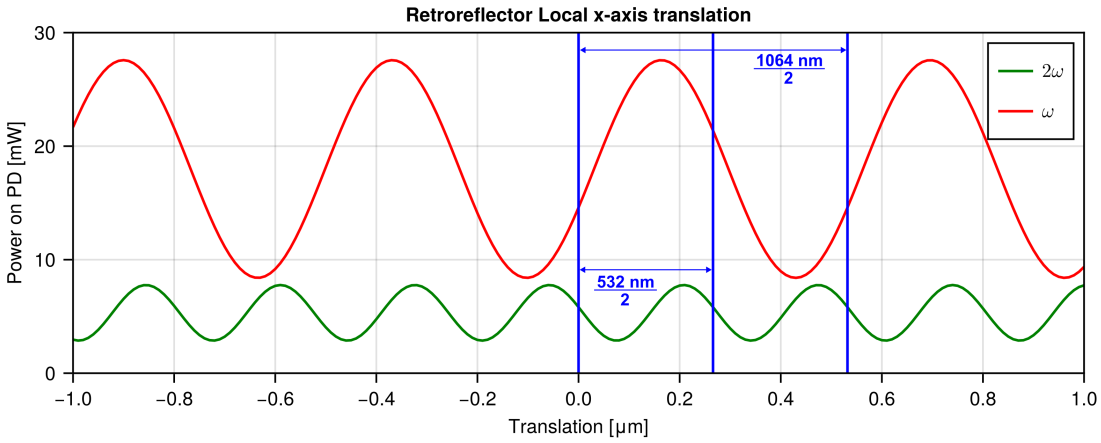

Figure 3.35: Homodyne translation simulation of the RR leads to a oscillating power curve. The contrast c is constant but reduced due to different phase fronts of reference and probe beams. The blue vertical lines indicate one period of power oscillation. For ω one period is 532 nm and for 2ω it is 266 nm. This equals the theory of the MI.

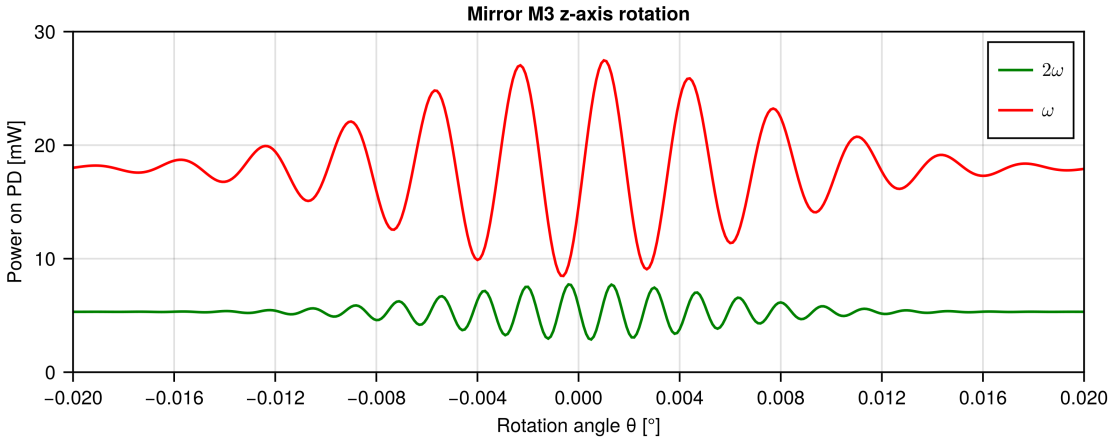

Figure 3.36: Homodyne rotation simulation of M3. The power oscillation amplitude is smaller for greater rotation angles due to reduced contrast c.

The vertical lines indicate that the oscillation period for ω is approximately 532 nm and for 2ω 266 nm. This coincides with the theory of the MI where translating an end mirror half the wavelength leads to one period in the interference pattern, equalling a phase shift of 2π. Due to reduced contrast c the amplitude in both curves is not maximal. A second example example is shown in Fig. 3.36 in which M3 is rotated around its z-axis. An oscillation in power occurs in both wavelengths starting from the adjusted alignment at $\theta = 0°$. For greater rotation angles the contrast c is lost and for $c = 0$ the power consists of a constant value. In both cases it is visible that the phase φ is continuously changed from the initial state. However, in general a reconstruction of φ for each wavelength solely by the homodyne power signal is non-trivial due to the ambiguity of the arccosine function. Thus in the next chapter the heterodyne vibration simulation method, which allows to determine the phase and its sign for each wavelength, is elaborated.

3.5.3 Heterodyne Vibration Simulation

In reality, the interferometer features a heterodyne detection technique due to the frequency shift caused by the AOM. The working principle of heterodyne detection is elaborated in Ch. 2.1.3. The frequency shift of the diffracted beam can be calculated with Eq. (2.32) and depends on the order m and the applied radio frequency Ω. In case of the investigated interferometer the diffracted beams are shifted $\Omega = 80\,\text{MHz}$ for ω and $2\Omega = 160\,\text{MHz}$ for 2ω. They are collinear and form the reference beam. In theory, the frequency shift leads to a power signal P for ω at the PD similar to Eq. 2.18

$$P_\omega(t) \propto 1 + c \cdot \cos(2\pi \cdot \Omega \cdot t + \varphi_\omega) \tag{3.18}$$

with interferometric contrast c and phase φ. For the power P of frequency 2ω

$$P_{2\omega}(t) \propto 1 + c \cdot \cos(2\pi \cdot 2\Omega \cdot t + \varphi_{2\omega})\,. \tag{3.19}$$

The power signal P oscillates therefore at the PD even when the interferometer is static, adjusted and no displacements are introduced. This is also called frequency-modulation of the power signal and leads to a beat signal at the PD. This is shown in Fig. 3.37, where Eq. (3.18) and Eq. (3.19) are plotted over time for $\varphi = 0$. For ideal contrast $c = 1$ the amplitude is at maximum, however the contrast c may be reduced due to a misalignment

between reference and probe beams. An alternative cause for reduced contrast are different spot sizes. The probe beams spot size is significantly greater than the reference beams due to the greater optical path length. In both cases this leads to the superposition and interference of different spatial phase fronts, reducing the contrast.

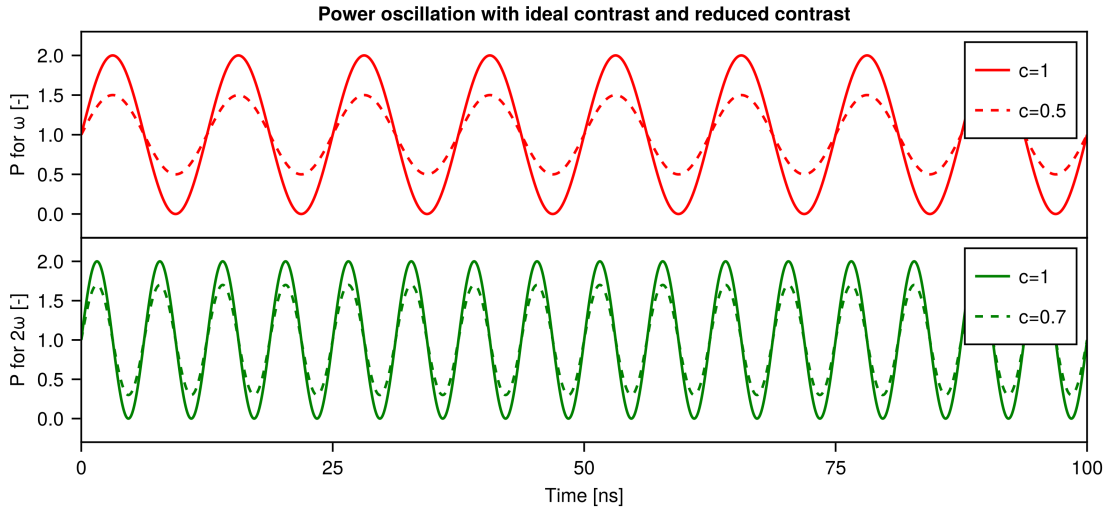

Figure 3.37: The power oscillates with frequency $\Omega = 80\,\mathrm{MHz}$ for ω and $2\Omega = 160\,\mathrm{MHz}$ for 2ω on the PD. The contrast $c = 1$ is ideal and may be reduced by misalignments.

The frequency modulation of the power signal P was implemented by phase modulating the diffracted beams. Each Gaussian beam contains the information of the electric field E, as described in Eq. 2.36, while propagating throughout the optical system. The function $E(r, z)$ returns a complex number $\hat{E}$ in general and can also be written in a reduced form with a scalar function $E_0(r, z)$ and an exponential term containing all phase information described in Ch. 2.3.1

$$E(r, z) = \hat{E} = E_0(r, z) \cdot e^{i \cdot \varphi_0(r,z)}\,, \tag{3.20}$$

where i is the imaginary unit. The term $E_0(r, z)$ can be interpreted as the scalar field strength and $\varphi_0(r, z)$ as the field phase of the electric field. By multiplying $\hat{E}$ with an additional complex exponential term, the phase of $\hat{E}$ can be adjusted trivially

$$\hat{E} \cdot e^{i \cdot \pi} = E_0(r, z) \cdot e^{i \cdot (\varphi_0(r,z) + \pi)}\,. \tag{3.21}$$

This allows the easy modelling of a phase modulation where phase increments can be added for each discretized simulation step in the time domain. This phase modulation leads to the desired effect of a frequency modulation. Hence, the modelling of the frequency modulation of the real-world AOM is as follows. Each time a beam intersects the AOM model, the diffraction orders are spawned as described in Ch. 3.2.3. The diffracted orders are then phase-shifted with a set phase increment as described above in order to generate an oscillating signal on the PD. By chaining a sequence of single-shot simulations, where for each simulation the phase is adjusted by a set increment, the time-domain behaviour of a heterodyne interferometer can be modelled. In particular to match the frequency modulation of $\Omega = 80\,\mathrm{MHz}$ and $2\Omega = 160\,\mathrm{MHz}$ the phase increment for each discretized time step must be chosen accordingly. For a set time-step t_i the additional phase term is

$$\varphi_{\mathrm{mod}}(t_i) = 2\pi \cdot \Omega \cdot t_i \tag{3.22}$$

a frequency-modulation of Ω takes place. Analogous for

$$\varphi_{\mathrm{mod}}(t_i) = 2\pi \cdot 2\Omega \cdot t_i \tag{3.23}$$

a frequency-modulation of 2Ω is realized.

Vibrations are simulated in the heterodyne simulation method equivalent to the homodyne method, where for each time step a certain displacement or rotation is imposed on an optical component, see Eq. (3.16) and Eq. (3.17). Thus, for each single shot simulation in the heterodyne method a displacement as well as a phase increment is set. The displacement or rotation may affect the phase φ in Eq. (3.18). This leads to a second frequency modulation of the power signal P where the carrier frequency is Ω and the varying phase $\varphi(t)$ leads to stretching or compressing of the fundamental oscillation. This is shown in Fig. 3.38, where for no introduced vibrations $\varphi = 0$ a dashed line and for a varying phase $\varphi(t)$, caused by vibrations, a drawn through line is depicted.

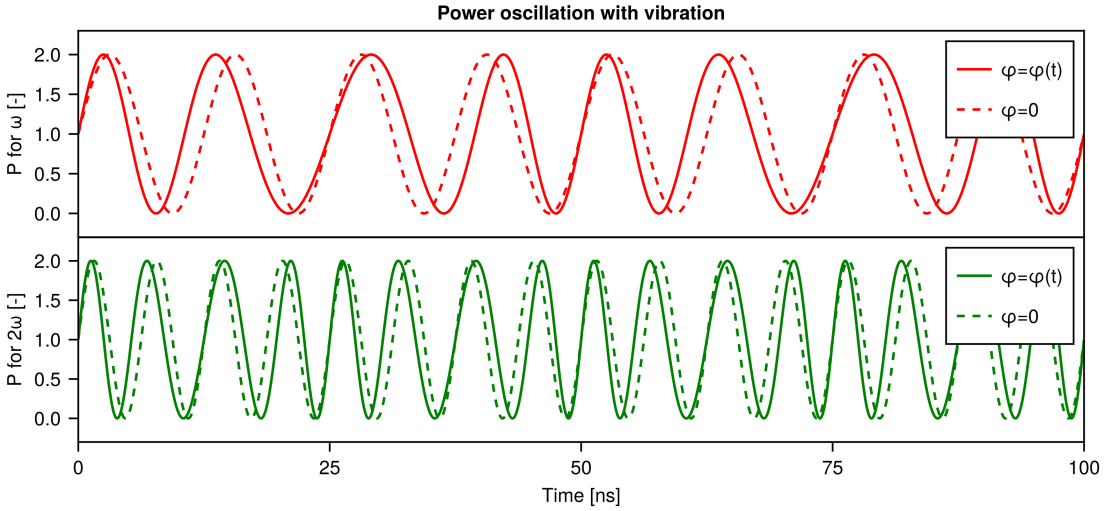

Figure 3.38: The vibration leads to a varying phase $\varphi(t)$. Thus the signal is modulated in frequency. The dashed line for each wavelength equals the power signal without a vibration. The drawn through lines are exemplary power signals caused by vibration.

It is of interest to obtain the phase φ for each wavelength. The phase difference $\Delta\varphi = \varphi_{2\omega} - 2\varphi_{\omega}$ can be obtained by the individual phases. This yields the left side of Eq. (2.8) and thus the measurement result of the SDI. For a mechanical insensitive interferometer any vibration does not effect the phase difference $\Delta\varphi$. If the probe medium is assumed as vacuum, meaning $n(\lambda) = 1$ for any wavelength and thus no dispersion, then with Eq. (2.8) it follows that $\Delta\varphi = 0\,\mathrm{rad}$. If a vibration leads to an error, then the phase difference will deviate from zero in that particular case. Thus for heterodyne simulations no dispersion in the probe medium was modelled. It was investigated how vibrations of each component alter the phases φ_{ω}, $\varphi_{2\omega}$ and how the phase difference $\Delta\varphi$ deviates from the ideal value of zero.

For every single shot simulation in the heterodyne vibration method a singular power value is obtained for each time-step. Storing each value leads to a power signal in time. To extract the phases of $\varphi_{2\omega}$ and φ_{ω} from the obtained power signal, the I/Q demodulation technique, elaborated in Ch. 2.1.3, is applied to the signal in a post-processing step. The obtained power P corresponds to the signal S in Ch. 2.1.3. A necessary part for I/Q demodulation is filtering the signal with a low-pass filter to cut-off and dampen frequencies

greater than the carrier frequency Ω. An ideal low-pass filter, assumed in the derivation of φ in Ch. 2.1.3, does not exist in practical applications. Thus various low-pass filters such as the continuous-time Butterworth filter with different steep frequency roll-offs were numerically tested on the signal. Good results were obtained with a discrete finite impulse response (FIR) low-pass filter featuring a Hanning window [35]. Because the FIR low-pass filter needs a rise-time to attenuate frequencies greater than the cut-off frequency, the first and last 0.5 ms of the resulting phases are not considered valid data. This reduces the total simulation time from 5 ms to 4 ms.

Simulating the frequency modulation in combination with mechanical vibrations leads to significant issues in regards to timescale resolution and simulation duration. The frequency modulation occurs at the MHz regime whereas mechanical vibrations occur on the order of several kHz. In combination, this difference in scale leads to an unfeasible amount of simulation steps in order to accurately capture the system dynamics in the time domain. Therefore, in the context of this work a simplification approach was chosen. The AOM model can independently simulate the frequency modulation and the diffraction angle, whereas they are directly related as per Eq. (2.31). This allows to artificially reduce the modulation frequency to a numerically feasible replacement frequency $\tilde{\Omega}$. However, analogous to the Nyquist-Shannon sampling theorem, $\tilde{\Omega}$ must still be large enough such that the mechanically caused phase shift is sufficiently sampled in the time domain, i.e. $\tilde{\Omega} \geq 2 \cdot f_x$. This ensures that the time-domain phase shift is correctly modulated onto the carrier frequency and in turn, can be demodulated using the I/Q scheme. Estimating the required sampling relation between $\tilde{\Omega}$ and f_x proved to be difficult, since especially for rotation the resulting gradient of the phase signal can become large very quickly. Hence, based on empiric observations it was determined that $\tilde{\Omega} = 500 \cdot f_x = 500\,\text{kHz}$ should be used as minimal digital modulation frequency. Nevertheless, this still represents a significant reduction in computational cost and allows to analyse the phase signal of the heterodyne SDI model in a representative manner.

4 Simulation results

In this chapter the results obtained with the heterodyne vibration simulation method, described in Ch. 3.5, are presented. In total there are nine optical components in this setup, which may be subject to vibrations and are of interest in the context of this work. The DPSSL and the PD are assumed as stationary components. Due to the vast amount of simulation results, selected results are presented in the following two chapters. The entirety of simulation results is condensed in Ch. 4.3.

4.1 Translation vibrations

For the investigation of vibrations a component of importance is the RR because it must be separated from the main optical group. Thus, in the real-world the vibration excitement for the RR can be fundamentally distinct. Furthermore, the large OPL of the outgoing and returning probe beams are relevant for the impact of vibrations on the measurement result. Applying a translation in the direction of the local x-axis x_L to the RR, equal to the global x-axis x_G, with the vibration function Δx of Ch. 3.4 is shown in Fig. 4.1.

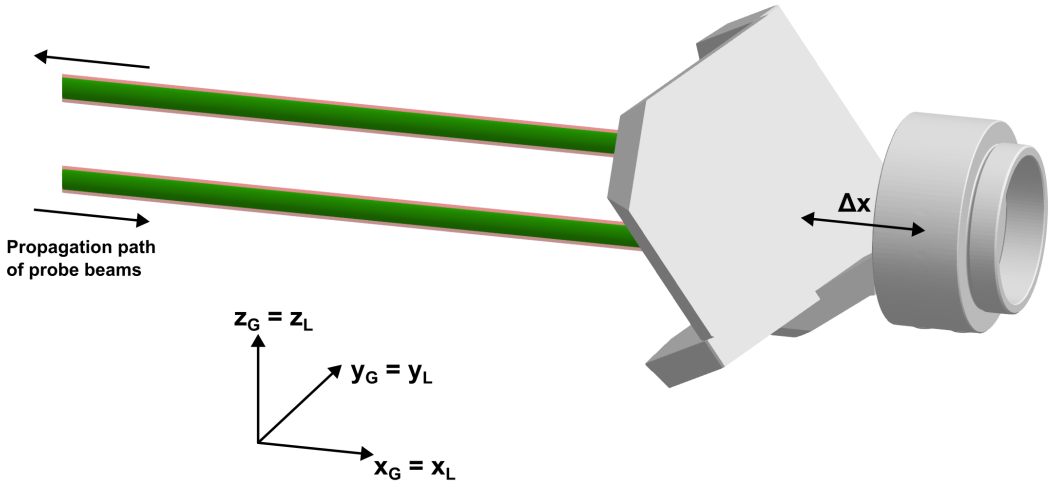

Figure 4.1: The RR is subject to translation vibrations. The propagation path of the probe beams is altered. A parallel offset between reference and probe beams is not introduced with this translation vibration.

The obtained power signal of the local x-axis translation, utilizing the heterodyne vibration simulation, is shown in Fig. 4.2. Due to the beat signal frequency of 500 kHz and the simulated timespan, the individual oscillations of the beat signal and the phase shift can not be discerned visually, compared to the illustrated example in Fig. 3.38. However, it is visible that the oscillation amplitude for each wavelength is constant, meaning the contrast is stable and reduced $c < 1$ for the local x-axis translation of the RR. The contrast can be calculated with $c = \frac{P_{\max} - P_{\min}}{P_{\max} + P_{\min}}$. With the described setup in Ch. 3.3 an

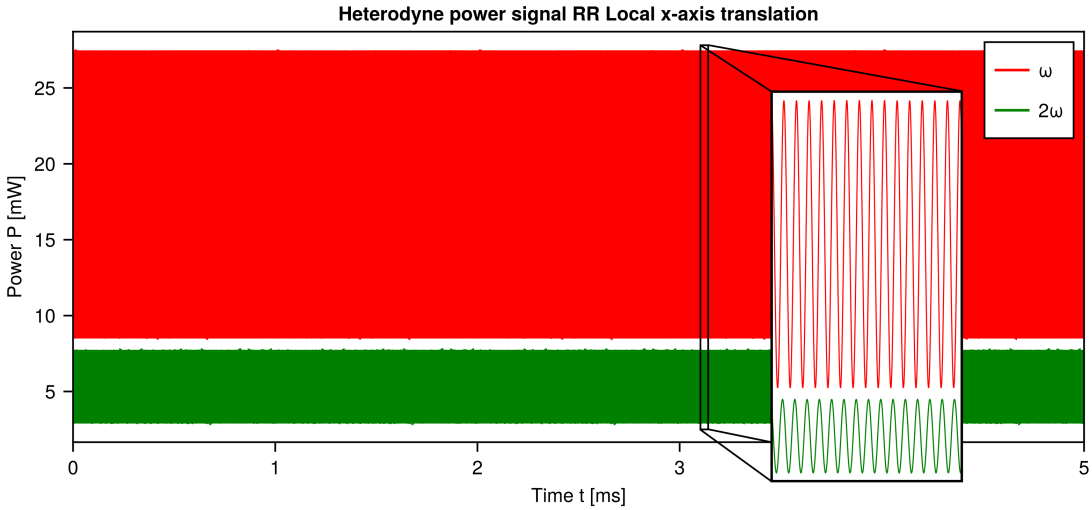

Figure 4.2: The heterodyne power signal obtained from local x-axis translation of the RR. The cut-out detail shows the oscillating beat signal.

interferometric contrast of $c_\omega = 0.46$ for ω and $c_{2\omega} = 0.53$ for 2ω is achieved. Applying the I/Q demodulation algorithm to the obtained power signal of Fig. 4.2 yields the phase of each wavelength φ_ω and $\varphi_{2\omega}$ plotted in the upper graph of Fig. 4.3. In the lower graph of Fig. 4.3 the translation vibration function Δx is shown as well as the phase difference $\Delta\varphi = \varphi_{2\omega} - 2\varphi_\omega$ on a common axis.

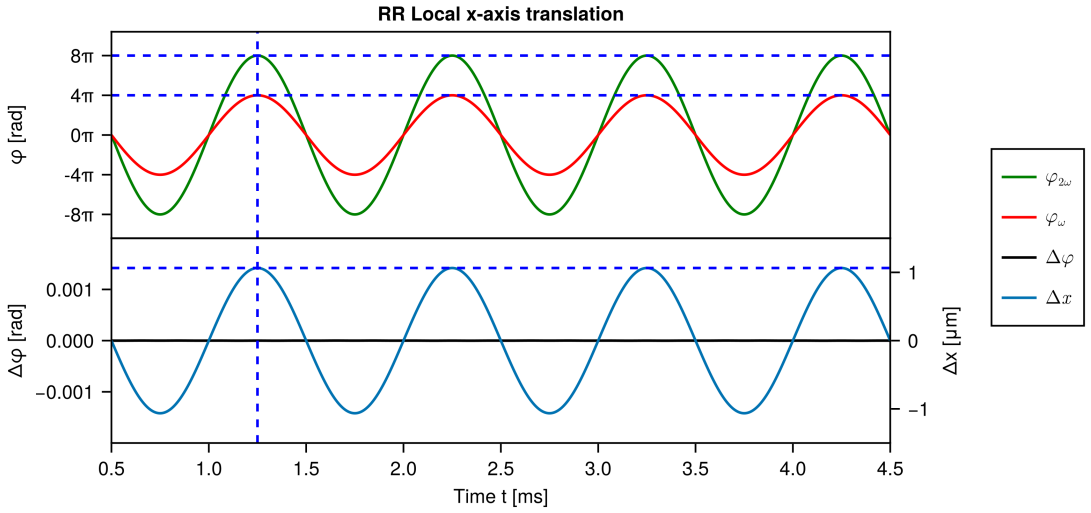

Figure 4.3: The phases correlate with the vibration translation function. The blue dashed horizontal lines indicate a phase shift of 4π and 8π respectively when the maximum displacement of 1064 nm, marked by the vertical blue dashed line, occurs. The phase difference $\Delta\varphi$ results in zero, which demonstrates the vibration robustness for one axis.

Firstly, it can be observed that the phase of each wavelength correlates with the vibration function. The period of the phase equals the period of vibration for both wavelengths. The peak in phase for each wavelength occurs for the maximum displacement of 1.064 µm,

marked as the horizontal blue dashed line in the lower graph. The maximum phase for $\omega \sim 1064\,\text{nm}$ is 4π and for $2\omega \sim 532\,\text{nm}$ it is 8π, shown with the horizontal blue dashed lines in the upper graph. This matches the theory of the MI, where a translation of an end mirror of half the wavelength $\lambda/2$ gives a phase shift of 2π. It is also visible that, while the phases of ω and 2ω are significant, the phase difference $\Delta\varphi$ is zero. This mean that the phases $\varphi_{2\omega}$ and φ_{ω} cancel each other out if the RR is moved in the direction of the global x-axis. Therefore no phase error is contributed by the x-axis translation vibration of the RR. This demonstrates the vibration robustness of the interferometer for this mode. For the y-axis translation of the RR a parallel offset is introduced between reference and probe beam. This case is adressed in Ch. 4.3.

Further, the components HBS1 and HBS2 as well as the mirrors M1 and M2 are of relevance for translation vibrations. They are of interest particular due to the characteristic of the interferometer. While each optical component after the AOM reflects or transmits both wavelengths in the same manner, the components prior to the AOM either separate the harmonically related wavelengths or reflect solely one wavelength. This component group is essential to assume a collinear beam pair in practice. Vice versa, it is obvious that it must be especially susceptible to dealignments in terms of phase sensitivity. In Fig. 4.4 it is shown how the translation vibration Δx was applied to the local x-axis of each component prior to the AOM in a singular heterodyne vibration simulation, thus four individual simulations were carried out.

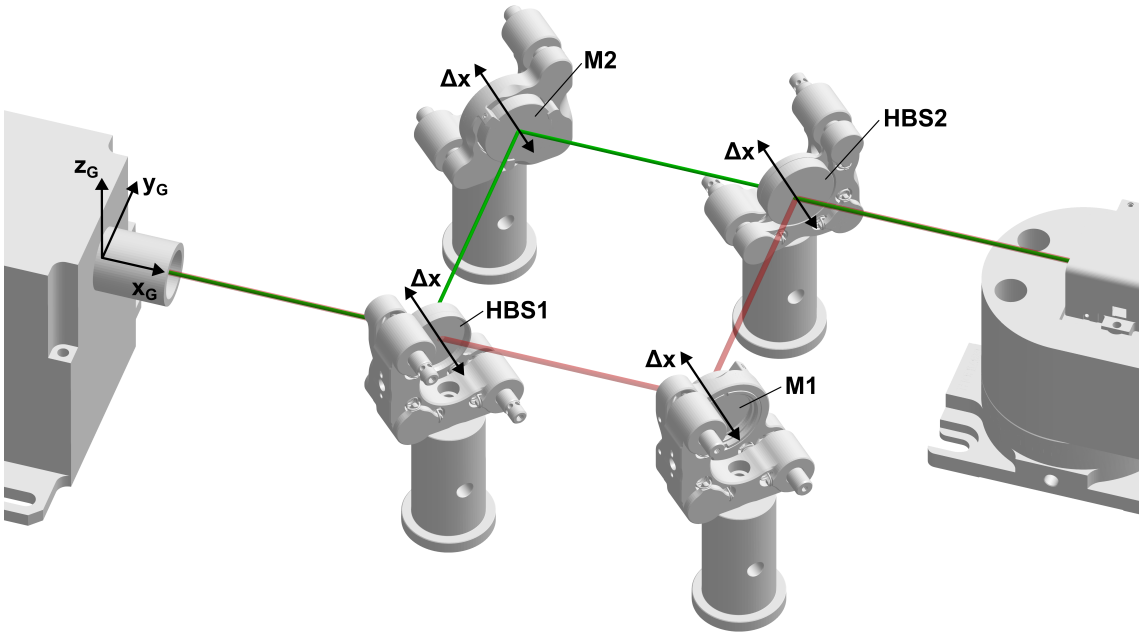

Figure 4.4: Local x-axis translation vibrations of optical components prior to the AOM.

The resulting phase graphs for HBS1 and HBS2 are shown in Fig. 4.5 and Fig. 4.6. It can be seen that the phase of the refracted wavelengths, in case of HBS1 it is ω, for HBS2 it is 2ω, are not affected by the vibration translation. The same applies for M1, where the path of 2ω is not altered in the vibration simulation and for M2, where the path of ω is not altered. Thus the phase of one wavelength is constant, while the phase of the other wavelength correlates with the vibration function. This results in a phase difference, where $\varphi_{2\omega}$ and φ_{ω} do not cancel each other out and thus a phase error results in the measurement. For each of the four translation cases prior to the AOM the phase error is $\Delta\varphi > 0.2\,\text{rad}$, visible in the lower graphs of Fig. 4.5 and Fig. 4.6. For M3, M4 and the PBS the local

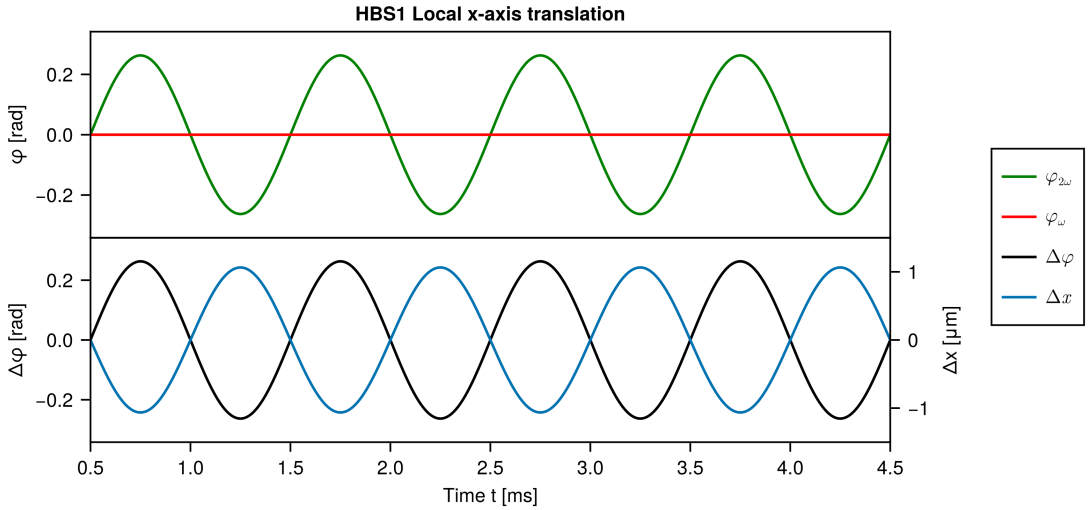

Figure 4.5: Resulting phases and phase difference $\Delta\varphi$ due to a local x-axis translation of HBS1. The phase φ_{ω} is not altered by translation vibration.

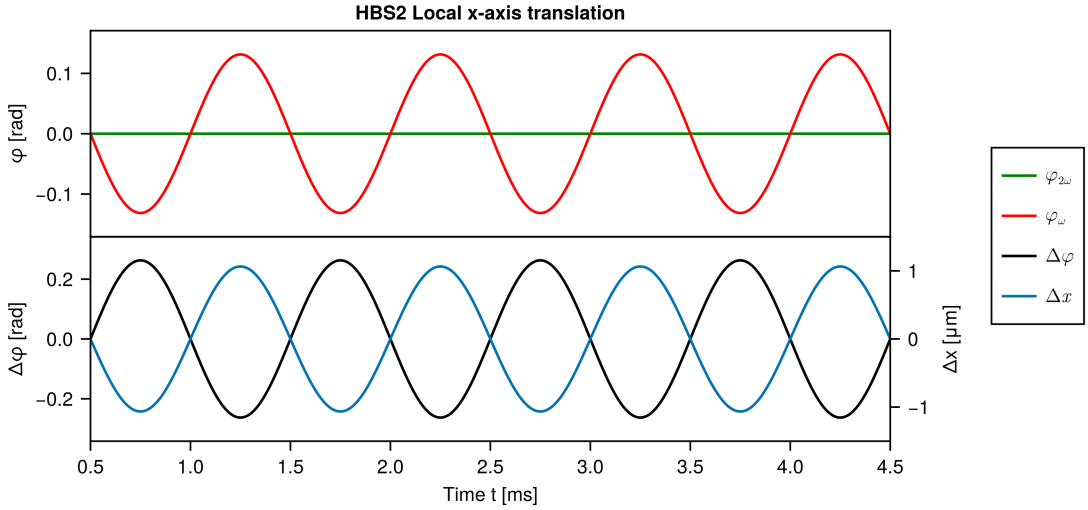

Figure 4.6: Resulting phases and phase difference $\Delta\varphi$ due to a local x-axis translation of HBS2. The phase $\varphi_{2\omega}$ is not altered by translation vibration.

x-axis translation vibration simulations were carried out analogous.

4.2 Rotation vibrations

While translation vibrations mostly cause a change in OPL and a parallel offset between reference and probe beams, rotation vibrations are inherently different. The normal vector of the incident surface is continuously changed and thus at the PD a spatial angular difference between reference and probe beams occurs. Because reference and probe beams intersect under an angle on the PD, the superposition and thus the interference is different in scale even for small displacements compared to the translation vibrations. An exception is the RR, where even for rotations, the direction of the outgoing probe beams equals

the direction of the incoming probe beams, however with a parallel offset. In Fig. 4.7 the rotation around the local vertical z-axes and local horizontal y-axes is shown for the components M3, M4 and the PBS. Furthermore, it can be seen that the reference and probe beams spot diameters are different in size when recombined by the PBS. The probe beams spots are increased due to the OPL to the RR and back.

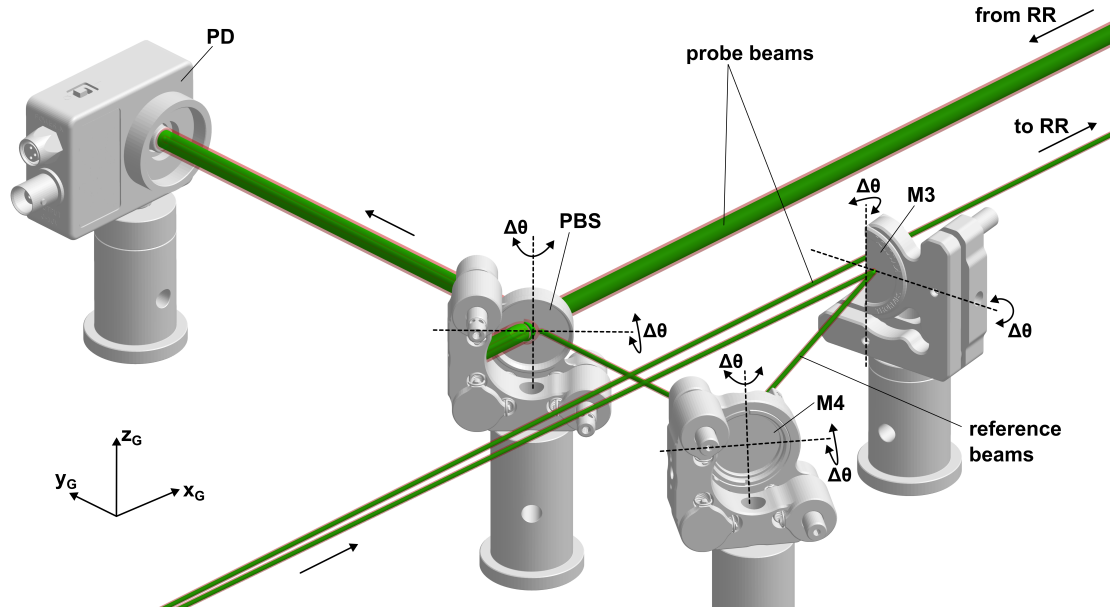

Figure 4.7: Local y- and z-axis vibrations of optical components after the AOM.

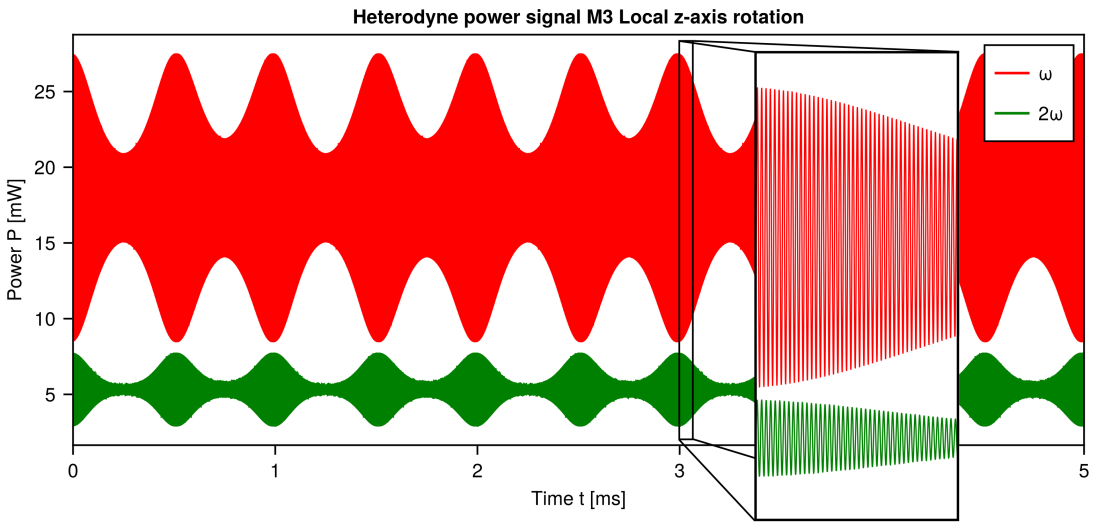

Figure 4.8: The heterodyne power signal obtained from local z-axis rotation of M3. The cut-out detail shows the oscillating beat signal, where the contrast is not constant but varies depending on the rotation angle.

The heterodyne power signal of a vibration rotation, analogous to Fig. 4.2 for translation, is plotted for the local z-axis rotation of M3 in Fig. 4.8. It can be seen, compared to Fig. 4.2, that the contrast is in this case not constant for the rotation vibration. The power is modulated in amplitude by the vibration due to a loss of contrast. Maximum

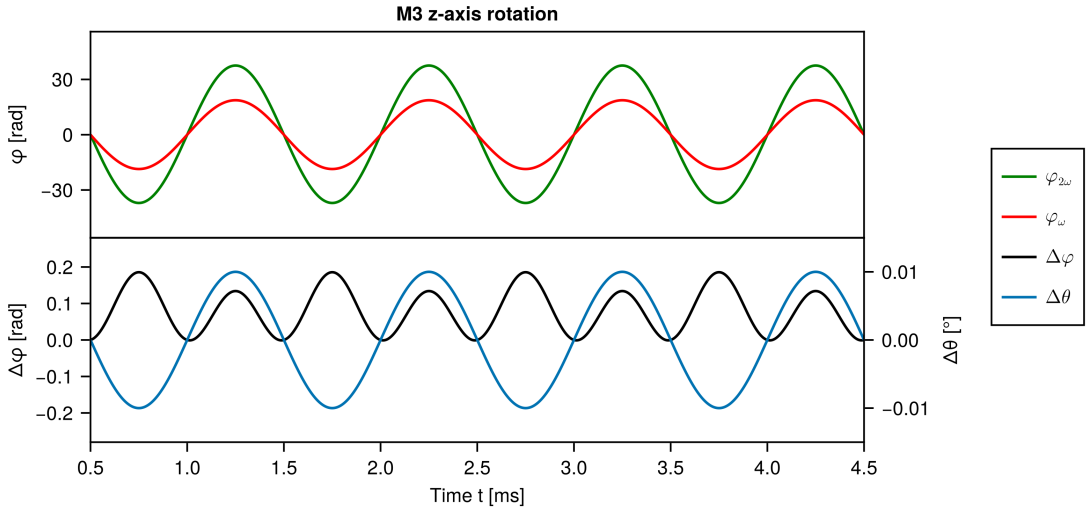

Figure 4.9: Resulting phases and phase difference $\Delta\varphi$ due to a local z-axis rotation of M3.

contrast appears where the phase fronts intersect without any angular difference, whereby the lowest contrast is obtained for the greatest applied rotation angle. It is also visible that the contrast is not reduced equally for the maximum rotation. This unsymmetrical behaviour is caused by the refraction of the PBS, where refraction depends on the AOI. Thus different angular deviations between reference and probe beam occur for the same absolute rotation angle $|\Delta\theta|$ in case of a local z-axis translation of M3. In case the contrast is completely lost ($c \approx 0$), a constant signal is obtained and the I/Q demodulation fails without exception, meaning that, no measurement result can be obtained. The power signal of Fig. 4.8 is I/Q demodulated after simulation, identical to the procedure of the translation vibration method. The resulting phases $\varphi_{2\omega}$ and φ_{ω} are shown in the upper graph of Fig. 4.9. The phases $\varphi_{2\omega}$ and φ_{ω} correlate with the rotation $\Delta\theta$ plotted in the lower graph of Fig. 4.9. The peak in phase for each wavelength is reached for the maximum rotation angle $|\Delta\theta| = 0.01°$. The phase of φ_{ω} is then $> 15\,\text{rad}$ and for $\varphi_{2\omega}$ even $> 30\,\text{rad}$. The phase difference $\Delta\varphi = \varphi_{2\omega} - 2\varphi_{\omega}$ is plotted in the lower graph of Fig. 4.9. The magnitude of phase difference is vastly lower at approximately 0.2 rad than the magnitude of the individual phases. However, the phases $\varphi_{2\omega}$ and $2\varphi_{\omega}$ do not cancel each other out fully, so that a residuum in phase difference exists. For an assumed vibration insensitive interferometer $\Delta\varphi = 0$ this residuum causes a significant measurement error. The phase error correlates with the rotation. Maximum absolute phase error $|\Delta\varphi|$ occurs for maximum absolute rotation angle $|\Delta\theta|$. Furthermore, it is visible that the maximum phase error $\Delta\varphi$ depends on the presence of a negative or positive rotation angle $\Delta\theta$. This unsymmetrical behaviour is also featured in the next chapter. Analogous to the results of the M3 z-axis rotation, rotations around the local y- and z-axis for the components prior and after the AOM were conducted. The condensed results of these simulations are presented in the following chapter.

4.3 Component Sensitivity Analysis

The component sensitivity analysis was carried out to compare the phase error $\Delta\varphi$ caused by the vibration of individual components. In case of a vacuum probe medium, vibration simulations should yield a nominal phase difference of $\Delta\varphi = \varphi_{2\omega} - 2\varphi_{\omega} = 0\,\text{rad}$. To

distinguish between a phase error caused by vibration and numerical precision errors, a minimal threshold of 1×10^{-5} rad for the largest calculated phase error $|\Delta\varphi|$ was applied to each case in order to be considered in the following evaluation. The component sensitivity analysis does not compare the loss of contrast for each component individually, but requires that contrast is sufficient. Because the low-pass filter in the I/Q demodulation is not ideal, a moving average filter was used to smooth the phase error in the following figures.

The comparison of phase errors caused by translation vibrations is shown in Fig. 4.10 and in Fig. 4.11. Two figures are used due to the fact that the phase error magnitude differs depending on the component. In both figures the absolute value of the phase error $|\Delta\varphi|$ is plotted over the absolute displacement $|\Delta x|$. In Fig. 4.10 it can be seen that four components, that is HBS1, HBS2, M1 and M2, contribute phase error terms $|\Delta\varphi| > 0.2$ rad. For these components each phase error is equal for a given displacement. A displacement of $|\Delta x| = 1.064\,\mu$m yields a phase error $|\Delta\varphi| = 0.26$ rad. The obtained curves for those components appear linear. The phase error gradient is approximately $\frac{|\Delta\varphi|}{|\Delta x|} = 0.25\,\text{rad}/\mu\text{m}$.

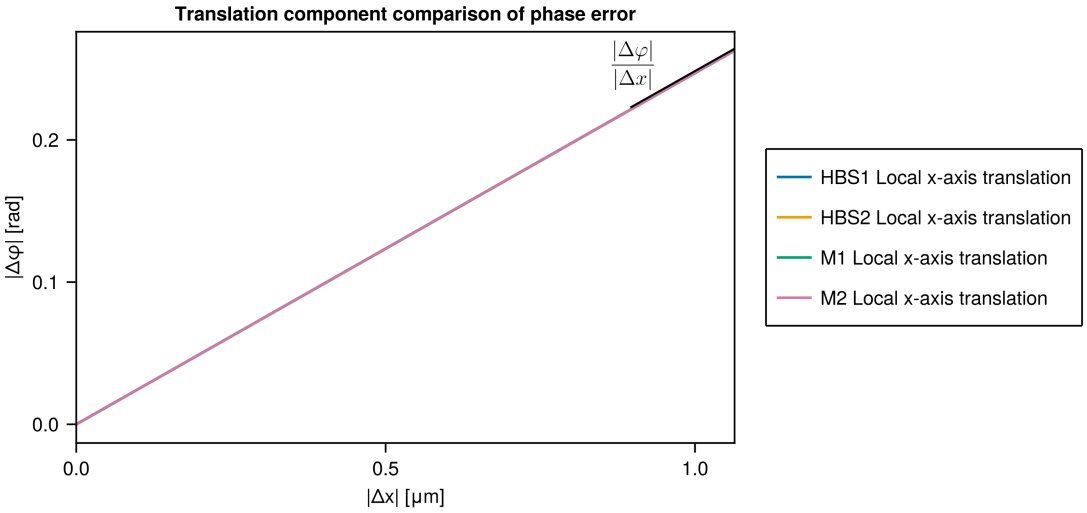

Figure 4.10: Translation phase error comparison. Range $|\Delta\varphi| > 0.1$ rad.

In Fig. 4.11 the phase error for translation vibrations is shown where the maximum absolute phase error is between the threshold of 1×10^{-5} rad and 10×10^{-5} rad. It is visible that the phase error due to RR y-axis translation appears linear, while the phase error curves due to x-axis translation of the PBS and M4 are slightly non-linear. For the translation of M3 a significant non-linearity can be observed. The maximum displacement of $|\Delta x| = 1.064\,\mu$m yields an absolute phase error of $|\Delta\varphi| = 8.1 \times 10^{-5}$ rad for the RR, followed by the PBS with 5.8×10^{-5} rad and the M4 with 4.6×10^{-5} rad. The lowest phase error due to translation vibration measured in the simulation occurs for M3 with $|\Delta\varphi| = 1.6 \times 10^{-5}$ rad. For the sensitivity analysis a sensitivity $\frac{|\Delta\varphi|}{|\Delta x|}$ or $\frac{|\Delta\varphi|}{|\Delta\theta|}$ was determined based on the maximum gradient along the simulated curves, as shown in Fig. 4.11. The phase error gradient for the RR y-axis translation is $\frac{|\Delta\varphi|}{|\Delta x|} = 0.08\,\text{mrad}/\mu\text{m}$ and for the M3 x-axis translation $0.02\,\text{rad}/\mu\text{m}$. The phase error gradients due to translation vibration are listed in Tab. 4.1 for the other components.

For the rotation vibrations the phase error comparison of components are depicted in Fig. 4.12, Fig. 4.13 and 4.14, each covering a certain range of maximum absolute phase error $|\Delta\varphi|$. Analogous to translation vibrations, the absolute phase error $|\Delta\varphi|$ is plotted for each figure over the absolute rotation angle $|\Delta\theta|$.

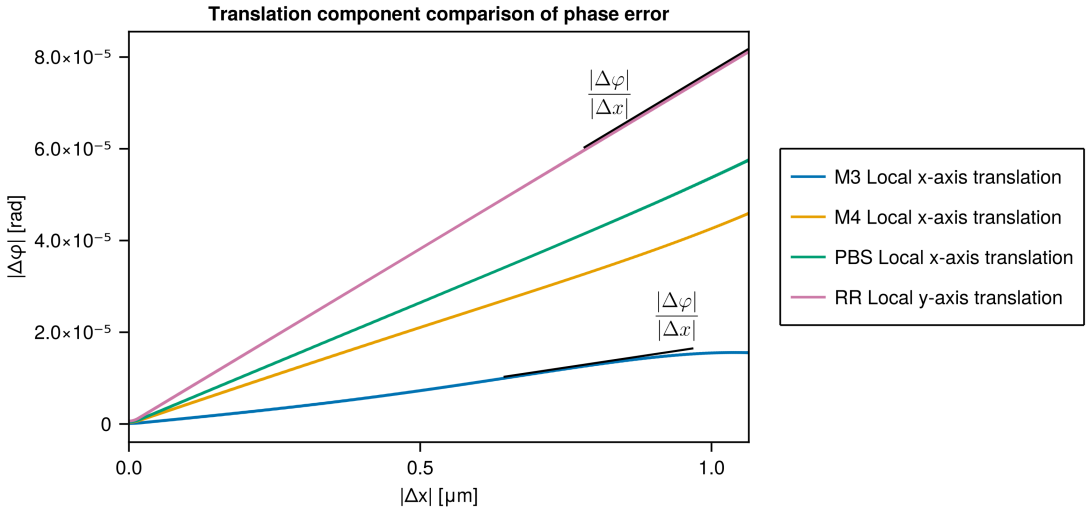

Figure 4.11: Translation phase error comparison. The maximum gradient of each curve $\frac{|\Delta\varphi|}{|\Delta x|}$ represents the sensitivity to vibrations. Range $|\Delta\varphi|$ from 1×10^{-5} rad to 10×10^{-5} rad.

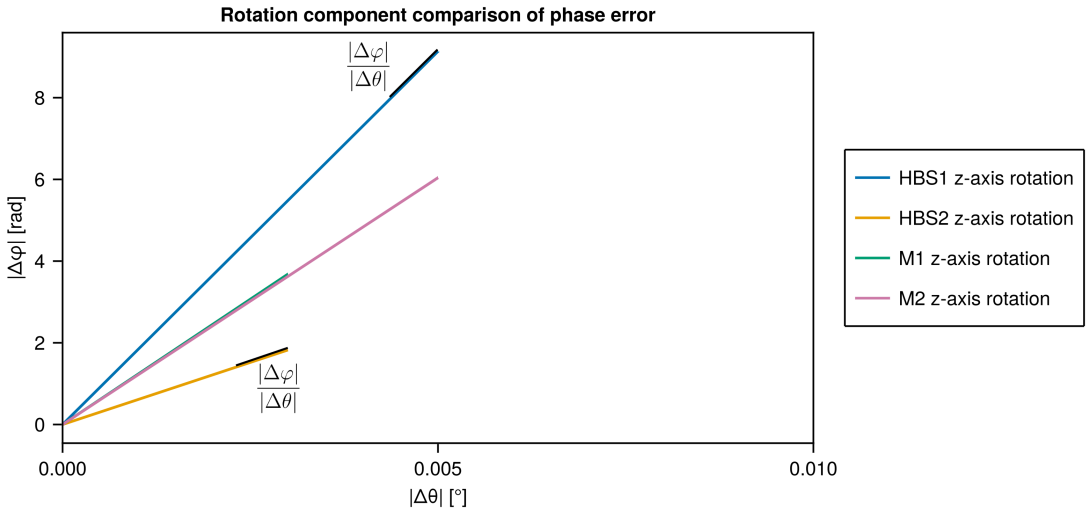

Figure 4.12: Rotation phase error comparison. Range $|\Delta\varphi| > 1$ rad.

In Fig. 4.12 components with the greatest phase error contributions are shown. The rotation vibration amplitude is $\hat{\theta} = 0.01°$. However, for M1 and HBS2 sufficient contrast was merely achieved for $\hat{\theta} = 0.003°$. For M2 and HBS1 a maximum amplitude of $\hat{\theta} = 0.005°$ was possible before total loss of contrast. One can see that in Fig. 4.12 the phase error for each component is significant, i.e. $\Delta\varphi > 1$ rad, and that each obtained curve appears linear. The greatest phase error gradient is caused by the z-axis rotation of HBS1. The gradient is approximately $\frac{|\Delta\varphi|}{|\Delta\theta|} = 1800\,\text{rad}/°$. The gradients of M1 and M2 are similar and amount to $1200\,\text{rad}/°$. For HBS2 a gradient of $600\,\text{rad}/°$ can be observed. Because of linear curves the resulting phase error can be computed for these components with the gradient for $|\Delta\theta| < 0.003°$, respectively $|\Delta\theta| < 0.005°$.

The next major phase error scope for rotation ranges from a maximum $|\Delta\varphi|$ of 0.05 rad to 0.25 rad, shown in Fig. 4.13. It is striking that while for the components prior to

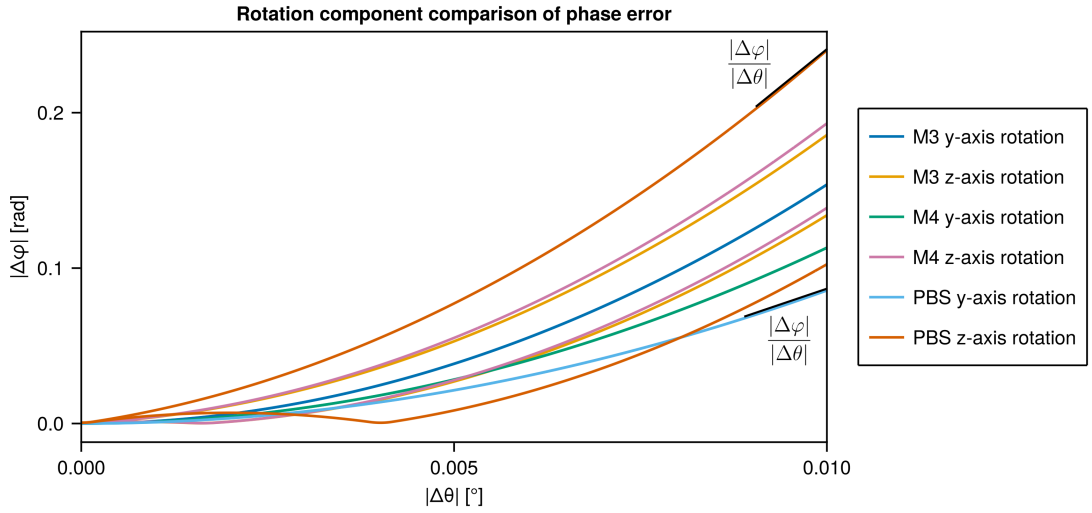

Figure 4.13: Rotation phase error comparison. The maximum gradient of each curve $\frac{|\Delta\varphi|}{|\Delta\theta|}$ represents the sensitivity to vibrations. Range $|\Delta\varphi|$ from 0.05 rad to 0.25 rad.

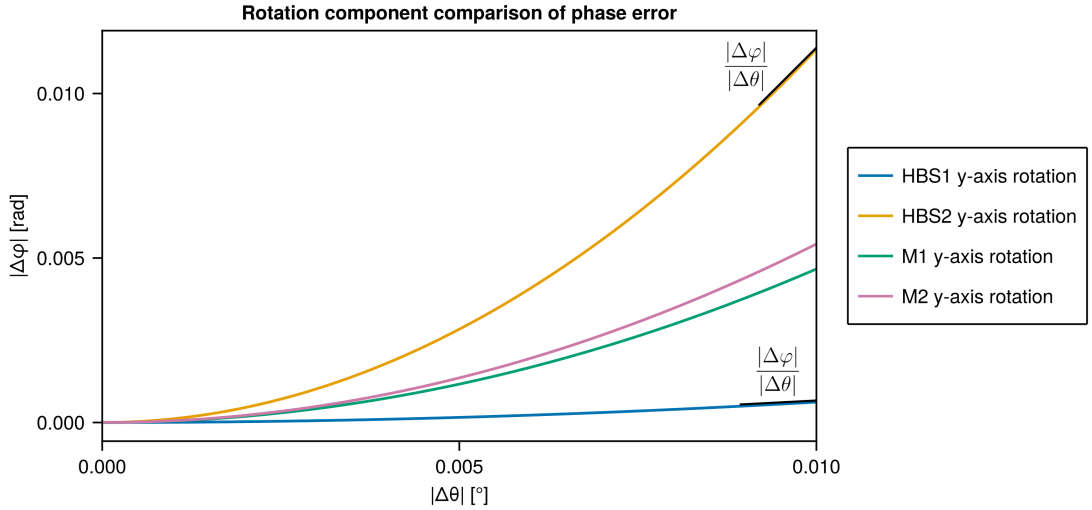

Figure 4.14: Rotation phase error comparison. The maximum gradient of each curve $\frac{|\Delta\varphi|}{|\Delta\theta|}$ represents the sensitivity to vibrations. Range $|\Delta\varphi| < 0.05$ rad.

the AOM in Fig. 4.12 a linear phase error is obtained, the phase error of components behind the AOM are strongly non-linear. Furthermore, it can be observed that for z-axis rotation cases two curves are plotted. This is caused by an unsymmetrical behaviour, where interference and thus the phase error depends on the sign of the rotation angle. Meaning, for a set positive rotation angle a different phase error is obtained as for the equal sized negative rotation angle. In case of symmetric phase error behaviour the curves are identical for negative and positive rotation. Thus the y-axis rotation cases in Fig. 4.13 lead to symmetric phase error behaviour, while the z-axis rotation cases cause an unsymmetrical phase error behaviour. Furthermore, for all components a general trend is apparent. For maximum rotation $|\Delta\theta| = 0.01°$ the z-axis rotation of a component leads to a greater phase error $|\Delta\varphi|$ than the corresponding y-axis case of the same component. Quantitatively, the

lowest phase error in this range is caused by the PBS y-axis rotation with $|\Delta\varphi| = 0.09\,\text{rad}$, while the PBS z-axis rotation causes the greatest phase error of 0.24 rad in this range. However, the phase error for any component in Fig. 4.13 is significantly smaller than the z-axes rotation cases of the components prior to the AOM, shown in Fig. 4.12. Due to the non-linearity of phase error in Fig. 4.13 the phase error gradients $\frac{|\Delta\varphi|}{|\Delta\theta|}$ correlate with the absolute phase error. For the PBS z-axis rotation the phase error gradient is $\frac{|\Delta\varphi|}{|\Delta\theta|} = 40\,\text{rad}/^\circ$. For the PBS y-axis a gradient of $17\,\text{rad}/^\circ$ is obtained. The gradients of M3 and M4 are enclosed by these values and are provided in Tab. 4.1.

In Fig. 4.13 the rotation phase error curves causing an error $|\Delta\varphi| < 0.05\,\text{rad}$ are depicted. It is visible that the curves are again non-linear and symmetric. In this range components prior to the AOM are causing a phase error. The y-axis rotation of M1 and M2 cause a phase error of similar magnitude $|\Delta\varphi| \approx 0.005\,\text{rad}$ for a rotation angle of 0.01°. The HBS2 y-axis rotation generates the greatest error in this range with 0.011 rad, while the HBS1 y-axis rotation effects the phase fewest with $6 \times 10^{-4}\,\text{rad}$. Comparing Fig. 4.12 and Fig. 4.14 shows that the z-axes rotation cases of components prior to the AOM cause notable phase errors while phase error due to y-axes rotation of the same components are noticeably smaller. The phase error gradients again correlate with the absolute phase error in Fig. 4.14 and are listed in Tab. 4.1. An overview of the absolute phase errors is given in Tab. 4.2. The computation time of simulations, conducted with the heterodyne vibration simulation method, was reduced by parallelizing the simulations of components. A singular ray trace of ω and 2ω through the optical system takes approximately 0.2 s on a modern CPU. The time scale of 5 ms was discretized with 100 000 time steps. Thus the computation time of one axis for one component is around 5.5 h. Sequential execution of simulations with 9 components and 3 axes takes therefore multiple days. By parallelizing the computation with a 2x Xeon Gold 6320 dual processor featuring 80 threads the computation time was reduced to 6 h to obtain translation results and approximately 12 h for rotation cases.

Table 4.1: Maximum phase error gradients $\frac{|\Delta\varphi|}{|\Delta x|}$ and $\frac{|\Delta\varphi|}{|\Delta\theta|}$ for components

Components	x-axis translation	y-axis rotation	z-axis rotation
HBS1	$250\,\frac{\text{mrad}}{\mu\text{m}}$	$0.12\,\frac{\text{rad}}{^\circ}$	$1800\,\frac{\text{rad}}{^\circ}$
HBS2	$250\,\frac{\text{mrad}}{\mu\text{m}}$	$2.2\,\frac{\text{rad}}{^\circ}$	$600\,\frac{\text{rad}}{^\circ}$
M1	$250\,\frac{\text{mrad}}{\mu\text{m}}$	$1\,\frac{\text{rad}}{^\circ}$	$1200\,\frac{\text{rad}}{^\circ}$
M2	$250\,\frac{\text{mrad}}{\mu\text{m}}$	$1\,\frac{\text{rad}}{^\circ}$	$1200\,\frac{\text{rad}}{^\circ}$
M3	$0.02\,\frac{\text{mrad}}{\mu\text{m}}$	$30\,\frac{\text{rad}}{^\circ}$	$34\,\frac{\text{rad}}{^\circ}$
M4	$0.05\,\frac{\text{mrad}}{\mu\text{m}}$	$22\,\frac{\text{rad}}{^\circ}$	$35\,\frac{\text{rad}}{^\circ}$
PBS	$0.06\,\frac{\text{mrad}}{\mu\text{m}}$	$17\,\frac{\text{rad}}{^\circ}$	$40\,\frac{\text{rad}}{^\circ}$

Table 4.2: Maximum phase error $|\Delta\varphi|$ for components

Components	x-axis translation	y-axis rotation	z-axis rotation
HBS1	260 mrad	0.6 mrad	9.1 rad
HBS2	260 mrad	11 mrad	1.8 rad
M1	260 mrad	5 mrad	3.7 rad
M2	260 mrad	5 mrad	6.0 rad
M3	0.016 mrad	150 mrad	190 mrad
M4	0.046 mrad	110 mrad	190 mrad
PBS	0.058 mrad	86 mrad	240 mrad

5 Discussion

In the following section the results obtained with the digital twin of the SDI will be analysed and interpreted. In essence, the simulation results can be sorted into three groups with respect to the optical components: the beam co-alignment optics before the AOM, the reference and probe beam alignment optics after the AOM and the RR itself. The main common denominator for this choice is the order of magnitude of the obtained phase error for a fixed vibration amplitude and component. For each group we can then further consider the induced interferometric phase error with respect to translational and rotational vibrations.

The greatest phase errors, ranging from 1.8 rad to 9.1 rad, with phase error gradients from 600 rad/° to 1800 rad/°, are caused by the z-axis rotation of components prior to the AOM, i.e. HBS1, HBS2, M1 and M2 as shown in Fig. 4.4. Total loss of contrast occurred for these components at rotation angles of $|\Delta\theta| > 0.003°$ and $|\Delta\theta| > 0.005°$ respectively. The phase error gradients due to the z-axis rotation of components prior to the AOM are significantly greater than any phase error gradient due to translation. The same applies for the absolute phase errors. This is an expected results, since the main purpose of this component group is to realign the visible and infrared beam to ensure the main premise of two-color interferometry. Any dealignment suffered by this group will directly lead to a non-common phase error which increases with the overall probe beam length, especially in the case of rotational dealignment. In this case, the displacement scales with the overall propagation path length. As anticipated, mechanical stability of this group is paramount.

The probe and reference beam alignment optics, as shown in Fig. 4.7 and consisting of M3, M4 and the PBS, cause significantly less phase error, that is from 0.1 rad to 0.2 rad for rotation of components after the AOM. Here, strongly non-linear and unsymmetrical phase errors can be observed with phase error gradients ranging from 17 rad/° to 40 rad/°. It is important to note that the results for these components were obtained with an almost perfectly adjusted co-alignment group. Whereas theory suggests that the vibration compensation method should virtually eliminate these errors, they are still present and significant in this simulation. For reference, as per the Ciddor equation these phase changes will be interpreted as an erroneous change in pressure with approximately 0.5 mrad m^{-1} Pa^{-1}, i.e. 1 Pa pressure error per mrad for a hypothetical two meter probe beam OPL [5]. It is assumed that the dispersion of optical components after the co-alignment group and small deviations from the ideally aligned state cause this effect. It is also known that a loss of contrast can also cause an increase of uncertainty of the obtained phase values after I/Q demodulation [5]. Additionally, the z-axes rotations of these components lead to a greater phase error than the equivalent applied y-axis rotation, however, the differences are marginal. The overall unsymmetrical behaviour during z-axis rotation is caused by the refraction at the PBS. Due to different AOI at the PBS depending on positive or negative rotation the intersection angle between reference and probe beam varies.

In regards to rotational and translational vibrations, the component sensitivity analysis yields the maximum phase error gradients, depending on component and the applied vibration. In case of pure OPL alteration, e.g. the RR x-axis translation case, no measurement error is made. This coincides with the simple 1D-model for the phase of the two-color interferometer. For translation vibrations, which induce a spatial parallel offset between reference and probe beam, relative small phase errors were obtained. The phase

error of the conducted translation simulations is approximately 0.2 rad for components prior to the AOM and for components after the AOM between 1×10^{-5} rad and 8×10^{-5} rad, depending on the optical component and displacement. Translation vibrations prior to the AOM lead to a linear phase error function, while components after the AOM introduce non-linear phase errors. It was also observed that constant contrast is obtained in all these cases.

The principle of vibration robustness is, in general, still confirmed by the simulated phase signals. For most translation and rotation vibrations the phase error is vastly smaller than the individual phases. A prime example for this is the RR x-axis translation, where the individual phases cancel each other out fully. In total this shows that the inherent vibration robustness holds true for many cases as assumed. In case of more complex spatial differences between reference and probe beams due to offsets or angular deviations, relatively small errors are introduced by the components after the AOM. Vibrations of optical components prior to the AOM are shown to falsify the measurement results drastically.

For the interpretation of the results detailed above the following limitations must be considered. Translation and vibration simulations were carried out with a fixed assumed amplitude. The translation vibration simulation was carried out with an amplitude of 1.064 µm. Larger displacement amplitudes are possible in practice. To simulate greater displacement amplitudes at the same frequency, the computational cost increases. The reason for this is that the carrier frequency modulation $\tilde{\Omega}$ must be chosen as described in Ch. 3.5.3. It must also be considered that for greater translation amplitudes a greater induced parallel shift may lead to a drop-off of one of the beams at the PD due to the small PD active area. Furthermore, vibrations in the real-world are coupled and superimposed, meaning translation and rotation will occur simultaneously for multiple components. Thus coupled phase errors could introduce non-linear responses which can not be linearly superimposed. The results of this work can be interpreted as a lower limit of possible phase errors.

Furthermore, as mentioned in Ch. 3.1.1, aberrations were not taken into account for the complex ray tracing method. Astigmatism may lead to additional differences in the phase fronts of reference and probe beams. However, the analysed optical components were planar and much larger than the analysed Gaussian beams. In addition, the analysed displacement offsets and angles where sufficiently small to assume quasi-linear behaviour.

6 Conclusion and Outlook

The main goal of this work was to implement a digital model of a two-color interferometer and simulate the heterodyne optical time-domain signal at a PD using the complex ray tracing method. This was done to allow the investigation of interference patterns which can not be analysed in the laboratory due to the modulation frequencies involved. In the following section, the content of this work will be summarized. Based on the findings specific improvements to the optical setup, as well as the simulation method, will be suggested for future work.

The time-domain simulation mentioned above has been successfully demonstrated. Optical components, such as the HBS, PBS and AOM were modelled to represent the interferometer digitally within the context of the SCDI framework. To model the diffraction inside of the AOM, a vector formalism from literature was employed and verified. The position and orientation of each optical component of the digital twin was chosen to recreate the laboratory setup of the interferometer. The complex ray tracing method was applied to simulate the propagation paths of the laser beams throughout the optical setup. Spatial interference effects between reference and probe beams, such as angular deviations, parallel shifts or OPL differences were simulated using this technique.

Furthermore, a heterodyne simulation method was utilized to resolve the time-dependent interference at the PD. The obtained power signal was I/Q demodulated in a post-processing step to extract the phase of each emitted wavelength. This closely represents the real-world signal acquisition chain.

Translation and rotation vibration simulations of individual components were conducted to create a component sensitivity overview of the interferometer. It was observed that for cases where only the OPL is altered, e.g. the x-axis translation of the RR, the phase measurement is not affected and the statement of vibration robustness holds true. In cases where parallel offsets or angular differences between the reference and probe beams are introduced, the phase fronts overlap non-trivially and mechanical phase effects can no longer be assumed to be linear in nature. The resulting phase measurement will lead to erroneous pressure change readings. The phase error magnitude and gradient is especially critical for the beam co-alignment optics before the AOM and can reach up to several hundreds of Pa in equivalent pressure change, making the sensor readings unusable.

Based on these findings it is highly recommended to replace the co-alignment optical group before the AOM with a refractive realignment solution. This is true for all reflective optics, since they will double any vibrational dealignment in general, but most critical for the mentioned optical elements. Errors accrued at this point of the optical system will scale with the overall OPL. It was also calculated that, even with good alignment, the vibration resistance of the system only holds under certain circumstances. Therefore, any reduction of the vibration amplitudes affecting the system are beneficial. In order to verify the validity of the simulated results, experiments should be conducted that assess the component sensitivity and compare them to the results obtained in this work.

Regarding the simulation itself, the complex ray tracing method allows the fast computation of the Gaussian beam propagation path. The influence of dispersive elements was considered in the simulation by the wavelength-dependent refraction at optical components. However, aberrations such as astigmatism or spherical aberrations are not included by default. Thus, the implementation of the general astigmatic Gaussian beam [36] and field

decomposition [18] is of interest for future simulations which might include curved optical surfaces. This would allow to simulate a telescope in the returning probe beam path and the investigation of phase front matching on the overall component sensitivity. The impacts of this optimization on the measurement results is of interest for future simulations.

In addition, an auto-align utility to automate the adjustment of components would be helpful. The AOM model used for complex ray tracing is primitive compared to the extensive analytical description of diffraction. However, the provided model is sufficient to calculate the direction of diffracted beams. A possible extension of the AOM model is the consideration of diffraction efficiency, where the intensity distribution of an outgoing beam depends on input parameters such as the AOI and the diffraction order.

References

[1] Philip E. Ciddor. Refractive index of air: new equations for the visible and near infrared. *Appl. Opt.*, 35(9):1566–1573, Mar 1996. 1, 3

[2] J. Irby, R. Murray, P. Acedo, and H. Lamela. A two-color interferometer using a frequency doubled diode pumped laser for electron density measurements. *Review of Scientific Instruments*, 70(1):699–702, 01 1999. 1

[3] V. P. Drachev, Yu. I. Krasnikov, and P. A. Bagryansky. Dispersion interferometer for controlled fusion devices. *Review of Scientific Instruments*, 64(4):1010–1013, 04 1993. 3, 4

[4] Dong-Geun Lee, K. C. Lee, J.-W. Juhn, Jae-seok Lee, and Y.-c. Ghim. The new single crystal dispersion interferometer installed on kstar and its first measurement. *Review of Scientific Instruments*, 92(3):033536, 03 2021. 1

[5] Hugo Uittenbosch, Oliver Kliebisch, Raoul-Amadeus Lorbeer, and Peter Mahnke. Synthetic dispersion interferometry for relative atmospheric pressure sensing. *Opt. Express*, 31(4):6356–6369, Feb 2023. 1, 4, 5, 7, 8, 14, 25, 57

[6] Hugo Uittenbosch, Raoul-Amadeus Lorbeer, Oliver Kliebisch, Peter Mahnke, and Thomas Dekorsy. Stability and vibration robustness of a real-time synthetic dispersion interferometer. Optica Sensing Congress, 2023. 3, 4

[7] A. Korpel. Acousto-optics—a review of fundamentals. *Proceedings of the IEEE*, 69(1):48–53, 1981. 9

[8] A. KORPEL. Acousto-optics. volume 3 of *Applied Solid State Science*, pages 71–180. Elsevier, 1972. 9

[9] Thorlabs Inc. UV Fused Silica Broadband Plate Beamsplitters (Coating: 250 - 450 nm). https://www.thorlabs.com/newgrouppage9.cfm?objectgroup_id=4806. Accessed: 2024-09-23. 9

[10] Thorlabs Inc. Broadband Polarizing Beamsplitter Cubes. https://www.thorlabs.com/newgrouppage9.cfm?objectgroup_id=739. Accessed: 2024-09-23. 9

[11] R. Loudon. *The Quantum Theory of Light*. OUP Oxford, 2000. 9, 10

[12] B.E.A. Saleh, M.C. Teich, and M. Bar-Eli. *Optik und Photonik*. Wiley, 2020. 10, 11, 12

[13] Jacques Arnaud. Representation of gaussian beams by complex rays. *Appl. Opt.*, 24(4):538–543, Feb 1985. 12

[14] Donald DeJager and Mark Noethen. Gaussian beam parameters that use coddington-based y–nu paraprincipal ray tracing. *Appl. Opt.*, 31(13):2199–2205, May 1992. 12

[15] J. A. Arnaud and H. Kogelnik. Gaussian light beams with general astigmatism. *Appl. Opt.*, 8(8):1687–1693, Aug 1969. 12

[16] Evgenia Kochkina. *Stigmatic and astigmatic Gaussian beams in fundamental mode: impact of beam model choice on interferometric pathlength signal estimates*. PhD thesis, Gottfried Wilhelm Leibniz Universität Hannover, 2013. Available at https://doi.org/10.15488/8105. 12

[17] Jeff Bezanson, Alan Edelman, Stefan Karpinski, and Viral B Shah. Julia: A fresh approach to numerical computing. *SIAM review*, 59(1):65–98, 2017. 13

[18] N. Worku and H. Gross. Vectorial field propagation through high NA objectives using polarized Gaussian beam decomposition. In Kishan Dholakia and Gabriel C. Spalding, editors, *Optical Trapping and Optical Micromanipulation XIV*, volume 10347, page 103470W. International Society for Optics and Photonics, SPIE, 2017. 15, 60

[19] Thorlabs Inc. Harmonic Beamsplitters for ND:YAG Wavelengths. https://www.thorlabs.com/newgrouppage9.cfm?objectgroup_id=7035. Accessed: 2024-10-21. 16, 18

[20] Mikhail N. Polyanskiy. Refractiveindex.info database of optical constants. *Scientific Data*, 11(1):94, Jan 2024. 18, 24

[21] Thorlabs Inc. Nd:YAG Laser Line Mirrors. https://www.thorlabs.com/newgrouppage9.cfm?objectgroup_id=3793. Accessed: 2024-10-29. 19, 20, 21

[22] Isomet Corporation. Acousto-Optics. https://isomet.com/acousto_optics.html. Accessed: 2024-11-06. 22, 23

[23] Class Instrumentation Ltd. Sound Velocity Table. https://www.classltd.com/sound-velocity-table/. Accessed: 2024-11-06. 24

[24] Isomet Corporation. Acousto-Optic Modulation. https://isomet.com/App-Manual_pdf/AOModulation.pdf. Accessed: 2024-11-06. 24

[25] Technology Design. Material Sound Velocities. https://technologydesign.com/wp-content/uploads/2023/01/Material_Sound_Velocities-1.docx. Accessed: 2024-11-06. 24

[26] Thorlabs Inc. Mounted Hollow Retroreflector Mirrors. https://www.thorlabs.com/newgrouppage9.cfm?objectgroup_id=12625. Accessed: 2024-10-30. 26

[27] Thorlabs Inc. BSW26 - Ø1" 50:50 UVFS Plate Beamsplitter, Coating: 350 - 1100 nm. https://www.thorlabs.com/thorproduct.cfm?partnumber=BSW26. Accessed: 2024-11-07. 27

[28] Thorlabs Inc. PDA10A - Si Fixed Gain Detector. https://www.thorlabs.com/thorProduct.cfm?partNumber=PDA10A. Accessed: 2024-11-07. 28, 29

[29] Thorlabs Inc. Beam Displacement Optics. https://www.thorlabs.com/newgrouppage9.cfm?objectgroup_id=5952. Accessed: 2024-11-18. 31

[30] Tobias Janke. Design and testing of an optical sensor for relative pressure measurement in aviation. Bachelor's thesis, University of Stuttgart, May 2024. 32

[31] Thorlabs Inc. Smooth Bore Kinematic Mirror Mounts with Two Adjusters. https://www.thorlabs.com/newgrouppage9.cfm?objectgroup_id=1492. Accessed: 2024-11-22. 32

[32] Thorlabs Inc. Clear-Edge Kinematic Mirror Mounts. https://www.thorlabs.com/newgrouppage9.cfm?objectgroup_id=8670. Accessed: 2024-11-22. 32

[33] K. Magnus, K. Popp, and W. Sextro. *Schwingungen: Physikalische Grundlagen und mathematische Behandlung von Schwingungen*. SpringerLink: Bücher. Springer Fachmedien Wiesbaden, 2013. 35

[34] United States Department of Defense. MIL-STD-810H. https://quicksearch.dla.mil/qsDocDetails.aspx?ident_number=35978. Accessed: 2024-12-04. 37, 38

[35] Julia DSP. Digital Signal Processing Routines in Julia. https://docs.juliadsp.org/stable/contents/. Accessed: 2024-12-05. 45

[36] Alan W. Greynolds. Propagation Of Generally Astigmatic Gaussian Beams Along Skew Ray Paths. In Dale M. Byrne and James E. Harvey, editors, *Diffraction Phenomena in Optical Engineering Applications*, volume 0560, pages 33 – 51. International Society for Optics and Photonics, SPIE, 1986. 59

7 Appendix

A. Data sheet acoustic-optic modulator

CAOM-080-030-CQC-532&1064-AF-A03

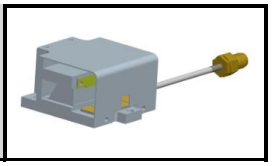

Acousto-optic modulators (AOM) allow the intensity of light to be controlled and modulated at rates that far exceed mechanical shutters.

声光调制器（AOM）允许以远超过机械快门的速率来控制和调制光强。

Getting more information
进一步获得信息

1. Specifications（规格）

Interaction material（介质材料）	Crystal quartz (石英)
Wavelength（光波长）	532&1064 nm
AR coating（AR膜反）	< 0.5% per surface
Transmission（透过率）	> 99%
RF frequency（射频频率）	80 MHz
Active aperture（有效孔径）	3.0 mm
Acoustic mode（声波模式）	Longitudinal（纵波）
Polarization（光偏振）	Linear, vertical to base（线偏振，垂直基座）
Diffraction efficiency （衍射效率）	＞85%
Separation angle（分离角）	7.41mrad @532nm; 14.83mrad @1064 nm
RF power（射频功率）	20W (Max)
Input impedance（输入阻抗）	50 Ohms
VSWR（驻波比）	< 1.2:1
RF line length（射频线长度）	100 mm
RF line orientation（射频线方向）	Left, face up to the marking surface of S/N （左侧，面向S/N打标面）
RF connector（射频接头）	SMA-F
Cooling（散热方式）	Conduction-cooled（传导散热）
Shell material（外壳材料）	Aluminum alloy 6063（铝6063）
Storage temperature（存储温度）	-20~70 ℃

2. Ordering Codes（编码规则）

CAOM	—080	—030	—CQ	C	—532&1064	—AF	—A03
	RF frequency	Aperture	Material	Acoustic mode	Wavelength	RF connector	Housing
	射频频率	有效孔径	介质材料	声波模式	光波长	射频接头	封装
	80MHz	3.0mm	Crystal quartz (石英)	Longitudinal (纵波)	532&1064nm	SMA-F	A03

3. Dimensions（外形尺寸-mm）

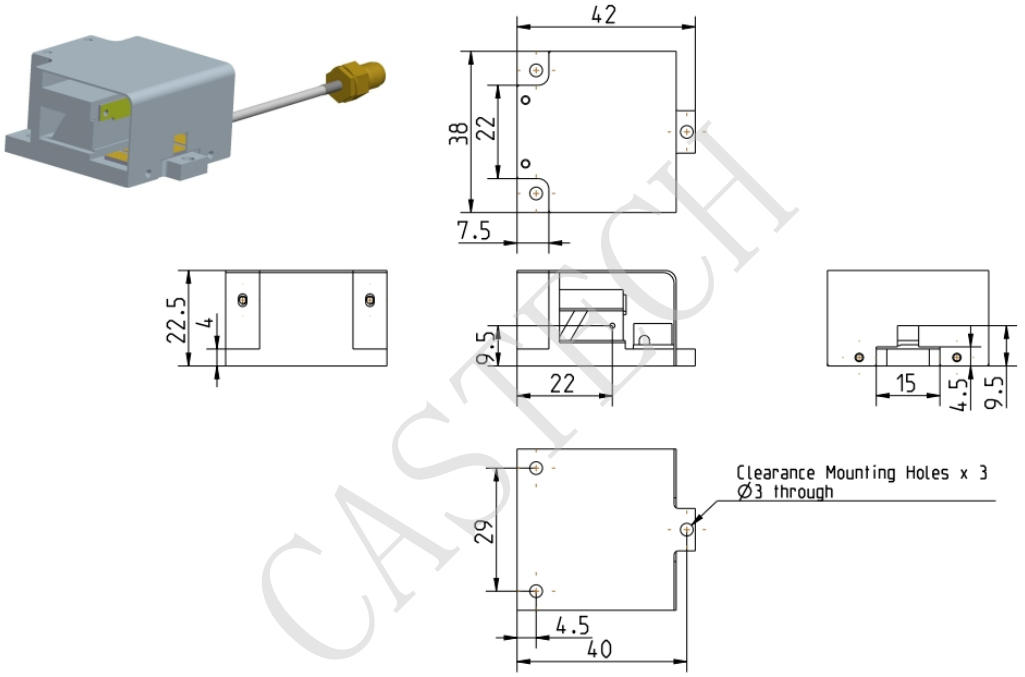

4. Version Informations（版本信息）

Number（编号）	Revision date（修订日期）	Revisions content（修订内容）
1.0	2023.08.18	/

CASTECH reserves the right to make changes to the products or information herein without notice.
（本公司保留更改本产品或资料之权利，恕不另行通知。）